Advanced Control of Active Filters in a Battery Charger Application

Martin Bojrup

Lund 1999

Cover picture
Measurement on the dynamic response of the MRI harmonic filter controller: load current (top), resulting line current (middle), and injected active filter current (bottom), see further page 101.

Department of Industrial Electrical Engineering and Automation (IEA)
Lund Institute of Technology (LTH)
P.O. Box 118
S–221 00 LUND
SWEDEN

ISBN 91-88934-13-6
CODEN:LUTEDX/(TEIE-1021)/1-124/(1999)

Printed in Sweden by Universitetstryckeriet, Lund University
Lund 1999

Abstract

In this thesis, a high performance battery charger for electric vehicles (EVs) is investigated. By including active power line conditioning capabilities in the battery charger, a viable concept for a fast charging infrastructure is obtained, beneficial both to the EV users and the power distributors.

The thesis contains discussions on modelling aspects and design considerations for the proposed battery charger, based on a carrier wave modulated self commutated 2-level voltage source converter topology. Furthermore, model based controller synthesis is employed, and thorough analysis of the controller characteristics is given.

Emphasis is put on the active filtering performance of the battery charger. The weaknesses of the model based control system in active filter applications are revealed, where especially the inherent phase deviation of the control system and the sensitivity to system parameters deteriorates the performance of the active filter.

In order to overcome the deteriorating properties of the model based controller, a controller structure for active filters based on several integrators in multiple reference frames is proposed. It is shown, both theoretically and experimentally, that the proposed controller exhibits low sensitivity to system parameters and provides for complete compensation of the inherent phase deviation. The result is excellent conditioning performance of the proposed active filter controller in steady state.

Acknowledgements

First of all, I would like to express my sincere gratitude to Per Karlsson for invaluable discussions during this project and a lot of laughs. He has proven to be the perfect friend, colleague and travelling companion.

I would also like to thank my supervisor Professor Mats Alaküla for his encouragement and support during this work. I am also grateful to Professor Lars Gertmar for initiating the research project and for fruitful discussions and comments along the way.

The support from the external members of the reference group, Anders Lasson (Volvo Technological Development) and Ulf Thorén (Sydkraft AB), has been greatly appreciated.

I wish to thank all my colleagues and the staff at IEA for providing a creative and stimulating atmosphere, and in particular to the lunch party, to Dr. Ulf Jeppsson for maintaining the UNIX system, to Getachew Darge for maintaining the workshop and to Bengt Simonsson for his helping hands in the laboratory.

I would like to thank my immediate family for their support during this time. I am also indebted to Karin for her love and support.

This work has been financially supported by Elforsk, within the Elektra research program, which is gratefully acknowledged.

Martin Bojrup

Contents

1

Introduction

This chapter provides an introduction to the thesis and points out the main objectives with the work carried out leading to this thesis.

1.1 Background

The Electric Vehicle (EV) has lately, during the past 10 years, been focus for thorough research where the major concern is to find a replacement for the Internal Combustion Engine (ICE) driven vehicle. Environmental aspects such as the air pollution due to the emissions of the ICE are the key driving forces for the research in alternatives to the ICE. Another fact is the limited oil reservoirs, which in the future inevitable will be depleted.

The tremendous development in the area of power electronics in terms of size, rating and frequency characteristics together with adapted electrical motors make high performance EV drives possible. The performance characteristics, i.e. top speed and acceleration capabilities, of the high performance EV drives are similar or superior to the ones obtained by an ICE [16].

The major short coming of the present EV originates from the limited energy storage on-board the vehicle, which reduces the obtainable driving range compared to an ICE. High power/energy density storage of electric energy is hard to achieve and expensive. But improvement in battery technology from lead-acid to NiCd or Ni-MH has considerable increased the storage capacity. The driving range of present EVs is approximately 70–100 km per one full charge, though dependent on the driver.

In order to increase the driving range of the EV, on-board charging systems such as ICE driven generators or fuel cells can be included. This gives higher freedom in the operation of the ICE. The ICE can be operated optimally with respect to emissions, efficiency or fuel consumption leading to improved overall performance [13]. Acceleration and peak power are then provided by the electrical supply. Fuel cells, on the other hand, provides electrical power through electro-chemical

reaction. Fuel cells have high power/energy density and the electro-chemical reaction is almost emission free, but they are expensive and still lot of development has to be done [28].

To further provide a wide take-up of EVs, a public charging infrastructure is needed [30]. Such a infrastructure would increase the mobility of the EV driver at least if fast charging, i.e. charging with high power, is an alternative. The driving range in between charging instants would be the same, but fast charging reduces the charging time considerably. Therefore, an EV driver may accomplish a 2-3 times longer daily driving range.

The topic for this thesis is to describe how such a fast charging station could be implemented in order to obtain the best use of the investment.

1.2 Charging – Fast charging

Charging of a battery is accomplished by the supply of a DC current to the battery. The DC current provides electrical charges that are stored in the battery through an electro-chemical process. Since current is defined as the transport of electrical charges per time, the energy delivered during the charging process is determined by the amount of DC current supplied and the elapsed time. Electrical energy is transferred from generator to consumer in AC quantities. These AC quantities have to be converted into DC quantities in a controllable manner suited to the voltage/current levels of the battery. This is the task for the battery charger.

Battery chargers are grouped in on-board and off-board chargers. An on-board charger is individual to the EV and located internally in the vehicle, while the off-board charger is of external and stand alone type. Off-board chargers are typically located at a charging station or at parking areas. The principle of operation is the same but the on-board charger performs the AC to DC conversion inside the vehicle, thus the vehicle is charged from an AC supply. The off-board charger, on the contrary, acts as a DC supply where the AC to DC conversion is made elsewhere from the vehicle point of view.

Both on-board and off-board chargers can operate from single or three phase AC supplies. On-board chargers are mainly of single phase type, since weight and size are crucial in vehicle applications. However, a three-phase charger can provide three times the charging power of a single phase charger, since all three phases can be loaded as much as the single phase charger loads one phase. Therefore, the charging time is reduced by

a third. Table 1.1 lists performance characteristics of different types of chargers, when charging an EV corresponding to a driving distance of 100 km. The energy consumption of the EV has been estimated to 20 kWh per 100 km in the comparison. The corresponding refuelling time for ICE vehicle is also given in Table 1.1.

Table 1.1 Charging power and time corresponding to a driving distance of 100 km.

Fuse / Phases	Power	Time	Type
16 A × 1	3 kW	7 h	On-board
16 A × 3	10 kW	2 h	Off-board
120 A × 3	75 kW	15 min	Fast charging station
		1/2 min	Gas station

Off-board chargers operate either in a conductive or inductive manner. Conductive chargers supply the electrical energy through conductors all the way from the DC output of the charger to the terminals of the battery. Inductive chargers, on the other hand, have a galvanic isolated intermediate stage, i.e. a high frequency transformer, between the charger DC output and the battery. The primary winding of the high frequency transformer is preferably located in the connector handle whereas the secondary winding is located inside the EV [19][29], thus providing galvanic isolation throughout the charging process. However, the losses in the high frequency transformer can reduce the energy efficiency of the charging process.

A major problem associated with charging of EV batteries is the lack of standardisation, since almost every car manufacturer has their own idea of how it should be done. Due to this, both types of chargers are focus for development and research [5][21].

Hereafter, only three phase conductive chargers are investigated.

1.3 Influence on the power grid

An introduction of EVs will have an impact on the power grid and its operation. Typically, on-board chargers will be used during night time when the car is parked at a residence. Usually, at night time the load on the power grid is low resulting in high voltage, which causes the power grid operators to disconnect capacitor banks and even insert reactors in order to maintain the voltage magnitude. In this sense, EV charging at night can even improve operation of the power grid, since the load is smoothened out over the day. Fast charging and maintenance charging at car parks, on the contrary, are used mainly during day time in order to

increase the operating range of the vehicle. At day time the load on the power grid is high and an increase due to fast charging can cause overload situations [12][31].

EV chargers will contribute to the increase of power electronic loads on the power grid, since power electronics is necessary in the AC to DC conversion of electrical energy. Power electronic loads cause, due to their non-linear characteristics, distorted or non-sinusoidal currents on the power grid. The distorted currents cause voltage distorsion due to self impedance in cables and transformers. Voltage distorsion leads to ageing and even to damage and malfunction of sensitive electrical equipment, i.e. computers. Other harmonic current generating electrical equipment are switched mode power supplies (SMPS) in computers and television sets, adjustable speed drives (ASD) and fluorescent lights.

Current and voltage distortion are considered as a problem in the operation of the power grid, despite difficulties in determining the real consequences of their presence. Anyway, the problem with harmonics have been recognised and standards for electrical equipment, in terms of harmonic emission and immunity, are being established. As a consequence hereby, fast chargers based on line commutated converters, i.e. diode or thyristor bridge rectifiers, though cheap and relatively simple should not be used, since they do not fulfil these standards on harmonic emission into the power grid. This is concluded from Figure 1.1, where a typical non-sinusoidal line current from a line commutated charger together with its harmonic content are given.

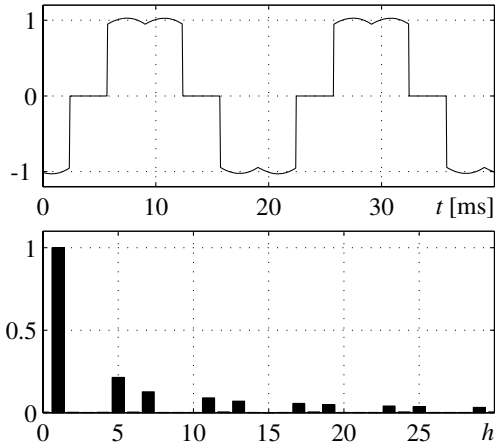

h	I_h/I_1 [%]	IEC 1000-3-4 I_h/I_1 [%]
5	21.4	9.5
7	12.7	6.5
11	9.0	3.1
13	7.1	2.0
17	5.7	1.2
19	4.9	1.1
23	4.1	0.9
25	3.8	0.8
29	3.3	0.7
31	3.1	0.7
≥35	…	≤0.6

Figure 1.1 Left) Line current from a thyristor based charger and its harmonic content. Right) Comparison of the current harmonics against the IEC 1000-3-4 regulation on current harmonic emissions.

1.4 Desired capabilities of the charger infrastructure

A fast charger should be capable of charging EVs with a grid-friendly current, i.e. sinusoidal line current with unity power factor. It should also be flexible enough to handle various battery types and sizes, with their individual voltage levels and current rating.

In order to increase the usage of a fast charger infrastructure, additional capabilities in terms of power grid conditioning can be included. This means that instead of having a negative impact on the power grid, a charger infrastructure may provide a tool for power grid operators to maintain, at least locally, a high power quality. The non-ideal, i.e. reactive, harmonic and asymmetric parts of the load current should be generated locally by the grid conditioning charger. The power grid supply would then only have to provide the active power of the load current. Figure 1.2 describes schematically the operation principle of such a grid conditioning charger. In this way, the load on distribution lines and transformers will be lowered and a more efficient supply of electrical energy obtained.

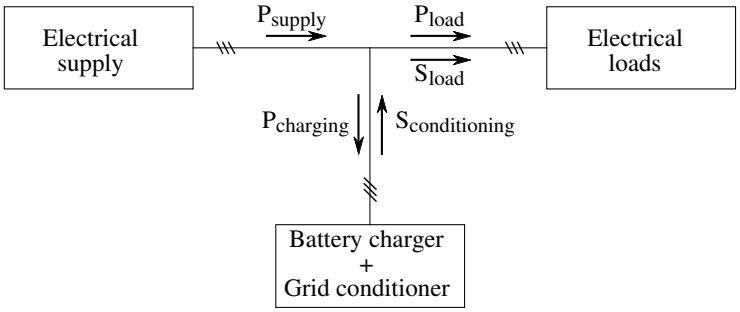

Figure 1.2 Schematic diagram of charger with grid conditioning capabilities.

Another, more controversial capability that can be included in a fast charger infrastructure deals with peak power generation, i.e. active power support at high load. EV batteries attached to fast chargers may be considered as a potential energy reserve. During short periods of time, energy could be borrowed from the batteries and supplied to the power grid. This means that the fast charger operates as an electronic gas turbine. This last capability has to be applied with great care, since the primary function of a fast charger has to be to charge EV batteries and not the opposite.

Summarising this discussion leads to a number of capabilities desired for a fast charger infrastructure:

- Charging of EVs with sinusoidal line current and unity power factor.
- Grid conditioning capabilities such as reactive power compensation, harmonic filtering and load balancing.
- Possibility to act as an electronic gas turbine, i.e. provide active power support during short periods of time by borrowing energy from the EV batteries.

1.5 Thesis outline

Chapter 1 provides a short introduction of the aim of the project leading to this thesis. In Chapter 2, basic grid conditioning concepts are investigated and tools to accomplish grid conditioning are presented. Chapter 3 describes implementation, design and modelling considerations for the proposed fast charger. In Chapter 4, the basic control structures and model based controllers for a fast charger are given. In Chapter 5 specific active filter control structures are thoroughly investigated. In Chapter 6 experimental results of a charger prototype are presented, verifying the proposed concept for fast chargers. Finally in Chapter 7 conclusion remarks are given.

Note that this thesis is one of two, evolved from the battery charger project. The accompanying thesis [18], treats hardware related aspects of the battery charger, while this thesis focuses on control and functional aspects.

2

Grid conditioning

This chapter describes the intention of power grid conditioning, its origin and how it may be done. The power grid connects the producers of electrical energy with the consumers, making it possible to transfer power from the centralised generators to the distributed consumers. Therefore, it is desired that the voltage magnitude and frequency at the consumer end are close to their nominal values and that the amount of voltage distortion is low.

The power grid consists of two parts, the transmission network and the distribution network. The transmission network consists of a meshed grid connecting different regions, it has high voltage and is therefore capable of high power transfer with low losses. The distribution network, on the contrary, consists of radial feeders inside a region where the power flows downstream from substations to consumers. The radial configuration in combination with the self impedance of the conductors causes load current dependent voltage drops and at the end of a feeder all upstream load contributions to the voltage distorsion is seen. Another problem is that resonance between conductors and capacitor banks or loads can be energised by distorted currents which also causes voltage distortion.

Electric energy transfer through the power grid is instantaneous, i.e. there is no storage of electrical energy. Therefore, frequency control is obtained by matching the active power production in the generators with the power used at the consumer end, including the losses in the distribution and transmission networks. If this is not achieved, the excess or the deficit of electrical power produced will accelerate or decelerate the generators resulting in a frequency variation.

2.1 Reactive power compensation – Voltage control

Reactive power compensation is equivalent to voltage control, that is by controlling the reactive power flow in a network substantial control of the voltage magnitude is achieved.

Reactive power Q in contrast to the active power P can not be converted into mechanical work, i.e. kinetic energy or heat etc. Instead, the reactive power represents an energy oscillation between load and generator. Still reactive power is a necessary quantity in electrical engineering, since it is used in electrical motors to build up the magnetic flux used to convert electrical energy into mechanical work. Reactive power is a steady-state property and defined as the imaginary part of the complex valued apparent power S

$$\bar{S} = \bar{U} \cdot \bar{I}^{*} = P + jQ \tag{2.1}$$

Problem – Losses and large distance transfer

Consider a loss less single distribution line with reactance X_l connecting a stiff (reference) bus to a load bus as in Figure 2.1.

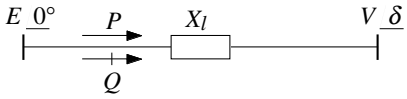

Figure 2.1 Power flow in a single line with reactance X_l.

The transfer of active and reactive power, from the stiff bus, over the line are strongly coupled and given by

$$\begin{aligned} P &= \frac{E \cdot V}{X_l} \cdot \sin\delta \\ Q &= \frac{E}{X_l}\left(E - V \cdot \cos\delta\right) \end{aligned} \tag{2.2}$$

where E is the voltage at the stiff bus, V is the voltage at the load bus and δ is the load angle, i.e. the angle difference between the voltages at the stiff and load bus [10].

From (2.2) it is found that large amount of reactive power transfer results in a significant voltage drop over the line. This is due to the dependency between the load angle δ and the active power transfer. It is also seen that a weak line, i.e. large X_l, reduces the power transfer capability.

The reactive current contributes to the rms-value of the supply current, thus resulting in a higher supply current than needed in order to deliver the active power to the load. This affects the efficiency of the power grid since in reality lines are not loss less, there exist a small resistance in addition to the reactance for every conductor. The losses in the conductors are proportional to the square of the current, therefore it is

obvious that also active as well as reactive losses increase with a large amount of reactive power transfer.

Solution – Local production

Local production of reactive power at a load bus decreases the amount of reactive power transfer over the line. Reducing the rms-value of the supply current to only correspond to the active power demand at the load bus. Therefore, the losses and the voltage drop across the line are decreased and a more efficient power grid is obtained. As a consequence, the voltage at the load bus may be controlled close to the nominal value by control of the reactive power input.

Shunt capacitor banks provide a simple way of reactive power compensation, see Figure 2.2. In a capacitor excited by a AC voltage the current leads the voltage by 90° in phasor notation, this phase lead corresponds to a injection of reactive current and thus production of reactive power. Shunt capacitor banks are common in distribution networks, where they are connected and disconnected according to the load fluctuation over the day in order to maintain a voltage magnitude close to the nominal.

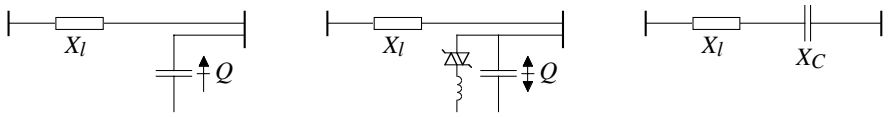

Figure 2.2 Reactive power compensation; shunt (left), TCR (middle) and series (right).

A more sophisticated solution includes a thyristor-controlled reactor (TCR) in parallel with the shunt capacitors. Such a device may even absorb reactive power during light load condition in addition to the production of reactive power. This combination can be treated as a capacitor bank with variable and even negative capacitance. Synchronous condensers, i.e. synchronous motors with no mechanical load, can also control their reactive power output to provide reactive power compensation.

Another form of reactive power compensation involves series capacitors, where capacitor banks are installed in series with the line. Their effect is to reduce the total series impedance of the line seen from the source, thereby reducing line voltage drops and increasing the line loadability.

Lately, even more advanced compensator structures, where power electronics are included, have been proposed. The unified power flow

controller (UPFC) consists of two converters connected back to back, one in series with the line and the other one in parallel [8]. The UPFC are intended for use on transmission systems and is very flexible. It can perform shunt reactive compensation as well as voltage magnitude and load angle control and line impedance compensation.

2.2 Load balancing

A balanced power grid is obtained if the three phases are equally loaded, i.e. each phase transfers one third of the total power. This gives the best utilisation of the power grid, since during balanced conditions the phases are affected in the same way. Electrical loads can be either one, two or three phase loads but since a line feeds several loads, the total load seen from the source is balanced if a large number of loads are distributed to the different phase conductors. Hence for the transmission network and the higher voltage distribution networks the balanced condition holds true. But close to the consumers, the load may be imbalanced due to the low number of loads to be distributed.

Imbalanced loads or systems may be analysed in steady state by the use of symmetrical components [10]. In accordance with symmetrical components, any balanced or imbalanced three phase quantity are resolved into three sequence components, that is positive-, negative- and zero-sequence components. The positive-sequence component consists of three phasors with equal magnitude and 120° phase displacement in positive sequence, i.e. in *abc* sequence, refer to Equation (A.5). The negative-sequence component also consists of three phasors with equal magnitude and 120° phase displacement however in negative sequence, i.e. in *acb* sequence, while the zero-sequence component have zero phase displacement. Figure 2.3 shows an example of an arbitrary unsymmetrical current separated into sequence components.

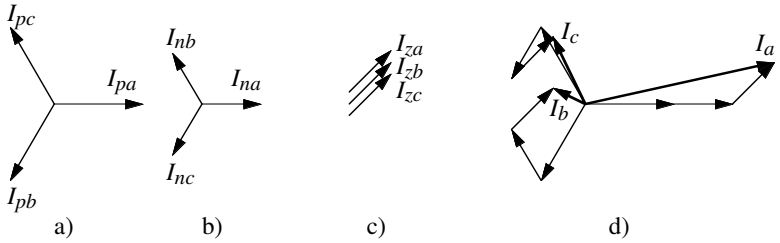

Figure 2.3 Sequences of an arbitrarily unsymmetrical current, a) positive-sequence, b) negative-sequence, c) zero-sequence and d) total current.

In Appendix A.1, the definition of the three phase to two phase vector transformation (*abc*→$\alpha\beta$) is given. A balanced system with positive-sequence, *abc* sequence, and rms-value *I* can be represented as a vector in the stationary reference $\alpha\beta$-frame as

$$\vec{i}_p^{\,\alpha\beta} = \sqrt{3} I e^{j\omega_1 t} \tag{2.3}$$

while for a balanced system with negative-sequence, *acb* sequence, the vector is according to

$$\vec{i}_n^{\,\alpha\beta} = \sqrt{3} I e^{-j\omega_1 t} \tag{2.4}$$

Positive- and negative-sequence components can thus be separated by the rotation direction of the vector in the stationary reference $\alpha\beta$-frame, see Figure 2.4. Applying the same transformation on a balanced system with zero-sequence gives

$$\vec{i}_z^{\,\alpha\beta} = 0 \tag{2.5}$$

This means that zero-sequence components are not represented in the stationary reference $\alpha\beta$-frame.

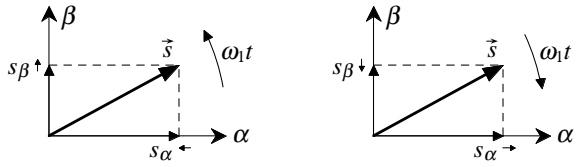

Figure 2.4 Rotation direction of vectors in the stationary $\alpha\beta$-frame, positive-sequence (left) and negative-sequence(right).

In order to obtain a vector transformation that is valid also for zero-sequence components, the given transformation in Appendix A.1 can be modified according to [25] where an *abc*→$\alpha\beta 0$ vector transformation is used.

Problem – Neutral currents and voltage distorsion

Imbalanced loads cause a distorted current distribution among the phase conductors as well as current in the neutral conductor. This leads to higher losses in the phase conductors than for a balanced load and may cause overload of a phase conductor. Neutral currents can result in circulating currents in transformers and additional losses in the windings and in the neutral conductor.

Another aspect of imbalance currents and especially neutral currents is the effect on the voltages at the load due to the self impedance in the conductors. The voltage drop in the neutral conductor affects the virtual zero potential at the load, resulting in an imbalance of the three phase voltages in terms of magnitude and phase displacement. This may cause over- and/or undervoltage in some of the phases, which in turn may cause malfunction or destruction of the electrical equipment connected to these phases.

Solution – Redirection of load currents

The most obvious solution to load imbalances is to physically connect similar loads to different phase conductors. Load balancing may also be obtained by redirection of load currents by a symmetrisation unit, see Figure 2.5. The average power used in the load mainly corresponds to the positive-sequence of the load current due to the balanced supply voltage of positive-sequence. Therefore, the negative- and/or zero-sequence components of the load current may be generated locally and thus eliminating those components from the supply current. The resulting supply current would only contain the positive-sequence component of the load current and the unsymmetrical load is seen as an equivalent symmetrical load from the supply point of view.

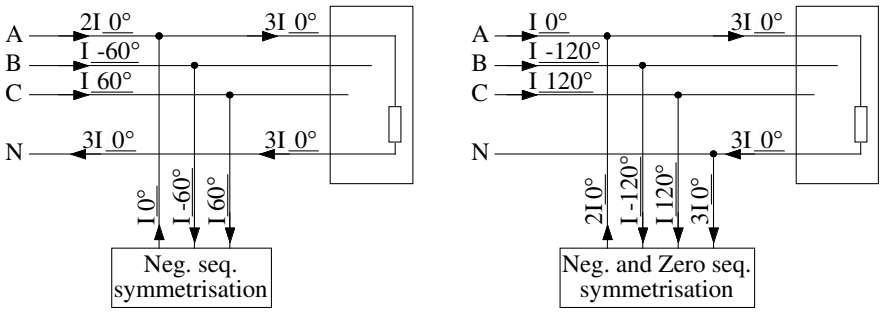

Figure 2.5 Load balancing principle, negative-sequence compensation (left), and negative- and zero-sequence compensation (right).

In Figure 2.5, the basic operation principles of such symmetrisation units are shown. In the left figure, the negative-sequence current of the load is provided by the compensator, thus resulting in only zero- and positive-sequence supply currents. Total symmetrisation is obtained in the right figure by injection of the negative- and zero-sequence currents, resulting in a balanced supply current of positive-sequence and no neutral current.

2.3 Harmonic reduction in distribution networks

Electrical equipment made of power electronics connected to the grid causes, due to their non-linear characteristics, non-sinusoidal grid currents. According to the fourier analysis, every periodic waveform can be treated as the sum of one or several sinusoidal waveforms of different frequencies, i.e. the fundamental frequency and multiples of the fundamental frequency. Since the grid voltage is nearly sinusoidal, the power used by a harmonic generating load corresponds to the fundamental frequency component of the load current. The current harmonics are a non-desired by-product due to the switched operation of line commutated rectifiers, i.e. diode or thyristor controlled rectifiers.

Current harmonics are in fact a steady-state problem due to their periodic and repetitive behaviour. However, current transients originating from inrush currents at start up or at distinctive shut downs or disconnection of loads can also be treated, in accordance to the fourier analysis, as current harmonics despite their lack of periodicity. Still, transients and their corresponding current harmonics will disappear after a sufficiently long time.

A typical load current and the corresponding harmonic spectrum of a line commutated three phase rectifier can be seen in Figure 1.1. The current contains the fundamental frequency and harmonics of order $6k\pm1$ where k is any positive integer. The current harmonics can further be resolved into sequence components, i.e. positive- and negative-sequences, according to Table 2.1. The absence of zero-sequence harmonics is due to the balanced configuration of three phase line commutated rectifiers. However, single phase line commutated rectifiers have additional zero-sequence harmonics of order $6k+3$ where k = [0,1,2…].

Table 2.1 Harmonic sequences of three phase line commutated rectifiers.

Sequence	Harmonics
Positive	1, 7, 13, 19, …
Negative	5, 11, 17, 23, …

The load current of a line commutated rectifier can be represented in the stationary reference $\alpha\beta$-frame as

$$\vec{i}_{Load}^{\,\alpha\beta} = \sqrt{3}I_1 e^{j(\omega_1 t+\phi_1)} + \sum_{h=6k-1}\sqrt{3}I_h e^{-j(h\omega_1 t+\phi_h)} + \sum_{h=6k+1}\sqrt{3}I_h e^{j(h\omega_1 t+\phi_h)} \qquad (2.6)$$

where I_1 and I_h are the rms-values of the fundamental current component and the individual current harmonics, respectively. Equation (2.6) gives a true representation of the current of three phase line commutated rectifiers, whereas for single phase rectifiers the current harmonics of zero-sequence are absent. This is due to the vector transformation used, refer to (2.5).

Problem – Losses and voltage distortion

Current harmonics result in a distorted voltage, which may cause malfunction of sensitive electrical equipment, i.e. computers. The voltage distorsion is due to the voltage drop across the non-zero impedance of cables and transformers. The current harmonics can also cause severe voltage distorsion due to resonance oscillations between the self inductance in the distribution network and the shunt capacitor banks for reactive power compensation [3][14].

Current harmonics cause additional losses in the distribution network. Transformers are exposed to thermal stresses due to an increase in iron losses caused by the distorted voltages and currents. This may lead to derating as well as premature ageing of the transformers. For electrical motors, the voltage distorsion causes thermal stresses and torque ripple.

Solution – Harmonic filtering

Current harmonics are often treated as a local problem at least for one feeder in the distribution network. The impedance of the distribution network dampens the harmonic propagation [14]. Therefore, harmonic filtering should be performed nearby the source of the current harmonics for the best result. If this is done, other equipment will be unaffected by the harmonic producing load. Harmonic filtering or compensation is accomplished by the use of passive filters, shunt active filters (AF) or series active filters.

Passive filters

Passive filters for harmonic reduction provide low impedance paths for the current harmonics. The current harmonics flow into the shunt filters instead of back to the supply. A typical shunt passive filter and the resulting equivalent impedance seen from the load are shown in Figure 2.6. The passive filter consists of series LC filters tuned for specific harmonics in combination with a general high pass filter used to eliminate the rest of the higher order current harmonics.

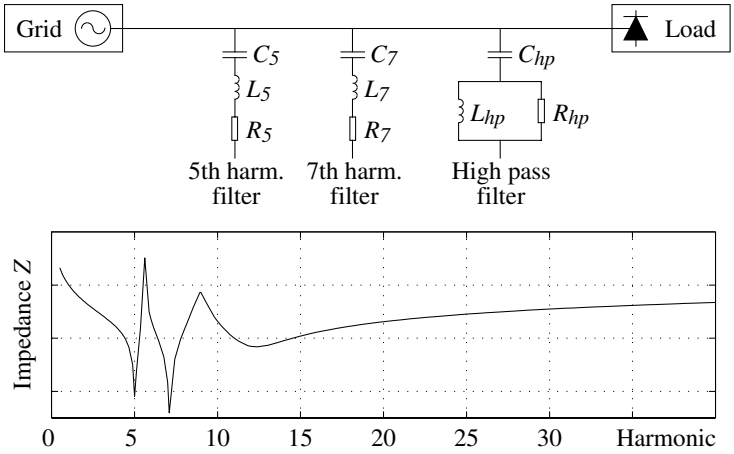

Figure 2.6 Typical passive filter for reduction of current harmonics and the equivalent impedance seen from the load.

The performance of a passive filter is strongly dependent on the system impedance at the harmonic frequencies [27]. The system impedance depends on the distribution network configuration and the loads. Therefore, design of passive filters involves thorough system analysis in order to obtain adequate filtering performance of the filter.

Shunt active filters

A shunt active filter consists of a controllable voltage or current source. The voltage source converter (VSC) based shunt AF is by far the most common type used today, due to its well known topology and straight forward installation procedure, see Figure 2.7. It consists of a DC-link capacitor C_{dc}, power electronic switches and filter inductors L_f.

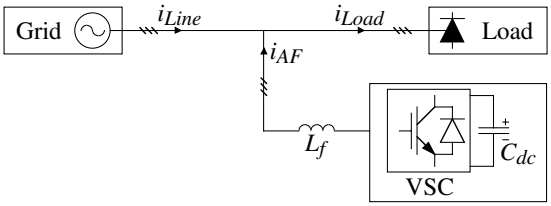

Figure 2.7 Principle configuration of a VSC based shunt active filter.

The operation of shunt AFs is based on injection of current harmonics i_{AF} in phase with the load current i_{Load} harmonics, thus eliminating the harmonic content of the line (supply) current i_{Line}. That is, suppose the load current can be written as the sum of the fundamental current component and the current harmonics according to

$$\vec{i}_{Load} = \vec{i}_{Load,fund} + \vec{i}_{Load,harmonics} \tag{2.7}$$

then the injected current by the shunt AF should be

$$\vec{i}_{AF} = \vec{i}_{Load,harmonics} \tag{2.8}$$

The resulting line current is

$$\vec{i}_{Line} = \vec{i}_{Load} - \vec{i}_{AF} = \vec{i}_{Load,fund} \tag{2.9}$$

which only contains the fundamental component of the load current and thus free from harmonics. Figure 2.8 shows the ideal phase currents when the shunt AF performs harmonic filtering of a diode rectifier. The injected shunt AF current completely cancels the current harmonics from the load, resulting in a harmonic free line current.

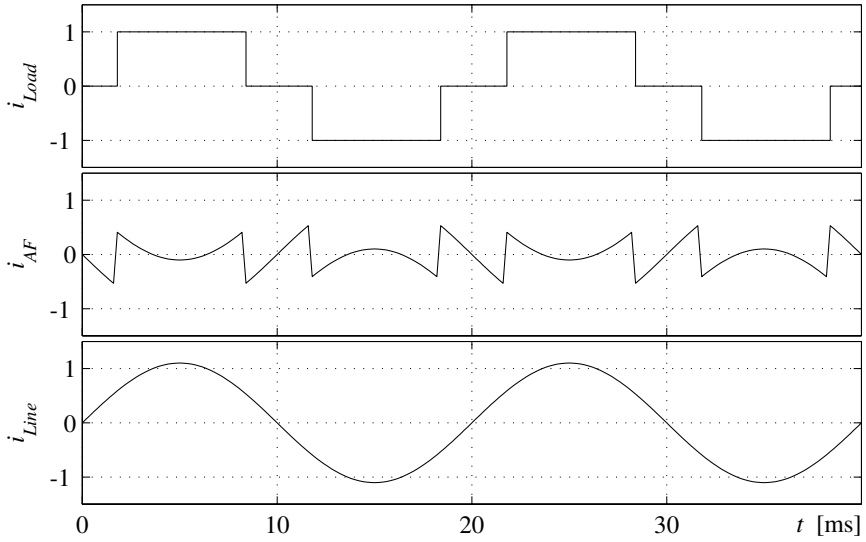

Figure 2.8 Shunt AF operation principle when performing harmonic filtering.

From the load current point of view, the shunt AF can be regarded as an varying shunt impedance. The impedance is zero, or at least small, for the harmonic frequencies and infinite in terms of the fundamental frequency.

Series active filters

Series active filters are connected in series with the line through a matching transformer. VSCs are appropriate as the controlled source even for series AFs, thus the principle configuration of series AFs are similar

to shunt AFs. The filter inductors of shunt AFs are replaced with the series transformer, see Figure 2.9.

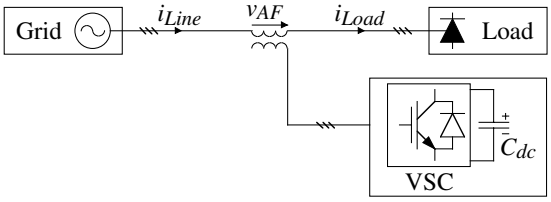

Figure 2.9 Principle configuration of a series AF system.

The operation principle of series AFs is based on isolation of the harmonics in between the load and the supply [4]. This is obtained by the injection of harmonic voltages across the transformer line side. The injected harmonic voltages affect the equivalent line impedance seen from the load. The equivalent line impedance can be regarded as infinite or large for the harmonics whereas it should ideally be zero for the fundamental frequency component. The operation principle of a series AF is illustrated in Figure 2.10.

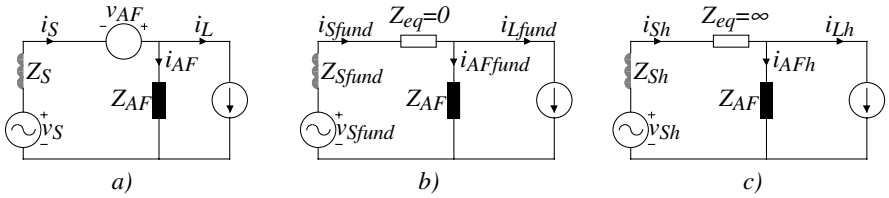

Figure 2.10 Series AF operation principle; a) single phase equivalent of series AF, b) fundamental equivalent circuit, and c) harmonic equivalent circuit.

Harmonic isolation is achieved by means of the infinite impedance for the current harmonics in series with the line. That is, no current harmonics can flow from load to source or from source to load. Current harmonics produced elsewhere on the source side of the series AF can not interfere with loads on the load side, i.e. passive filters and shunt capacitors.

Hybrid filters

Hybrid filters consists of combinations of shunt/series AFs and shunt passive filters. The main purpose of hybrid filters are to reduce the initial costs and to improve efficiency. The passive filters reduces the bulk harmonic content of the load current, whereas the active filter handles the rest of the harmonic content not filtered by the passive filters. Therefore, the rating of the active filter can be decreased compared to a stand alone active filter and thus reducing the initial cost. Figure 2.11 shows two

examples of hybrid filter configurations, additional configurations have been reported in the literature [3].

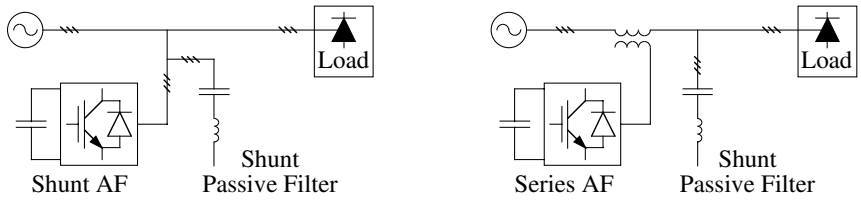

Figure 2.11 Hybrid filters; left) combination of shunt AF and shunt passive filter, and right) combination of series AF and shunt passive filter.

The optimal solution to harmonic reduction in distribution networks in terms of performance characteristics consists of the combination of a shunt and a series AF with a common DC-link, see Figure 2.12. This combination is referred to as the unified power quality conditioner (UPQC) and has the same configuration as the UPFC, refer to Section 2.1 page 10. However, the UPQC for distribution networks differ from the UPFC for transmission networks in terms of operation, purpose and control strategy [3]. The conditioning functions of the UPQC are shared by the series and shunt AFs. The series AF performs harmonic isolation between supply and load, voltage regulation and voltage flicker/imbalance compensation. The shunt AF performs harmonic current filtering and negative sequence balancing as well as regulation of the DC-link voltage shared by the AFs. The DC-link voltage regulation is obtained by balancing the active power from both the VSCs including all losses in the passive as well as the active components.

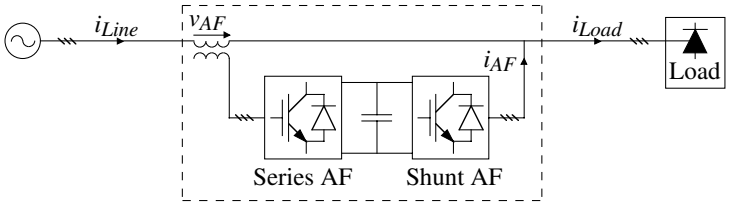

Figure 2.12 Configuration of the unified power quality conditioner (UPQC).

3

Design and modelling of the battery charger

In this chapter, the hardware topology of the investigated charger is discussed. Design considerations and modelling aspects of the charger are given. The topology selection for the battery charger is based on the desired capabilities for a fast charger infrastructure derived in Section 1.4:

- Conductive charging of EVs with sinusoidal line current.
- Grid conditioning capabilities such as:
  - Harmonic filtering
  - Load balancing
  - Reactive power compensation
- Possibility to act as an electronic gas turbine.

These requirements and restrictions indicate the type of power electronics to use. Line commutated converter topologies can not be used, due to their non-sinusoidal line current. The second point hints the usage of an active filter topology as the line side interface of the battery charger. Finally, the third capability is accomplished if the battery charger is designed for bi-directional power flow, i.e. the power can flow in either direction between the power grid and the EV batteries.

3.1 System description

The selected battery charger topology able to carry out the listed capabilities is shown in Figure 3.1, where the point of common coupling (PCC) towards the power grid and an EV battery attached to the charger are also shown. The battery charger consists of a DC-link capacitor C_{dc}, a three phase VSC connected back to back to a half bridge converter, and passive filters.

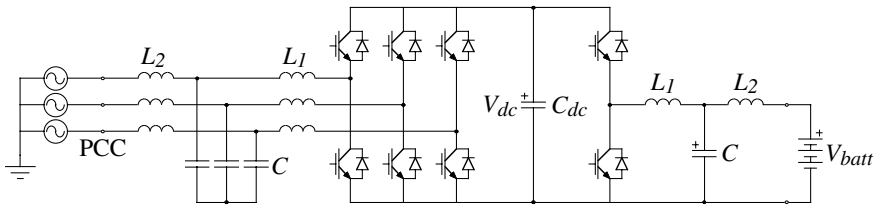

Figure 3.1 The selected battery charger topology.

The passive filters are, due to the switched operation of the VSCs, essential components of the battery charger topology. The output voltage pulses of the VSCs are filtered by the passive filters, reducing the high frequency current components. Hence, sinusoidal line currents as well as a low ripple battery current are obtained. The passive filters shown in Figure 3.1 consist of third order LCL-filters instead of ordinary first order L-filters. The reasons are discussed in Sections 3.4 and 3.5. At the moment, it is sufficient to say that the high frequency as well as the low frequency characteristics of the LCL-filter are beneficial compared to the L-filter configuration, i.e. the equivalent impedance is high for the high frequency current components and low for the active filter currents.

The line side of the battery charger topology forms an equivalent shunt AF. The decoupling of the converters provided by the DC-link capacitor ensures that the functionality of the shunt AF is separated from the battery side operation. Therefore, harmonic filtering as well as load balancing and reactive power compensation may be accomplished by the topology selected. However, the lack of a neutral conductor makes balancing of zero-sequence current components impossible. Thus, only negative-sequence current balancing is achievable according to the discussion in Section 2.2.

Finally, the half bridge DC-DC converter enables charging of EV batteries of different voltage levels. Furthermore, it allows bi-directional battery current and thus that the battery charger is able to function as an electronic gas turbine.

3.2 Converters

The VSCs of the battery charger consist of four bridge legs as shown in Figure 3.2. Three bridge legs form the line side converter while the fourth bridge leg acts as the DC-DC converter at the battery side. A bridge leg, or a half bridge converter, consists of two transistors each

connected to an anti-parallel diode. The transistors should preferably be IGBTs[1] due to their superior overall performance characteristics, i.e. forward voltage drop and switching times, in the power range considered. Soft recovery free-wheeling diodes should be used in order to get less snappy turn-off at reverse recovery of the diodes.

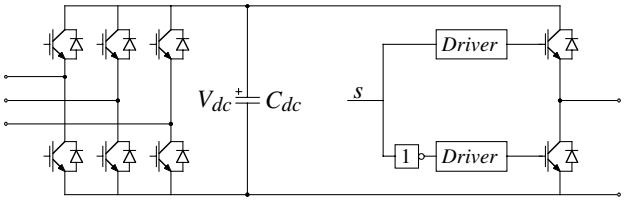

Figure 3.2 The VSCs of the battery charger including drivers for the DC/DC half bridge converter.

In Figure 3.2, additional drivers needed to convert the logic control signal *s* into gate voltages suitable to the IGBTs are also shown. The logic inverter block prior to the lower IGBT driver ensures that the IGBTs are not simultaneously conducting. Thus, short circuit of the DC-link capacitor is prevented.

Ideally, there are no losses in the VSCs and current commutation is instantaneous. However, this is not the case for practical VSCs. In practical converters the power electronic devices are not loss less and the switching times are finite. When a power electronic device is conducting current, a simultaneous voltage drop of a few volts across the device appears. The finite switching times imply that the current and the voltage are simultaneously high, leading to large instantaneous power dissipation during the switching transients. These losses, referred to as conduction losses and switching losses, are the limiting factors in the current loading capability and the switching frequency. Stray inductance further stresses the power electronic devices at the switching instants [27]. Therefore, snubbers to reduce these effects are often needed.

The finite switching times further imply that during commutation both IGBTs may conduct at the same time, since one IGBT is turning on and the other one is turning off. This implies that the DC-link capacitor is short circuited at the switching instants. This is prevented by additional control logic in the drivers. The turn on of the IGBTs are delayed in order to guarantee the completion of the turn off process of the other

---

1 Insulated Gate Bipolar Transistor

IGBT. This is referred to as the interlock or blanking time, since both IGBTs have temporarily logic low control signals.

The energy efficiency of the VSCs may be improved by the use of soft-switched topologies instead of the hard-switched shown in Figure 3.2 [17]. Extensive analysis of resonant converters are performed in the parallel thesis [18] and therefore not considered in this thesis.

Instantaneous modelling

In order to model the VSCs, the simplified equivalent circuit of Figure 3.3 is used. The equivalent circuit is derived based on the ideal properties of the VSCs. Hence, the upper valve of the half bridge is conducting when the logic control signal or the half bridge switching state s is high, whereas the lower valve conducts when s is low. High and low value of the switching state corresponds to one and zero, respectively, in the following discussion.

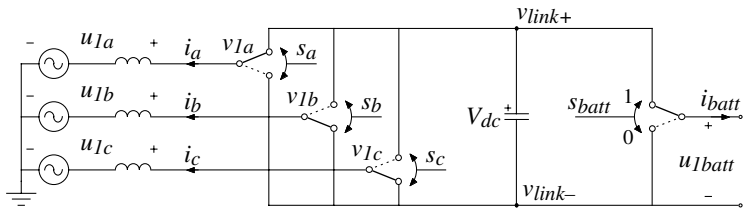

Figure 3.3 Simplified ideal model of the VSCs.

The instantaneous uni-polar output voltage u_{1batt} of the half bridge DC/DC converter is given by

$$u_{1batt} = s_{batt} V_{dc} \tag{3.1}$$

where s_{batt} corresponds to the switching state of the DC/DC converter. When s is low, the output voltage is ideally zero, since the output terminal is shorted by the lower valve to the DC-link negative supply rail. If, on the other hand, the switching state s is high then the upper valve is active. Hence, the output terminal is connected to the positive supply rail of the DC-link and the output voltage ideally equals the value of the DC-link voltage, i.e. V_{dc}.

A similar approach for the three phase VSC gives the following expressions for the output phase voltage potentials with respect to the DC-link negative supply rail

$$\begin{cases} v_{1a} = s_a V_{dc} \\ v_{1b} = s_b V_{dc} \\ v_{1c} = s_c V_{dc} \end{cases} \tag{3.2}$$

where s_a, s_b and s_c are the switching states of the bridge legs for phases a, b and c, respectively. From (3.2) the output phase voltages seen from the neutral point of the power grid are given by

$$\begin{cases} u_{1a} = v_{1a} + v_{link-} = s_a V_{dc} + v_{link-} \\ u_{1b} = v_{1b} + v_{link-} = s_b V_{dc} + v_{link-} \\ u_{1c} = v_{1c} + v_{link-} = s_c V_{dc} + v_{link-} \end{cases} \tag{3.3}$$

where v_{link-} is the voltage potential of the DC-link negative supply rail with respect to the power grid neutral. The voltage potential of the DC-link negative supply rail can be determined from the balanced condition of a three phase system, which states that the phase quantities should sum up to zero according to Equation (A.3). That is, since

$$u_{1a} + u_{1b} + u_{1c} = 0 \tag{3.4}$$

then v_{link-} is given by

$$v_{link-} = -\frac{s_a + s_b + s_c}{3} V_{dc} \tag{3.5}$$

which indicates that the DC-link supply rails of the VSCs are floating with respect to power grid neutral.

The corresponding voltage vector of the three phase VSC in the stationary reference $\alpha\beta$-frame, obtained by the space vector transformation given in Appendix A.1, is defined as

$$\vec{u}_1^{\alpha\beta} = \sqrt{\frac{2}{3}}\left(u_{1a} e^{j0} + u_{1b} e^{j\frac{2\pi}{3}} + u_{1c} e^{j\frac{4\pi}{3}} \right) \tag{3.6}$$

Insertion of (3.3) into (3.6) gives the following expression for the voltage vector

$$\vec{u}_1^{\alpha\beta} = \sqrt{\frac{2}{3}}\left(s_a V_{dc} + s_b V_{dc} e^{j\frac{2\pi}{3}} + s_c V_{dc} e^{j\frac{4\pi}{3}} + v_{link-} \underbrace{\left(e^{j0} + e^{j\frac{2\pi}{3}} + e^{j\frac{4\pi}{3}} \right)}_{=0} \right) \tag{3.7}$$

which can be simplified to

$$\vec{u}_1^{\alpha\beta} = \sqrt{\tfrac{2}{3}} V_{dc} \left(s_a + s_b e^{j\frac{2\pi}{3}} + s_c e^{j\frac{4\pi}{3}} \right) \tag{3.8}$$

since the zero-sequence component v_{link-} vanishes in the transformation as indicated in (3.7).

From (3.8) it can be concluded that, since the three switches can be combined in 2^3=8 ways, eight discrete voltage vectors may be generated by the three phase VSC. The voltage vector space for the three phase VSC is displayed in Figure 3.4. Here, the switching states for the corresponding voltage vectors are indicated by the notation $u_{s_a s_b s_c}$.

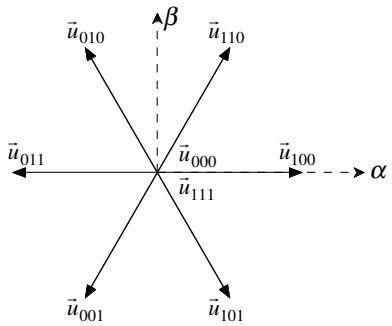

Figure 3.4 Voltage vector space for the three phase VSC.

The length of the voltage vectors are $\sqrt{\frac{2}{3}} V_{dc}$ according to (3.8), except for the zero voltage vectors obtained when all switching states are equal, i.e. the combinations 000 and 111.

Pulse Width Modulation

Pulse width modulation (PWM) methods are employed in order to determine the instantaneous switching states of the VSCs [15][34]. Usually, modulation of the VSCs are obtained through current control. In closed loop PWM techniques, the current control is included in the switching state generation, whereas open loop PWM is based on reference voltages obtained from current controllers. In the latter case, the reference voltages are then used to find the instantaneous switching states of the VSCs either by general space vector modulation or, in particular by carrier wave modulation.

Closed loop modulation by hysteresis control

Closed loop control of the VSCs is obtained by hysteresis or tolerance band current controllers. The principle of hysteresis controllers is to keep

the current within the hysteresis dead band. This is shown in Figure 3.5 together with the principle scheme of a hysteresis current controller.

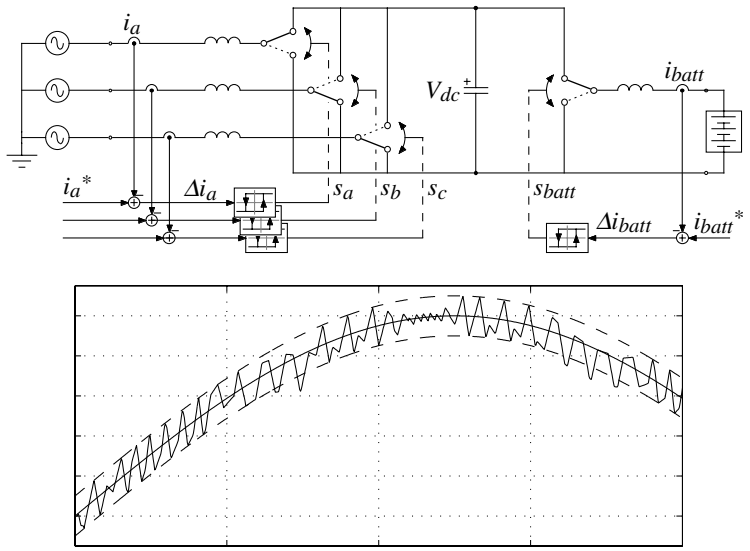

Figure 3.5 Top) Principle scheme of a hysteresis current controller. Bottom) Basic current waveform included the controller dead band (dashed).

The basic principles of hysteresis current controllers causes the current to be within the hysteresis dead band. This implies high dynamic performance, since the current is able to follow almost any reference current trajectory. Hence, hysteresis current controllers are very attractive in active filter applications. However, there are some inherent drawbacks with this control method [15] such as

- lack of intercommunication between the individual hysteresis controllers and therefore no strategy to generate zero voltage vectors.
- a tendency to lock into limit cycles of high frequency switching.
- generation of subharmonic current components.
- the current is not strictly limited by the hysteresis dead band as can be seen in Figure 3.5. This can happen whenever the grid voltage vector has an component that opposes the active switching state vector.

Anyway, the varying switching frequency complicates the converter design. Furthermore, the intended use of LCL-filters make hysteresis current control less practicable.

Open loop modulation by triangular carrier PWM

Open loop control of VSCs is usually obtained by carrier based PWM strategies. In Figure 3.6, the principle scheme and signal flow diagram for triangular carrier PWM VSCs with additional symmetrisation is shown. Here, the instantaneous switching states are generated from comparators, which compare the voltage references with the carrier signal. At the crossing instants of a voltage reference and the carrier signal, the corresponding switch state changes and commutation of the bridge leg is initiated.

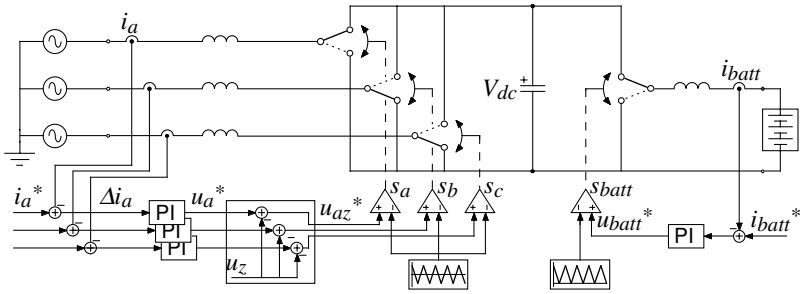

Figure 3.6 Signal flow diagram of carrier based PWM.

An important property of carrier based PWM techniques is determined by the frequency modulation ratio m_f defined in [27] as

$$m_f = \frac{f_{carrier}}{f_1} \tag{3.9}$$

where $f_{carrier}$ and f_1 are the carrier signal frequency and the fundamental grid frequency, respectively.

Accurate time average output voltages are obtained, if the amplitude of the carrier signal corresponds to the instantaneous DC-link voltage of the VSCs. Hence, the peak value of the carrier signal for the three phase VSC should be

$$\hat{u}_{carrier} = \frac{1}{2} V_{dc} \tag{3.10}$$

whereas the carrier signal used for the uni-polar half-bridge converter should vary between zero and V_{dc}.

Figure 3.7 shows in detail the logic control signal generation of triangular carrier PWM of a three phase VSC. Since high performance is equivalent

to a large m_f, which implies that the voltage references can be assumed constant during the carrier period as shown in the figure.

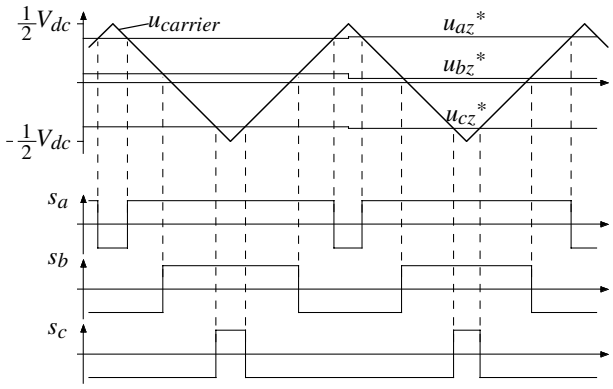

Figure 3.7 Detailed description of the logic control signal generation for a three phase VSC with triangular carrier PWM.

From Figure 3.7, it can be concluded that the switching frequency f_{sw} of the VSC is given by the carrier signal frequency, i.e.

$$f_{sw} = f_{carrier} \tag{3.11}$$

Symmetrisation of the phase voltage references, as indicated in Figure 3.6, by the subtraction of a zero-sequence component u_z given by

$$u_z = \frac{\max\left(u_a^*, u_b^*, u_c^*\right) + \min\left(u_a^*, u_b^*, u_c^*\right)}{2} \tag{3.12}$$

improves the performance of the PWM method [15][34]. The utilisation of the DC-link voltage increases and the current ripple decreases. Furthermore, the phase currents are equal to their average values at the triangular carrier end-points. Sampling of the phase currents at these instants reduces the need of average filters for control purposes in digital controllers. Hence, the sampling rate f_s and the corresponding sampling time T_s are given by

$$\begin{aligned} f_s &= 2 \cdot f_{carrier} \\ T_s &= \frac{1}{f_s} \end{aligned} \tag{3.13}$$

As stated before, a large m_f means that the frequency of the carrier signal is much higher than the grid frequency. Hence, only small changes in the voltage references occur between two periods of the carrier signal. This

means that the content of the frequency spectrum of the output voltages will be dominated by the content at f_{sw} and at multiples of f_{sw}, besides the fundamental grid frequency component. This is illustrated in Figure 3.8, where the normalised spectrum of the output voltage obtained by triangular carrier PWM with m_f equal to 99 corresponding to a switching frequency of 4950 Hz.

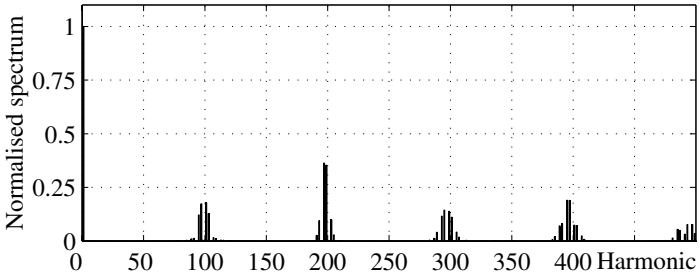

Figure 3.8 Normalised phase voltage spectrum of triangular carrier PWM VSC.

The well defined harmonic content of carrier based PWM makes the design of proper passive filters easier.

Average modelling

The fundamental properties of triangular carrier based PWM with symmetrisation imply the use of average modelling of the converters [23]. During each sampling interval, the average output voltages equal the reference voltages. Hence, the average output voltage of the half bridge converter is given by

$$\bar{u}_{1batt} = \bar{s}_{batt} V_{dc} = \left\{ 0 \le u^*_{1batt} \le V_{dc} \right\} \tag{3.14}$$

where the switching state average is referred to as the duty cycle or pulse ratio. The rightmost part of (3.14) indicates the limitation in output voltage due to the DC-link voltage restriction. Similar expressions are obtained for the average phase voltages of the three phase VSC, that is

$$\begin{cases} \bar{u}_{1a} = \left\{ -\frac{1}{2} V_{dc} \le u^*_{1az} \le \frac{1}{2} V_{dc} \right\} \\ \bar{u}_{1b} = \left\{ -\frac{1}{2} V_{dc} \le u^*_{1bz} \le \frac{1}{2} V_{dc} \right\} \\ \bar{u}_{1c} = \left\{ -\frac{1}{2} V_{dc} \le u^*_{1cz} \le \frac{1}{2} V_{dc} \right\} \end{cases} \tag{3.15}$$

still under the balanced constrint given by (3.4).

The average models of the VSCs are used in the performance analysis of the controller structures in the battery charger, since they enable time efficient simulation of the principle behaviour of the battery charger. Furthermore, the non-ideal properties of VSCs such as the semiconductor forward voltage drop and the blanking time effect may also be contained in the average model as described in [15].

3.3 DC-link

The DC-link capacitor C_{dc} provides an intermediate energy storage, which decouples the three phase VSC from the half bridge DC/DC converter. Hence, the VSCs can be operated independently of each other as long as the average power flow is balanced between the VSCs. The instantaneous difference in active power is stored in C_{dc}, which causes the DC-link voltage V_{dc} to vary. Hence, the value of C_{dc} is determined by the constraint on the maximum allowed DC-link voltage ripple ΔV_{dc}. The instantaneous DC-link capacitor current i_{Cdc} can be derived from Figure 3.3 and is given by

$$i_{Cdc} = -s_a i_a - s_b i_b - s_c i_c - s_{batt} i_{batt} \tag{3.16}$$

In [7], a thorough discussion on the limiting factors of the DC-link capacitor size is given. It is stated that the DC-link capacitor should be large enough to handle transients, i.e. load changes and tripping of circuit breakers, without any severe effect on the DC-link voltage. The energy handling capability of the DC-link capacitor should correspond to the excess energy stored in the passive filters.

However in shunt AF applications, the limiting factor of the DC-link capacitor size is determined by the instantaneous active power redirected by the shunt AF. This means that the instantaneous active power contained in the conditioning current is temporarily stored in the DC-link capacitor. The worst case corresponds to long periods of charging/discharging of the DC-link capacitor. This implies that load balancing at rated power of the negative-sequence current component gives the limiting design constraint on the DC-link capacitor size.

A design expression for the DC-link capacitor value is derived, based on simplified analysis of the instantaneous active power flow in the battery charger when performing load balancing at rated power. The instantaneous active power flow through the PCC can be expressed, in the synchronously rotating reference *dq*-frame oriented to the integral of the grid voltage vector, from (A.16) as

$$p_{PCC} = e_d i_d + e_q i_q = \{e_d \equiv 0\} = e_q i_q \tag{3.17}$$

where e_q and i_q are the q-axis components of the grid voltage vector and the injected negative-sequence current vector, respectively. Hence, they are given by

$$\begin{aligned} e_q &= E_n \\ i_q &= \Im m\left(\sqrt{3} I_n e^{-j2\omega_1 t}\right) = \sqrt{3} I_n \sin(-2\omega_1 t) \end{aligned} \tag{3.18}$$

where subscript n denotes nominal value and ω_1 is the fundamental angular frequency of the grid.

If the line filter and the three phase VSC are considered loss less, the instantaneous active power flow through the PCC should correspond to the power flow in the DC-link capacitor, i.e.

$$p_{Cdc} = i_{Cdc} V_{dc} = p_{PCC} \tag{3.19}$$

Substituting (3.17) into (3.19) and rearranging gives an expression for the average DC-link capacitor current i_{Cdc}

$$i_{Cdc} = \frac{e_q}{V_{dc}} i_q \tag{3.20}$$

The differential equation for the DC-link voltage can then be written

$$\tfrac{d}{dt} V_{dc} = \frac{1}{C_{dc}} \frac{e_q}{V_{dc}} i_q \tag{3.21}$$

Linearisation of (3.21) around the average DC-link voltage $\overline{V}_{dc}$ gives

$$\tfrac{d}{dt} \Delta V_{dc} = \frac{1}{C_{dc}} \frac{e_q}{\overline{V}_{dc}} i_q \tag{3.22}$$

where ΔV_{dc} corresponds to the DC-link voltage ripple. Substituting (3.18) into (3.22) and solving the differential equation, a design expression for the DC-link capacitor is found by rearrangement of the solution as

$$C_{dc} = \frac{S_n}{\overline{V}_{dc} \Delta V_{dc}} \frac{1}{2\omega_1} \tag{3.23}$$

where S_n is the rated power of the battery charger.

3.4 Line filter

As stated earlier, the line filter reduces the high frequency harmonic content of the battery charger line current, caused by the switched operation of the three phase VSC. Hence, sinusoidal line currents can be obtained. Usually, the line filter consists of filter inductors, i.e. L-filter, but by the use of additional capacitors and inductors, other filter combinations such as LC- or LCL-filters can be applied. In this section, however, only the L-filter and the LCL-filter configurations, shown in Figure 3.9, are investigated.

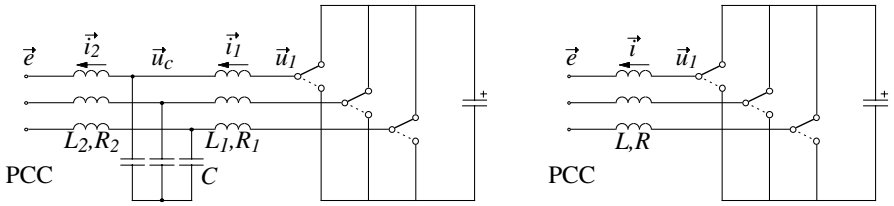

Figure 3.9 Line side of the battery charger with LCL-filter (left) and L-filter (right).

LCL-filter – Modelling

The differential equations of the LCL-filter in the stationary reference $\alpha\beta$-frame are

$$\begin{aligned}
\tfrac{d}{dt}\vec{i}_1^{\,\alpha\beta} &= -\frac{R_1}{L_1}\vec{i}_1^{\,\alpha\beta} + \frac{1}{L_1}\left(\vec{u}_1^{\,\alpha\beta} - \vec{u}_c^{\,\alpha\beta}\right) \\
\tfrac{d}{dt}\vec{u}_c^{\,\alpha\beta} &= \frac{1}{C}\left(\vec{i}_1^{\,\alpha\beta} - \vec{i}_2^{\,\alpha\beta}\right) \\
\tfrac{d}{dt}\vec{i}_2^{\,\alpha\beta} &= -\frac{R_2}{L_2}\vec{i}_2^{\,\alpha\beta} + \frac{1}{L_2}\left(\vec{u}_c^{\,\alpha\beta} - \vec{e}^{\,\alpha\beta}\right)
\end{aligned} \tag{3.24}$$

which are equivalently represented by the state space description

$$\tfrac{d}{dt}\begin{bmatrix} \vec{i}_1^{\,\alpha\beta} \\ \vec{u}_c^{\,\alpha\beta} \\ \vec{i}_2^{\,\alpha\beta} \end{bmatrix} = \underbrace{\begin{bmatrix} \frac{-R_1}{L_1} & \frac{-1}{L_1} & 0 \\ \frac{1}{C} & 0 & \frac{-1}{C} \\ 0 & \frac{1}{L_2} & \frac{-R_2}{L_2} \end{bmatrix}}_{\vec{A}_{LCL}^{\alpha\beta}} \begin{bmatrix} \vec{i}_1^{\,\alpha\beta} \\ \vec{u}_c^{\,\alpha\beta} \\ \vec{i}_2^{\,\alpha\beta} \end{bmatrix} + \underbrace{\begin{bmatrix} \frac{1}{L_1} & 0 \\ 0 & 0 \\ 0 & \frac{-1}{L_2} \end{bmatrix}}_{\vec{B}_{LCL}^{\alpha\beta}} \begin{bmatrix} \vec{u}_1^{\,\alpha\beta} \\ \vec{e}^{\,\alpha\beta} \end{bmatrix} \tag{3.25}$$

The frequency response of the LCL-filter is shown in Figure 3.10. Note the peak at the resonance frequency of the LCL-filter, which implies a poorly damped oscillatory behaviour. The use of triangular carrier based PWM, however, prevents the excitation of this resonance due to its advantageous frequency spectrum, refer to Figure 3.8. Anyway, the attenuation at the resonance frequency can be improved by damping resistors in series with the filter capacitors at the expense of the high frequency attenuation.

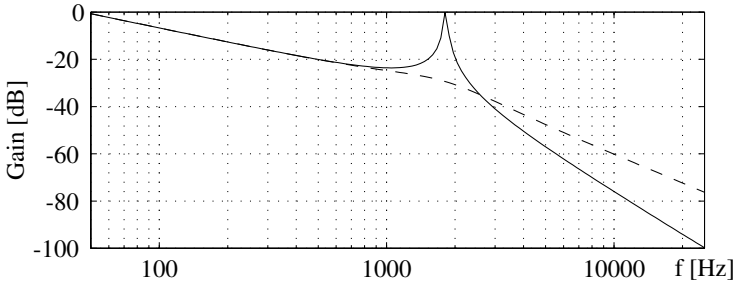

Figure 3.10 Frequency response from converter output voltage to output current (solid) and with damper resistors (dashed).

Transformation of the state space description in stationary coordinates into the synchronously rotating reference *dq*-frame is obtained by subtraction of the angle difference as described in Appendix A.2. This operation is equivalent to a shift in the frequency-domain [11]. The resulting state space description of the LCL-filter in synchronous coordinates is given by

$$\frac{d}{dt}\begin{bmatrix}\vec{i}_1^{\,dq}\\ \vec{u}_c^{\,dq}\\ \vec{i}_2^{\,dq}\end{bmatrix}=\underbrace{\begin{bmatrix}\frac{-R_1}{L_1}-j\omega_1 & \frac{-1}{L_1} & 0\\ \frac{1}{C} & -j\omega_1 & \frac{-1}{C}\\ 0 & \frac{1}{L_2} & \frac{-R_2}{L_2}-j\omega_1\end{bmatrix}}_{\vec{A}_{LCL}^{dq}}\begin{bmatrix}\vec{i}_1^{\,dq}\\ \vec{u}_c^{\,dq}\\ \vec{i}_2^{\,dq}\end{bmatrix}+\underbrace{\begin{bmatrix}\frac{1}{L_1} & 0\\ 0 & 0\\ 0 & \frac{-1}{L_2}\end{bmatrix}}_{\vec{B}_{LCL}^{dq}}\begin{bmatrix}\vec{u}_1^{\,dq}\\ \vec{e}^{\,dq}\end{bmatrix} \quad (3.26)$$

The complex valued state space description in synchronous coordinates indicates that the behaviour of the LCL-filter is dependent on the rotation direction of the vectors. A real valued state space description of (3.26) is obtained by separating the vector equations in their real and imaginary parts, i.e. *d*- and *q*-components, respectively. Hence, the LCL-filter is also described by the following state space system

$$\frac{d}{dt}\begin{bmatrix} i_{1d} \\ i_{1q} \\ u_{cd} \\ u_{cq} \\ i_{2d} \\ i_{2q} \end{bmatrix} = \underbrace{\begin{bmatrix} \frac{-R_1}{L_1} & \omega_1 & \frac{-1}{L_1} & 0 & 0 & 0 \\ -\omega_1 & \frac{-R_1}{L_1} & 0 & \frac{-1}{L_1} & 0 & 0 \\ \frac{1}{C} & 0 & 0 & \omega_1 & \frac{-1}{C} & 0 \\ 0 & \frac{1}{C} & -\omega_1 & 0 & 0 & \frac{-1}{C} \\ 0 & 0 & \frac{1}{L_2} & 0 & \frac{-R_2}{L_2} & \omega_1 \\ 0 & 0 & 0 & \frac{1}{L_2} & -\omega_1 & \frac{-R_2}{L_2} \end{bmatrix}}_{A_{LCL}^{dq}} \begin{bmatrix} i_{1d} \\ i_{1q} \\ u_{cd} \\ u_{cq} \\ i_{2d} \\ i_{2q} \end{bmatrix} + \underbrace{\begin{bmatrix} \frac{1}{L_1} & 0 & 0 & 0 \\ 0 & \frac{1}{L_1} & 0 & 0 \\ 0 & 0 & 0 & 0 \\ 0 & 0 & 0 & 0 \\ 0 & 0 & \frac{-1}{L_2} & 0 \\ 0 & 0 & 0 & \frac{-1}{L_2} \end{bmatrix}}_{B_{LCL}^{dq}} \begin{bmatrix} u_{1d} \\ u_{1q} \\ e_d \\ e_q \end{bmatrix} \quad (3.27)$$

LCL-filter – Design

The design of the passive filter is dependent on the attenuation needed in order to reduce the high frequency components of the line currents. Hence, the design inputs for the passive filter are the high frequency spectrum of the three phase VSC, shown in Figure 3.8, and the harmonic regulation to be fulfilled, for example the IEC 1000-3-4 regulation on current harmonic emissions into the power grid. The IEC 1000-3-4 regulation states that current harmonics above the 33rd should be less than 0.6 % of the nominal current, i.e.

$$I_h \leq 0.6\% \text{ of } I_n \text{ for } h \geq 33 \quad (3.28)$$

The design expressions for the LCL-filter are derived from the analysis of an idealised LCL-filter, where the series resistance of the inductors are neglected. The relationship between the converter output voltage and the line current in stationary coordinates is given by the transfer function $G^{\alpha\beta}(s)$ derived from (3.25), with R_1 and R_2 set to zero, that is

$$G^{\alpha\beta}(s) = \begin{bmatrix} 0 & 0 & 1 \end{bmatrix} \left(sI - \vec{A}_{LCL}^{\alpha\beta} \right)^{-1} \vec{B}_{LCL}^{\alpha\beta} \begin{bmatrix} 1 \\ 0 \end{bmatrix} = \frac{\frac{1}{L_1 L_2 C}}{s\left(s^2 + \frac{L_1 + L_2}{L_1 L_2 C} \right)} \quad (3.29)$$

where s denotes the Laplace operator. The corresponding fourier transform $G^{\alpha\beta}(j\omega)$ is obtained from (3.29) by the substitution of the Laplace operator s with $j\omega$. Hence, the gain function $|G^{\alpha\beta}(j\omega)|$ of the

LCL-filter for each harmonic, i.e. replacing ω with $h\omega_1$, can thus be expressed by

$$\left|G^{\alpha\beta}(jh\omega_1)\right| = \frac{\dfrac{1}{L_1 L_2 C}}{h\omega_1 \left| -h^2 {\omega_1}^2 + \dfrac{L_1 + L_2}{L_1 L_2 C} \right|} \tag{3.30}$$

From (3.30) it is clear that several combinations of the filter parameters, i.e. L_1, L_2 and C, can fulfil the harmonic content constraint of the line current. Additional requirements, such as the ratio between the inner and outer inductors and the idle production of reactive power by the filter, are needed to derive a design expression. In [23], it is stated that the ratio between the inductors is a trade off between low resonance frequency and low current ripple in the inner inductor L_1. From [23], a good compromise is obtained if the inner inductor is twice the size of the outer inductor. Furthermore, an idle reactive current of 5 % of the nominal line current is considered reasonable. Hence, the additional requirements are given by

$$\begin{aligned} L_1 &= 2L_2 \\ C &= 0.05 C_{base} \end{aligned} \tag{3.31}$$

where C_{base} is defined in Appendix B.1.

Substituting (3.31) into (3.30) and solving for the outer inductor L_2 finally gives a design expression for the LCL-filter

$$L_2 = \max_h \left(\frac{3}{4Ch^2\omega_1^2} + \sqrt{\left(\frac{3}{4Ch^2\omega_1^2} \right)^2 + \frac{U_{phase,h}}{h\omega_1 I_{h\max}}} \right) \tag{3.32}$$

where $U_{phase,h}$ represents the rms-value of the output phase voltage harmonics given in Figure 3.8. Note that the given design expression is only valid for harmonics above the resonance frequency of the LCL-filter, refer to Figure 3.10.

L-filter – Modelling and design

As described previously, the passive filter usually consists only of filter inductors thus forming a L-filter. The L-filter is described by the vector differential equation in stationary coordinates

$$\frac{d}{dt}\vec{i}^{\,\alpha\beta} = -\frac{R}{L}\vec{i}^{\,\alpha\beta} + \frac{1}{L}\left(\vec{u}_1^{\,\alpha\beta} - \vec{e}^{\,\alpha\beta}\right) \tag{3.33}$$

or in synchronous coordinates by the complex valued vector differential equation

$$\frac{d}{dt}\vec{i}^{\,dq} = -\left(\frac{R}{L} + j\omega_1\right)\vec{i}^{\,dq} + \frac{1}{L}\left(\vec{u}_1^{\,dq} - \vec{e}^{\,dq}\right) \tag{3.34}$$

The complex valued representation of the L-filter is transformed into a real valued state space system in synchronous coordinates by separating (3.34) into its real and imaginary parts, that is

$$\frac{d}{dt}\begin{bmatrix} i_d \\ i_q \end{bmatrix} = \underbrace{\begin{bmatrix} -\frac{R}{L} & \omega_1 \\ -\omega_1 & -\frac{R}{L} \end{bmatrix}}_{A_L^{dq}}\begin{bmatrix} i_d \\ i_q \end{bmatrix} + \underbrace{\begin{bmatrix} \frac{1}{L} & 0 \\ 0 & \frac{1}{L} \end{bmatrix}}_{B_L^{dq}}\begin{bmatrix} u_{1d} \\ u_{1q} \end{bmatrix} + \underbrace{\begin{bmatrix} -\frac{1}{L} & 0 \\ 0 & -\frac{1}{L} \end{bmatrix}}_{-B_L^{dq}}\begin{bmatrix} e_d \\ e_q \end{bmatrix} \tag{3.35}$$

The previous discussion on the design of the LCL-filter can be applied also to the L-filter. Hence, a design expression for the inductance L based on the same requirements as for the LCL-filter case is given by

$$L = \max_h\left(\frac{U_{phase,h}}{h\omega_1 I_{h\max}}\right) \tag{3.36}$$

Comparing the properties of L- and LCL-filters

The advantageous characteristics of the LCL-filter compared to the L-filter are found from the frequency responses plotted in Figure 3.11. The filter parameters are obtained from the design expressions given by (3.31) and (3.32) for the LCL-filter and (3.36) for the L-filter. Hence, both filters fulfil the harmonic current constraint.

In the high frequency region (>2.5 kHz), the attenuation increases with 60 dB/decade for the LCL-filter compared to the 20 dB/decade for the L-filter. Hence, the higher order current harmonics are better attenuated by the LCL-filter and thus the total high frequency harmonic distorsion is lower for the LCL-filter case.

In the low frequency region (<1 kHz), the slope of the frequency responses are both 20 dB/decade. This implies that the LCL-filter can be regarded as a virtual inductor with an inductance of L_1+L_2, refer to (3.29). However, the difference in the attenuation further indicates that

the sum L_1+L_2 is smaller than the L-filter inductance L. Consequently, the voltage drop across the LCL-filter, caused by the injected current harmonics, is lower compared to the L-filter case. This is the key advantage of the LCL-filter, which is especially important in an active filter application. Furthermore, the lower voltage drop across the LCL-filter implies that the required DC-link voltage is lower. Hence, a greater semiconductor margin can be obtained, i.e. the ratio between the operating and the rated voltage levels of the IGBTs.

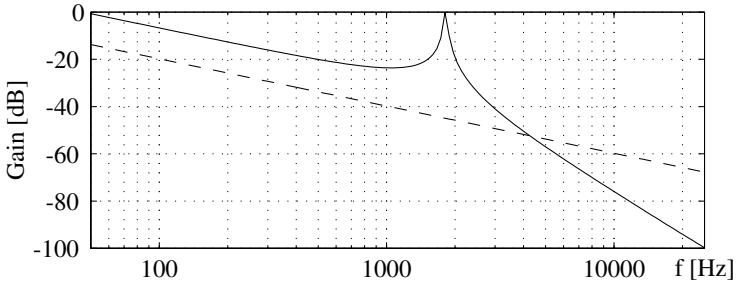

Figure 3.11 Frequency responses, LCL-filter (solid) and L-filter (dashed), from converter output voltage to line current.

The major drawbacks of the LCL-filter are the high current ripple in the inner inductor L_1 and the increased number of transducers needed for control purposes. The high current ripple in L_1 results in high amount of iron losses, i.e. hysteresis and eddy current losses, which implies the use of thin laminated iron cores or even iron powder cores. Also, the extended complexity increases the requirements on the signal electronics and the control system. Furthermore, the reactive power requirements of the filter capacitors have to be accommodated by the converter as to prohibit reactive grid currents when the unit is operating under idle conditions.

3.5 Battery filter

The battery filter in Figure 3.1 also consists of a LCL-filter. The intention is to reduce the physical size of the filter, since the total inductance of a LCL-filter is smaller than for a L-filter inductance. However, the large current ripple in the inner inductor L_1 implies high amount of iron losses, and hence larger iron cores are needed in order to reduce the thermal problems. Anyway, the advantageous high frequency characteristics of the LCL-filter, i.e. the 60 dB/decade slope, further motivates the use of the LCL-filter.

Modelling

The state space description of the single phase LCL-filter is given by

$$\frac{d}{dt}\begin{bmatrix} i_1 \\ u_c \\ i_2 \end{bmatrix} = \underbrace{\begin{bmatrix} -\frac{R_1}{L_1} & -\frac{1}{L_1} & 0 \\ \frac{1}{C} & 0 & -\frac{1}{C} \\ 0 & \frac{1}{L_2} & -\frac{R_2}{L_2} \end{bmatrix}}_{A_{LCL}} \begin{bmatrix} i_1 \\ u_c \\ i_2 \end{bmatrix} + \underbrace{\begin{bmatrix} \frac{1}{L_1} & 0 \\ 0 & 0 \\ 0 & -\frac{1}{L_2} \end{bmatrix}}_{B_{LCL}} \begin{bmatrix} u_1 \\ V_{batt} \end{bmatrix} \quad (3.37)$$

where the same quantity notation as for the line filter are used, i.e. i_1 and i_2 are the currents in the inner and outer inductors L_1 and L_2, respectively. Also, u_1 and u_c are the DC-DC converter output voltage and filter capacitor voltage, respectively.

In Figure 3.12, the frequency responses for the single phase LCL-filter obtained from (3.37) are displayed. The corresponding frequency response of a L-filter is also shown in the figure.

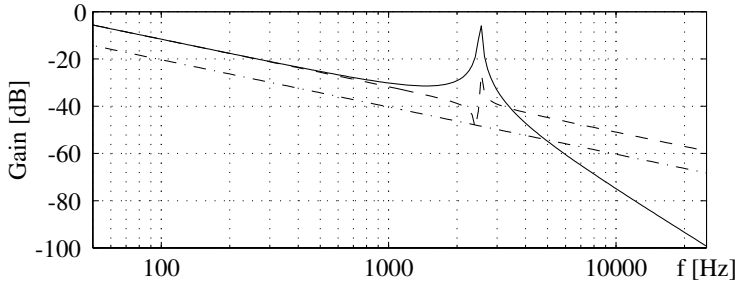

Figure 3.12 Frequency responses from converter output voltage to currents i_2 and i_1, LCL-filter (i_2 solid and i_1 dashed) and L-filter (dash dotted).

Design

The design procedure for the battery side LCL-filter resembles the one used for the line filter. That is, knowledge of the frequency spectrum of the DC-DC converter output voltage and the allowed battery current ripple gives the required overall attenuation of the LCL-filter. The lack of standardisation implies that no regulation on charging current ripple exist. However, a charging current ripple of 10 % peak to peak of the nominal current is considered reasonable and hence the current ripple constraint is given by

$$\Delta\hat{i}_{batt} \le 0.05\, I_{batt,n} \tag{3.38}$$

Consider the principle voltage and current waveforms of the LCL filter in Figure 3.13. The half bridge converter output voltage consists of equidistant pulses of constant duration t_p. Hence, the converter output voltage u_1 can be expressed analytically by the trigonometric fourier series

$$u_1(t) = D \cdot V_{dc} + \sum_{h=1}^{\infty} \frac{2V_{dc}\,\sin(h\pi \cdot D)}{h\pi} \cos(h\omega_{sw} t) \tag{3.39}$$

where D is the duty cycle or pulse ratio defined by

$$D = \frac{t_p}{T_{sw}} \tag{3.40}$$

Note the difference in the i_1 and i_2 current waveforms shown in Figure 3.13, which is due to the high frequency characteristics of the LCL-filter shown in Figure 3.12. The almost sinusoidal i_2 current is a consequence of the slope of 60 dB/decade in the frequency response of the LCL-filter and the inverse proportionality to frequency of the converter voltage spectrum. Therefore, the design of the LCL-filter should be derived for the switching frequency and for a duty cycle D of 0.5, since this corresponds to the highest amplitude which is concluded from (3.39).

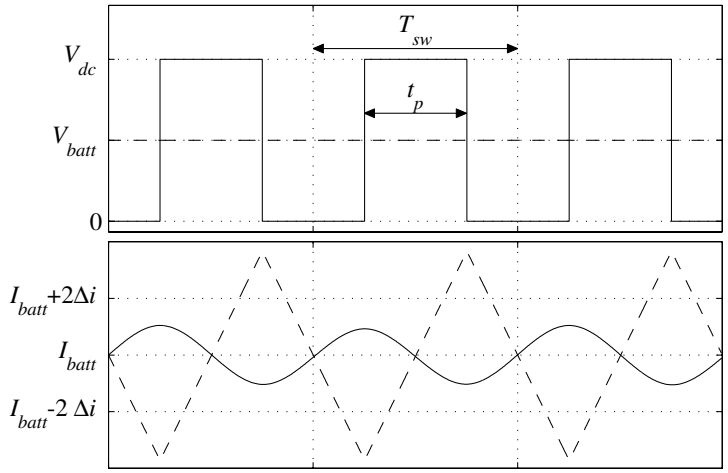

Figure 3.13 Principle waveforms of the battery side. Top) u_1 (solid) and V_{batt} (dashed), and bottom) i_2 (solid) and i_1 (dashed).

The transfer functions from converter output voltage u_1 to the inner and outer inductor currents i_1 and i_2 are obtained from (3.37) and given by

$$G_{i_1}(s) = \frac{\left(s^2 + \frac{1}{L_2 C}\right)\frac{1}{L_1}}{s\left(s^2 + \frac{L_1 + L_2}{L_1 L_2 C}\right)} \tag{3.41}$$

$$G_{i_2}(s) = \frac{\frac{1}{L_1 L_2 C}}{s\left(s^2 + \frac{L_1 + L_2}{L_1 L_2 C}\right)} \tag{3.42}$$

where the series resistance of the inductors are neglected. The attenuation at the switching frequency can be obtained from (3.41) and (3.42) by replacing s with $j\omega_{sw}$, which gives

$$\left|G_{i_1}(j\omega_{sw})\right| = \frac{\left(\omega_{sw}^2 - \frac{1}{L_2 C}\right)\frac{1}{L_1}}{\omega_{sw}\left(\omega_{sw}{}^2 - \frac{L_1 + L_2}{L_1 L_2 C}\right)} \tag{3.43}$$

$$\left|G_{i_2}(j\omega_{sw})\right| = \frac{\frac{1}{L_1 L_2 C}}{\omega_{sw}\left(\omega_{sw}{}^2 - \frac{L_1 + L_2}{L_1 L_2 C}\right)} \tag{3.44}$$

In the derivation of design expressions for the LCL-filter, two additional requirements have been applied. First, the filter capacitor has been chosen equal to the filter capacitors of the line filter. Second, a constraint also on the current ripple in the inner inductor implies control of the stresses applied to the inner inductor and the DC-DC converter. This ease up the manufacturing of these components. Hence, the additional requirements are given by

$$\begin{aligned} \left|G_{i_1}(j\omega_{sw})\right| &= x \cdot \left|G_{i_2}(j\omega_{sw})\right| \\ C &= 0.05\, C_{base} \end{aligned} \tag{3.45}$$

where the factor x is given by the selected constraint on the current ripple of the inner inductor. From (3.43) to (3.45) the design expressions for the inductors can be derived as

$$L_1 = \frac{2V_{dc}}{x\,\omega_{sw}\,\pi\,\Delta\hat{i}_{batt}} + \frac{x+1}{x\;\omega_{sw}^2\;C} \tag{3.46}$$

$$L_2 = \frac{x+1}{\omega_{sw}^2\;C} \tag{3.47}$$

In the thesis, the factor x is selected to 3. This should imply that the current ripple in the inner inductor is three times the current ripple in the outer inductor. However, as can be seen in Figure 3.13, the actual current ripple in i_1 is somewhat higher. This is due to the contribution of the higher order harmonics, refer to (3.39), which are more efficiently attenuated in the outer inductor case.

3.6 Target system specification

The general specification of the target system investigated in the thesis is listed in Table 3.1. Hence, the investigated battery charger is the same as the one designed and tested in [5], except for the rated power which is 10 kVA in this case but 75 kVA in [5].

Table 3.1 General specification of the battery charger.

rated power	S_n	10 kVA
grid voltage	E_n	400 V
grid frequency	f_1	50 Hz
battery voltage	V_{batt}	375 V
battery current	$I_{batt,n}$	26.67 A

Note that the battery current is limited either by the nominal current or by the rated power listed in Table 3.1.

In Table 3.2, the parameters of the VSCs and the DC-link are listed. Furthermore, as indicated previously triangular carrier based PWM modulation is used, which implies that the switching frequency and also the controller sampling time are fixed. Synchronous sampling at the carrier wave end-points, refer to the discussion given in Section 3.2, is employed.

Note that the actual DC-link capacitor value is not selected according to the design expression (3.23). The main reason for the larger value is to

improve the robustness of the physical implementation, described in Chapter 6. Anyway, the effect is that the specified peak to peak DC-link voltage ripple is reduced to 2.5 % of the nominal DC-link voltage.

Table 3.2 Parameters of the voltage source converters, including the DC-link.

DC-link voltage	V_{dc}		750 V
DC-link voltage ripple	ΔV_{dc}	peak-peak	10 % of V_{dc}
DC-link capacitor	C_{dc}	design	570 µF
		actual	2.2 mF
switching frequency	f_{sw}		4.88 kHz
sampling time	T_s		102.4 µs

The parameters of the line filter is given in Table 3.3. The design inputs are the IEC 1000-3-4 regulation on current harmonic emissions (3.28) and the converter voltage spectrum, refer to Figure 3.8. Note that an additional 10 % margin is applied on the inductor values used in the actual charger. The equivalent series resistances correspond to the winding resistance of the inductors used in the experimental set-up, refer to Chapter 6.

Table 3.3 Parameters of the line filter.

LCL-filter	L_1	design	2.0 mH
		actual	2.2 mH
	R_1		75 mΩ
	C	design	10 µF
		actual	10 µF
	L_2	design	1.0 mH
		actual	1.15 mH
	R_2		66 mΩ
L-filter	L	design	15.6 mH

The corresponding inductance of an equivalent L-filter is also given in Table 3.3. The larger value of this inductance in comparison to the total inductance of the LCL-filter indicates the advantageous low frequency characteristics of the LCL-filter, refer to the discussion given in Section 3.4.

The parameters of the LCL-filter applied on the battery side is listed in Table 3.4, where the design is according to the discussion given in Section 3.5. In this design, the maximum allowed charging current ripple is given

by (3.38). Furthermore, the corresponding inductance of a L-filter is also given in the table.

Table 3.4 Parameters of the battery filter.

LCL-filter	L_1	design	5.6 mH
		actual	5.3 mH
	R_1		57.2 mΩ
	C	design	10 µF
		actual	10 µF
	L_2	design	0.414 mH
		actual	0.415 mH
	R_2		19 mΩ
L-filter	L	design	16.3 mH

4

Control

In this chapter the overall control structure of the battery charger is presented. Model based controller synthesis is applied. Furthermore, extensive analysis of the performance characteristics is given with emphasis on stability and frequency domain characteristics.

4.1 Overall control

The overall control structure in the battery charger consists of a DC-link voltage controller, a battery current controller, and a line current controller, refer to Figure 4.1.

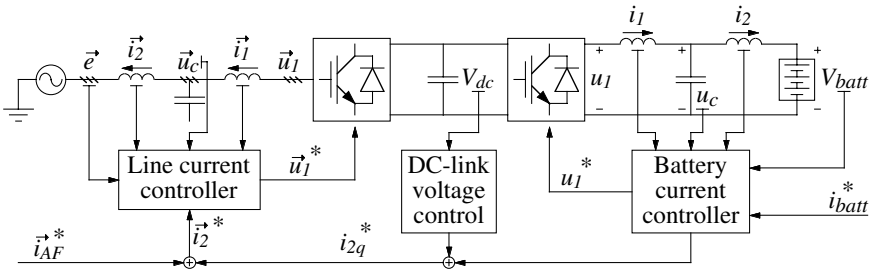

Figure 4.1 Overall control structure of the battery charger.

The DC-link voltage controller balances the active power flow in the battery charger. This is obtained by controlling the active current component on the line side. In order to avoid conflict with the active filter function of the battery charger, the bandwidth of the DC-link voltage controller has to be low. However, feed forward of the battery current implies faster response to changes in the battery current, and hence reducing the DC-link voltage deviation during transients.

The battery current controller consists of a model based cascade controller. The cascade controller is composed of an outer current control loop for the battery current, i.e. current i_2, an intermediate voltage controller for the filter capacitor voltage, and finally an inner current control loop for the i_1 current. The cascade configuration enables the use

of basic P- and PI-controllers, where the gain of the proportional parts are derived from the model representation of the battery filter, described in section 3.5.

The line side current controller resembles the cascade controller structure of the battery current controller. However, the line current controller is implemented in the synchronously rotating reference *dq*-frame oriented to the integral of the grid voltage vector as described in Appendix A.2. Hence, individual controllers for the active and reactive current components with additional compensation for the cross-coupling of the *d*- and *q*-axis quantities are obtained. Synchronous coordinates further utilise the use of integrators in the controller structure in order to eliminate the steady state errors of the fundamental current components.

4.2 Battery current control

A model based discrete cascade controller for the battery current is obtained by applying Euler approximations to the differential equations of the LCL-filter (3.37). By assuming dead beat response in each P-controller, the following discrete controller is derived

$$\begin{aligned} u_c^*(k) &= k_{i2}\frac{L_2}{T_s}\left(i_2^*(k)-i_2(k)\right)+R_2\cdot i_2(k)+V_{batt}(k) \\ i_1^*(k) &= k_{uc}\frac{C}{T_s}\left(u_c^*(k)-u_c(k)\right)+i_2^*(k) \\ u_1^*(k) &= k_{i1}\frac{L_1}{T_s}\left(i_1^*(k)-i_1(k)\right)+R_1\cdot i_1(k)+u_c(k) \end{aligned} \tag{4.1}$$

where k indicates the time for the sampling instants according to $t_k=kT_s$.

The controller structure in (4.1) consists of three cascaded P-controllers with additional feed forward and feed back terms given by the LCL-filter model. In order to stabilise the controller, the gain of the P-parts are altered from the dead beat gain by the constants k_{i1}, k_{uc} and k_{i2}. Proper values for these are then obtained from the stability analysis.

The controller in (4.1) is further modified in three steps to fit the application. First, the discrete controller is implemented in a digital signal processor (DSP), which gives a time delay of one sample due to the calculation time. The calculation delay causes additional phase deviation of the system. This decreases the stability margin and hence the bandwidth of the controlled system has to be reduced. However, compensation for the

time delay is accomplished by adopting the Otto-Smith controller [9] for systems with time delays as described in [22]. Second, the feed back of the resistive voltage drops are replaced by an integrator in the outer current control loop. The integrator reduces the steady state error of the DC-quantity of the battery current as well as compensates for uncertainties in the model.

Third, if the gain of the inner current and capacitor voltage P-controllers are chosen according to

$$k_{i1}\frac{L_1}{T_s}\cdot k_{uc}\frac{C}{T_s}=1 \tag{4.2}$$

then the effect of the capacitor voltage dynamics are cancelled. Hence, no measurement of the capacitor voltage is needed for control purposes.

The final discrete current control algorithm employed to the battery charger is therefore given by

$$\begin{aligned} u_c^*(k) &= k_{i2}\frac{L_2}{T_s}\left((i_2^*(k)-i_2(k))+\sum\Delta i_2(k)\right)+V_{batt}(k)\\ i_1^*(k) &= i_2^*(k)+i_{smith}(k)\\ u_1^*(k) &= k_{i1}\frac{L_1}{T_s}\left(i_1^*(k)-i_1(k)\right)+u_c^*(k) \end{aligned} \tag{4.3}$$

where the variable $\sum\Delta i_2$ corresponds to the integral part and is given by

$$\sum\Delta i_2(k+1)=\frac{T_s}{L_2/R_2}\cdot\left(i_2^*(k)-i_2(k)\right)+\sum\Delta i_2(k) \tag{4.4}$$

The delay compensation (Smith predictor) algorithm employed to the inner current control loop is given by

$$\begin{aligned} s_p(k+1) &= \left(1-\frac{R_1T_s}{L_1}\right)s_p(k)+\frac{T_s}{L_1}u_1(k)\\ i_{smith}(k+1) &= \frac{R_1T_s}{L_1}s_p(k)-\frac{T_s}{L_1}u_1(k) \end{aligned} \tag{4.5}$$

The block diagram representation of the discrete battery current controller, including the Smith predictor, is displayed in Figure 4.2.

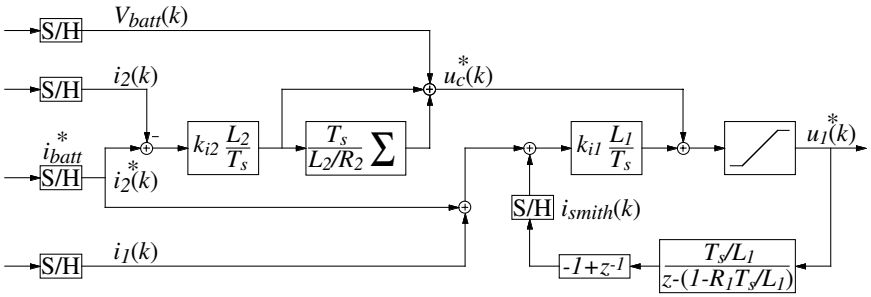

Figure 4.2 Block diagram representation of the discrete battery current controller.

The characteristics of the Smith predictor are fully utilised if its input corresponds to the output voltage of the half bridge converter. Since the DC-link voltage limits the converter output voltage, refer to (3.14), the same limitation should be applied to the feed back of the voltage reference. This is obtained by limiting the voltage reference, which is indicated in the block diagram by the saturation block.

Analysis

In order to analyse the battery current controller, the closed loop system of the controller and the LCL-filter has to be derived. The discrete controller implies that a discrete time model of the LCL-filter (3.37) has to be used.

The state vector x and input vector u of (3.37) are defined according to

$$x = \begin{bmatrix} i_1 & u_c & i_2 \end{bmatrix}^T \tag{4.6}$$

$$u = \begin{bmatrix} u_1 & V_{batt} \end{bmatrix}^T \tag{4.7}$$

The continuous state space system of the LCL-filter (3.37) can be described by the discrete-time model

$$\begin{aligned} x(k+1) &= \Phi_{LCL}\, x(k) + \begin{bmatrix} \Gamma_{LCL}^{u_1} & \Gamma_{LCL}^{V_{batt}} \end{bmatrix} u(k) \\ i_2(k) &= C_{LCL}\, x(k) \end{aligned} \tag{4.8}$$

where the system matrices are given according to [37] as

$$\Phi_{LCL} = e^{A_{LCL}T_s} \tag{4.9}$$

$$\begin{bmatrix} \Gamma_{LCL}^{u_1} & \Gamma_{LCL}^{V_{batt}} \end{bmatrix} = \int_0^{T_s} e^{A_{LCL}h}\, dh \cdot B_{LCL} \tag{4.10}$$

and the output matrix is

$$C_{LCL} = \begin{bmatrix} 0 & 0 & 1 \end{bmatrix} \tag{4.11}$$

The computational delay in the discrete controller implies that the converter output voltage corresponds to the reference voltage delayed by one sample, that is

$$u_1(k+1) = u_1^*(k) \tag{4.12}$$

The closed loop discrete state space system of the controller and the LCL-filter is derived based on the extended state vector X and the input vector U, defined according to

$$X = \begin{bmatrix} i_1 & u_c & i_2 & u_1 & s_p & \sum \Delta i_2 \end{bmatrix}^T \tag{4.13}$$

$$U = \begin{bmatrix} V_{batt} & i_2^* \end{bmatrix}^T \tag{4.14}$$

Note that the converter output voltage is represented as a state variable in the closed loop system due to the computational delay (4.12). Further on, the discrete control algorithm of (4.3) can interpreted as a linear state feed back controller with feed forward of the inputs according to

$$u_1^*(k) = \begin{bmatrix} L_x & L_{u_1} & L_{s_p} & L_{\sum i_2} \end{bmatrix} X(k) + \begin{bmatrix} L_{V_{batt}} & L_{i_2 *} \end{bmatrix} U(k) \tag{4.15}$$

where the individual feed back elements of (4.15) are found from (4.3), (4.4) and (4.5)

$$L_x = \begin{bmatrix} -k_{i1} \dfrac{L_1}{T_s} & 0 & -k_{i2} \dfrac{L_2}{T_s} \end{bmatrix} \tag{4.16}$$

$$L_{u_1} = -\frac{T_s}{L_1} \cdot \left(k_{i1} \frac{L_1}{T_s} \right) = -k_{i1} \tag{4.17}$$

$$L_{s_p} = \frac{R_1 T_s}{L_1} \cdot \left(k_{i1} \frac{L_1}{T_s} \right) = k_{i1} R_1 \tag{4.18}$$

$$L_{\sum i_2} = k_{i2} \frac{L_2}{T_s} \tag{4.19}$$

$$L_{V_{batt}} = 1 \tag{4.20}$$

$$L_{i_2*} = k_{i2}\frac{L_2}{T_s} + k_{i1}\frac{L_1}{T_s} \tag{4.21}$$

The closed loop system is then given by the extended discrete state space system

$$\begin{aligned} X(k+1) &= \begin{bmatrix} \Phi_{LCL} & \Gamma_{LCL}^{u_1} & 0 & 0 \\ L_x & L_{u_1} & L_{s_p} & L_{\sum i_2} \\ 0 & S_{u_1} & S_{s_p} & 0 \\ I_x & 0 & 0 & 1 \end{bmatrix} X(k) + \begin{bmatrix} \Gamma_{LCL}^{V_{batt}} & 0 \\ L_{V_{batt}} & L_{i_2*} \\ 0 & 0 \\ 0 & I_{i_2*} \end{bmatrix} U(k) \\ i_2(k) &= \begin{bmatrix} C_{LCL} & 0 & 0 & 0 \end{bmatrix} X(k) \end{aligned} \tag{4.22}$$

where the additional non-zero elements are

$$S_{u_1} = \frac{T_s}{L_1} \tag{4.23}$$

$$S_{s_p} = 1 - \frac{R_1 T_s}{L_1} \tag{4.24}$$

$$I_x = \begin{bmatrix} 0 & 0 & -\dfrac{T_s}{L_2/R_2} \end{bmatrix} \tag{4.25}$$

$$I_{i_2*} = \frac{T_s}{L_2/R_2} \tag{4.26}$$

Stability analysis of the closed loop system finally gives the proper values for the gain constants k_{i1} and k_{i2} of the P-controllers in the cascaded controller. Here, the root locus method [37] is applied on the closed loop system. The root locus method is convenient for sensitivity analysis with respect to the gain of the P-controllers. The stability boundary for discrete time systems is defined by the unit circle. Hence, if the poles of the closed loop system, i.e. the eigenvalues of the state matrix in (4.22), are inside the unit disc, the discrete system is considered stable.

In Figure 4.3 the root locus of the closed loop system is shown, when both k_{i1} and k_{i2} are altered. Since the complex poles appear in conjugated pairs, only the upper half of the unit disc is displayed. From the root locus it can be concluded that a high gain in the inner current control loop, that is close to the dead beat gain, implies an unstable or oscillatory behaviour.

Further on, a low value of the gain in the outer current control loop, i.e. k_{i2} lower than the dead beat gain, has the same effect. As a conclusion it is stated that the gain of the inner control loop should be well below dead beat gain, whereas the gain of the outer loop should be chosen some times higher than the dead beat gain.

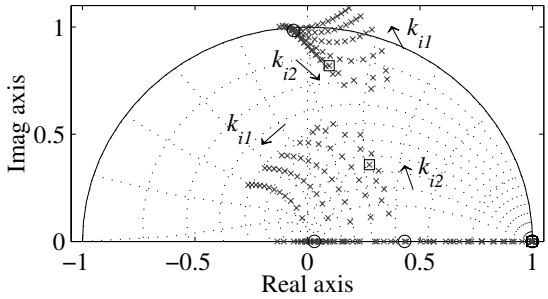

Figure 4.3 Root locus for the closed loop system for k_{i1}=[0.05…1] and k_{i2}=[0.5…7]; circle) k_{i1}=0.5 and k_{i2}=1, square) k_{i1}=0.1 and k_{i2}=5.

In Figure 4.4, the transfer functions from battery current reference i_2^* to battery current i_2 are shown for two sets of gain constants. The first set of gain constants are chosen as k_{i1}=0.5 and k_{i2}=1, whereas for the second set they are k_{i1}=0.1 and k_{i2}=5. The poles corresponding to these sets of gain constants are marked in Figure 4.3 with circles and squares, respectively.

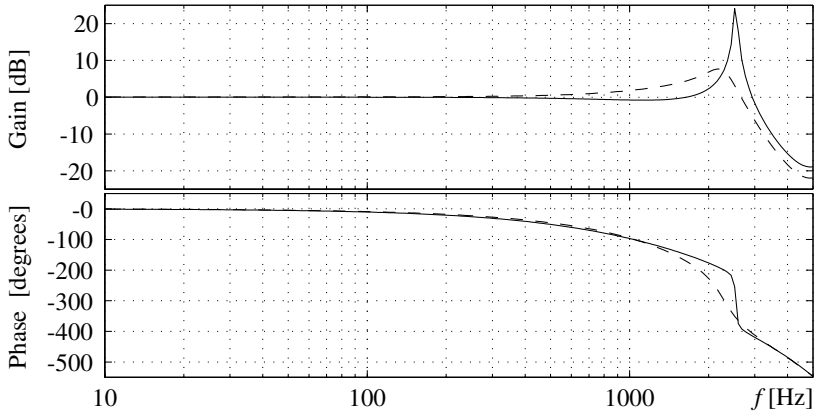

Figure 4.4 Frequency response from reference current to battery current (i_2^* to i_2), solid) k_{i1}=0.5 and k_{i2}=1, and dashed) k_{i1}=0.1 and k_{i2}=5.

The suppression of the resonance peak provided by the second set of gain constants implies a less oscillatory behaviour, which confirms the conclusions drawn from the root locus plot. Since the bandwidth of the

systems are almost the same, the second set of gain constants, that is k_{i1}=0.1 and k_{i2}=5, are chosen.

Simulation

Simulation of the battery side of the charger confirms the less oscillatory behaviour with the second set of gain constants, as shown in Figure 4.5. However, the oscillation does not seem to appear in the inner inductor current i_1. This implies that the oscillation originates from the outer inductor and the filter capacitor. Since the gain in the outer current control loop is low for the first set of gain constants, the controller is not able to generate counter actions to the oscillations. However, the higher gain provided by the second set of gain constants is sufficient in order to dampen the oscillations.

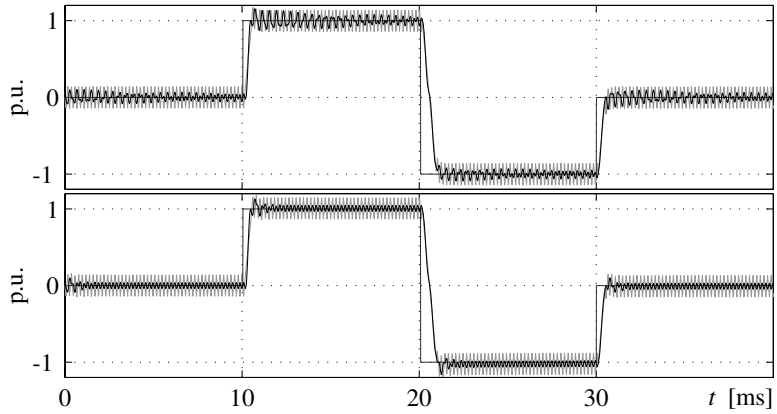

Figure 4.5 Battery side currents i_2^* (dark grey), i_2 (black), and i_1 (light grey). Top: k_{i1}=0.5 and k_{i2}=1, and bottom: k_{i1}=0.1 and k_{i2}=5.

4.3 Line current control

The derivation procedure of the line current controller resembles the one used for the battery current controller. The line current controller consists of a model based cascade control structure as was the case for the battery current controller. However, the line current controller is implemented in the synchronously rotating reference *dq*-frame oriented to the integral of the grid voltage vector as described in Appendix A.2.

In synchronous coordinates, the reactive and active quantities are related to the *d*- and *q*-axis components, respectively. Hence, individual controllers for the active and reactive quantities with additional compensation for the cross-coupling of the *d*- and *q*-axis components are

obtained. Synchronous coordinates further utilise the use of integrators in the controller structure in order to eliminate the steady state errors of the fundamental current components.

Applying Euler approximations to the differential equations given in (3.26) for the LCL-filter in synchronous coordinates and by assuming dead beat response, the derived discrete line current controller in complex vector notation is given by

$$\begin{aligned}
\vec{u}_c^{\,*}(k) &= k_{i2}\frac{L_2}{T_s}\left(\left(\vec{i}_2^{\,*}(k)-\vec{i}_2(k)\right)+\sum\Delta\vec{i}_2(k)\right)+(R_2+j\omega_1 L_2)\vec{i}_2(k)+\vec{e}(k)\\
\vec{i}_1^{\,*}(k) &= k_{uc}\frac{C}{T_s}\left(\vec{u}_c^{\,*}(k)-\vec{u}_c(k)\right)+j\omega_1 C\vec{u}_c(k)+\vec{i}_2^{\,*}(k)+\vec{i}_{smith}(k)\\
\vec{u}_1^{\,*}(k) &= k_{i1}\frac{L_1}{T_s}\left(\vec{i}_1^{\,*}(k)-\vec{i}_1(k)\right)+(R_1+j\omega_1 L_1)\vec{i}_1(k)+\vec{u}_c(k)
\end{aligned} \tag{4.27}$$

where integrators in the outer current control loop as well as a Smith predictor in the inner current control loop in order to compensate for the computational delay in the DSP are included. The integrator is given by

$$\sum\Delta\vec{i}_2(k+1)=\frac{T_s}{L_2/R_2}\left(\vec{i}_2^{\,*}(k)-\vec{i}_2(k)\right)+\sum\Delta\vec{i}_2(k) \tag{4.28}$$

whereas the Smith predictor algorithm is according to

$$\begin{aligned}
\vec{s}_p(k+1) &= \left(1-\frac{R_1T_s}{L_1}-j\omega_1T_s\right)\vec{s}_p(k)+\frac{T_s}{L_1}\vec{u}_1(k)\\
\vec{i}_{smith}(k+1) &= \left(\frac{R_1T_s}{L_1}+j\omega_1T_s\right)\vec{s}_p(k)-\frac{T_s}{L_1}\vec{u}_1(k)
\end{aligned} \tag{4.29}$$

The block diagram representation of the discrete line current controller is displayed in Figure 4.6. Note that the feed back of the converter voltage reference is bounded by the DC-link voltage, in order to fully utilise the properties of the Smith predictor. The resemblance to the battery current controller, displayed in Figure 4.2, is quite obvious. However, the robustness and the frequency domain characteristics are improved by keeping the intermediate capacitor voltage P-controller in the line current controller. This is especially important due to the active filter function of the battery charger.

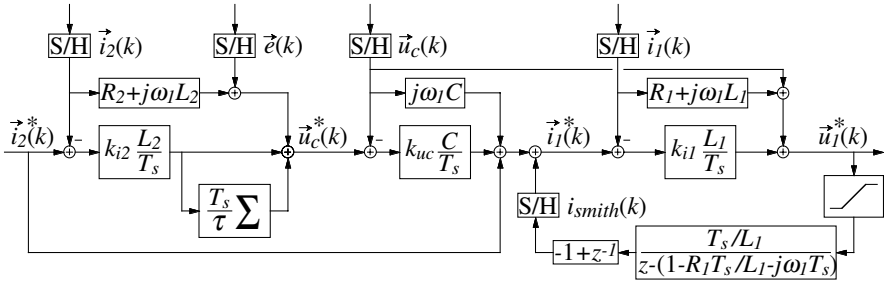

Figure 4.6 Block diagram representation of the discrete line current controller.

Analysis

Analysis of the line current controller is based on the closed loop system of the discrete controller and the line LCL-filter. The closed loop system is derived in the same way as the battery side counterpart was in the previous section. The complex valued discrete state space vector representation of the LCL-filter in synchronous coordinates is found from the continuous model (3.26) and is given by

$$\begin{aligned} x(k+1) &= \vec{\Phi}_{LCL}^{dq} x(k) + \vec{\Gamma}_{LCL}^{dq} u(k) \\ \vec{i}_2(k) &= \vec{C}_{LCL}^{dq} x(k) + \vec{D}_{LCL}^{dq} u(k) \end{aligned} \tag{4.30}$$

where the state vector x and input vector u are defined according to

$$x = \begin{bmatrix} \vec{i}_1 & \vec{u}_c & \vec{i}_2 \end{bmatrix}^T \tag{4.31}$$

$$u = \begin{bmatrix} \vec{u}_1 & \vec{e} \end{bmatrix}^T \tag{4.32}$$

The state matrix $\vec{\Phi}_{LCL}^{dq}$ and the input matrix $\vec{\Gamma}_{LCL}^{dq}$ are given by

$$\vec{\Phi}_{LCL}^{dq} = e^{\vec{A}_{LCL}^{dq} T_s} \tag{4.33}$$

$$\vec{\Gamma}_{LCL}^{dq} = \begin{bmatrix} \vec{\Gamma}_{LCL}^{u_1} & \vec{\Gamma}_{LCL}^{e} \end{bmatrix} = \int_0^{T_s} e^{\vec{A}_{LCL}^{dq} h} dh \cdot \vec{B}_{LCL}^{dq} \tag{4.34}$$

and finally, the output matrixes are given by

$$\vec{C}_{LCL}^{dq} = \begin{bmatrix} 0 & 0 & 1 \end{bmatrix} \tag{4.35}$$

$$\vec{D}_{LCL}^{dq} = \begin{bmatrix} 0 & 0 \end{bmatrix} \tag{4.36}$$

The extended state vector X and input vector U of the closed loop system are defined according to

$$X = \begin{bmatrix} \vec{i}_1 & \vec{u}_c & \vec{i}_2 & \vec{u}_1 & \vec{s}_p & \sum \Delta \vec{i}_2 \end{bmatrix}^T \tag{4.37}$$

$$U = \begin{bmatrix} \vec{e} & \vec{i}_2^{\,*} \end{bmatrix}^T \tag{4.38}$$

The cascade control algorithm can be interpreted as a state feed back controller with additional feed forward of the inputs according to

$$\vec{u}_1(k+1) = \vec{u}_1^{\,*}(k) = \begin{bmatrix} \vec{L}_x & \vec{L}_{u_1} & \vec{L}_{s_p} & \vec{L}_{\sum i_2} \end{bmatrix} X(k) + \begin{bmatrix} \vec{L}_e & \vec{L}_{i_2 *} \end{bmatrix} U(k) \tag{4.39}$$

where

$$\vec{L}_x = \begin{bmatrix} \vec{L}_{i_1} & \vec{L}_{u_c} & \vec{L}_{i_2} \end{bmatrix} \tag{4.40}$$

The entries are found from (4.27), (4.28), and (4.29) and are given by

$$\vec{L}_{i_1} = -k_{i1} \frac{L_1}{T_s} + R_1 + j\omega_1 L_1 \tag{4.41}$$

$$\vec{L}_{u_c} = 1 + k_{i1} \frac{L_1}{T_s} \left(-k_{uc} \frac{C}{T_s} + j\omega_1 C \right) \tag{4.42}$$

$$\vec{L}_{i_2} = k_{i1} \frac{L_1}{T_s} \cdot k_{uc} \frac{C}{T_s} \left(-k_{i2} \frac{L_2}{T_s} + R_2 + j\omega_1 L_2 \right) \tag{4.43}$$

$$\vec{L}_{u_1} = -\frac{T_s}{L_1} \cdot k_{i1} \frac{L_1}{T_s} = -k_{i1} \tag{4.44}$$

$$\vec{L}_{s_p} = \left(\frac{R_1 T_s}{L_1} + j\omega_1 T_s \right) \cdot k_{i1} \frac{L_1}{T_s} = k_{i1} \left(R_1 + j\omega_1 L_1 \right) \tag{4.45}$$

$$\vec{L}_{\sum i_2} = k_{i1} \frac{L_1}{T_s} \cdot k_{uc} \frac{C}{T_s} \tag{4.46}$$

$$\vec{L}_e = k_{i1} \frac{L_1}{T_s} \cdot k_{uc} \frac{C}{T_s} \tag{4.47}$$

$$\vec{L}_{i_2 *} = k_{i1} \frac{L_1}{T_s} \left(1 + k_{uc} \frac{C}{T_s} \cdot k_{i2} \frac{L_2}{T_s} \right) \tag{4.48}$$

The complex valued vector representation of the closed loop system in synchronous coordinates can now be expressed as

$$X(k+1) = \overbrace{\begin{bmatrix} \vec{\Phi}_{LCL}^{dq} & \vec{\Gamma}_{LCL}^{u_1} & 0 & 0 \\ \vec{L}_x & \vec{L}_{u_1} & \vec{L}_{s_p} & \vec{L}_{\Sigma i_2} \\ 0 & \vec{S}_{u_1} & \vec{S}_{s_p} & 0 \\ \vec{I}_x & 0 & 0 & I \end{bmatrix}}^{\vec{\Phi}_X^{dq}} X(k) + \overbrace{\begin{bmatrix} \vec{\Gamma}_{LCL}^{e} & 0 \\ \vec{L}_e & \vec{L}_{i_2*} \\ 0 & 0 \\ 0 & \vec{I}_{i_2*} \end{bmatrix}}^{\left[\vec{\Gamma}_e^{dq} \quad \vec{\Gamma}_{i_2*}^{dq}\right]} U(k) \tag{4.49}$$

$$\vec{i}_2(k) = \underbrace{\begin{bmatrix} \vec{C}_{LCL}^{dq} & 0 & 0 & 0 \end{bmatrix}}_{\vec{C}_X^{dq}} X(k) + \underbrace{\begin{bmatrix} 0 & 0 \end{bmatrix}}_{\left[\vec{D}_e^{dq} \; \vec{D}_{i_2*}^{dq}\right]} U(k)$$

where the additional non-zero elements are given by

$$\vec{S}_{u_1} = \frac{T_s}{L_1} \tag{4.50}$$

$$\vec{S}_{s_p} = 1 - \frac{R_1 T_s}{L_1} - j\omega_1 T_s \tag{4.51}$$

$$\vec{I}_x = \begin{bmatrix} 0 & 0 & -k_{i2} \dfrac{L_2}{T_s} \cdot \dfrac{T_s}{L_2 / R_2} \end{bmatrix} \tag{4.52}$$

$$\vec{I}_{i_2*} = k_{i2} \frac{L_2}{T_s} \cdot \frac{T_s}{L_2 / R_2} \tag{4.53}$$

The complex valued vector representation of the closed loop system (4.49) is easily transformed into a real valued state space description, by separation of the complex valued relationships into their real and imaginary parts, i.e. the *d*- and *q*-components.

The gain constants k_{i1}, k_{uc} and k_{i2} are selected on basis of stability and frequency domain characteristics. The selected gain constants are

$$\begin{aligned} k_{i1} &= 0.5 \\ k_{uc} &= 0.25 \\ k_{i2} &= 1 \end{aligned} \tag{4.54}$$

Stability of the system with gain constants according to (4.54) is confirmed by the pole plot shown in Figure 4.7. The closed loop poles

corresponding to the selected gain constants are shown with large × markers. In the figure, the root locus of the closed loop system when only one gain constant at the time is altered while the others are fixed is also shown.

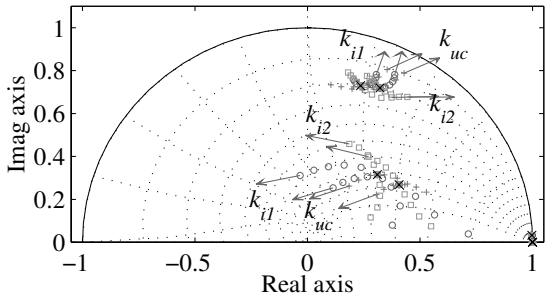

Figure 4.7 Root locus plot for the closed loop system. Selected gain constants (×), varying k_{i1} (○), k_{uc} (+) and k_{i2} (□).

Since the closed loop system is represented in vector notation, it can be regarded as a single input-single output (SISO) system. Therefore, ordinary gain and phase deviation functions derived from the frequency response are valid. The vector notation further implies that positive as well as negative frequencies have to considered. The sign of the frequency corresponds to the rotation direction of the vector, refer to the discussion in Section 2.2 on representation of positive- and negative-sequences in vector notation. Figure 4.8 shows the frequency response for the closed loop system.

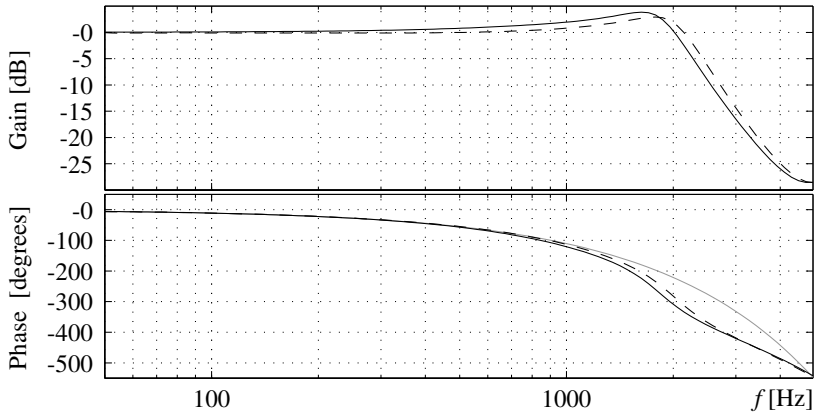

Figure 4.8 Frequency response from line current reference to line current, positive-sequence (solid) and negative-sequence (dashed).

Note the phase deviation of the frequency response shown in Figure 4.8. The phase deviation corresponds approximately to a linear phase lag of three samples, which is indicated by the grey line in the figure. The effect of the phase deviation will further be discussed in Chapter 5.

If the real valued vector representation, i.e. individual representation of the *d*- and *q*-components, is used, the closed loop system is regarded as a multiple input-multiple output (MIMO) system. In this case, other frequency domain analysis methods have to be applied [26]. In [11], frequency domain analysis based on the minimum and maximum singular values is described. It is stated that the gain spread is bounded by the minimum and maximum singular values. The gain may vary between the boundary values for a specific frequency depending on the direction of the input vector. In fact, it was found in [11] that the complex valued transfer functions for the positive- and negative-sequences correspond to these minimum and maximum singular values.

Simulation

A simulation of the line side currents of the battery charger, when applied to step changes in the *d*- and *q*-current references, is shown in Figure 4.9. The overshoot of the step responses in the outer current i_2 of about 30 % is due to the high bandwidth selected for the line current controller. The high bandwidth in combination with the third order LCL-filter imply an oscillatory behaviour, which is derived from the peaks in the frequency responses shown in Figure 4.8. However, due to the active filter option of the battery charger, the high bandwidth is deemed necessary in order to obtain high filtering performance.

The cross-coupling of the *d*- and *q*-currents is clearly seen in the simulation. That is, the oscillations in the *d*- and *q*-currents caused by step responses in the opposite current component. However, the steady state influence of the cross-coupling is compensated for by the line current controller. The slower response in the *q*-current for a positive step change is due to overmodulation of the VSC.

In Figure 4.10, a simulation with the averaged model of the VSC is shown. The dynamic resemblance of the current responses obtained by the averaged model compared to the instantaneous model is high. Their difference is merely due to the high frequency current ripple, especially in the inner inductor current i_1, caused by the switched operation of the VSC for the instantaneous model. Hence, the validity of the averaged model is confirmed. Furthermore, the time consumption for the

simulation of the averaged model is decreased by at least one order of magnitude compared to the instantaneous model.

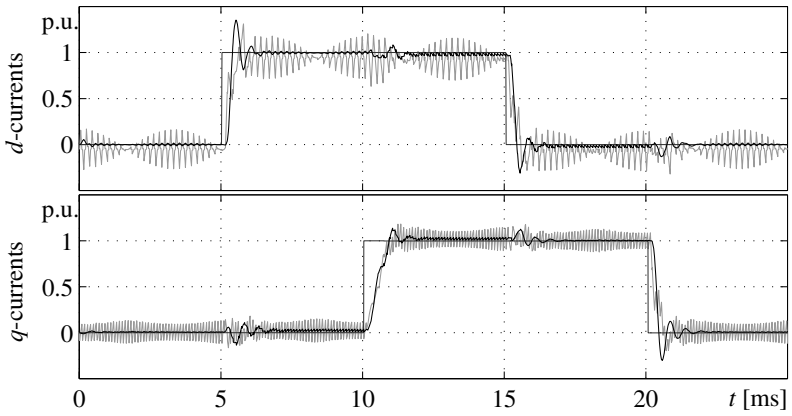

Figure 4.9 Line side *d*- and *q*-currents, i_2^* (dark grey), i_2 (black), and i_1 (light grey).

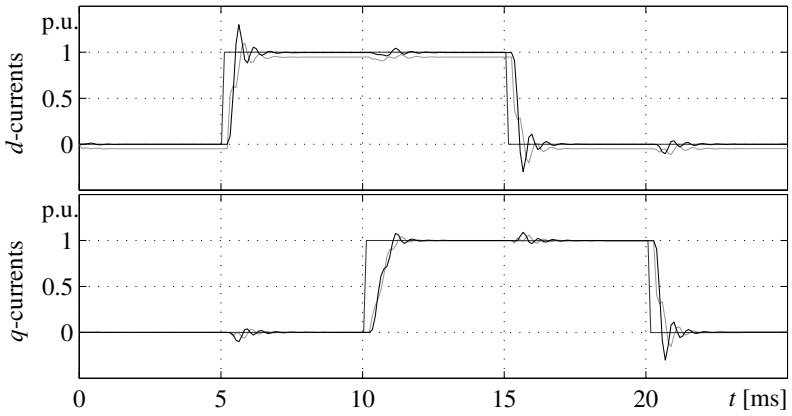

Figure 4.10 Line side *d*- and *q*-currents obtained by simulation of the averaged model, i_2^* (dark grey), i_2 (black), and i_1 (light grey).

4.4 DC-link voltage control

The purpose of the DC-link voltage controller is to preserve the DC-link voltage at its reference value. This is accomplished by balancing the active power flow in the battery charger. That is, the active current component i_{2q} on the line side is controlled in order to match the power consumed by the battery charger. The consumed power, in this case, corresponds to the charging (output) power and the power dissipated in the battery charger.

The block diagram representation of the DC-link voltage control loop is shown in Figure 4.11. The DC-link voltage controller consists of a PI-controller, where the integral part reduces the steady state error of the DC-link voltage. The low pass filter introduced in the feed back loop limits the bandwidth of the DC-link voltage controller. Hence, generation of counter actions due to the DC-link voltage variation caused by the active filter currents are avoided. Furthermore, the low bandwidth is circumvented by the feed forward of the battery current. This implies a faster response to changes in the battery current and thereby reduction of the DC-link voltage deviation during transients.

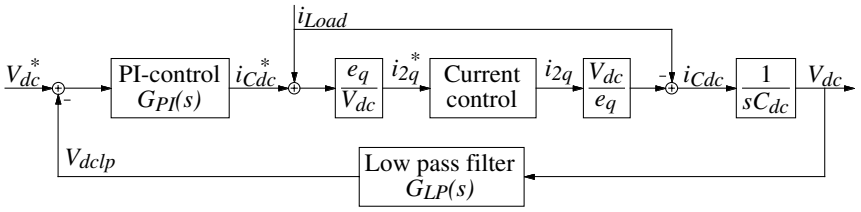

Figure 4.11 Block diagram representation of the DC link voltage controller.

The low pass filter further implies that the dynamics of the line current controller can be neglected in the DC-link voltage controller synthesis. From Figure 4.11, the closed loop transfer function of the DC-link voltage controller is obtained according to

$$G_{PIc}(s) = \frac{\frac{1}{sC_{dc}} G_{PI}(s)}{1 + \frac{1}{sC_{dc}} G_{PI}(s) G_{LP}(s)} \tag{4.55}$$

The transfer function of the PI-controller is given by

$$G_{PI}(s) = K(1 + \frac{1}{sT_i}) \tag{4.56}$$

where the parameters K and T_i are the gain and integral time constant of the PI-controller, respectively.

The low pass filter consists of a first order filter with the cut off frequency selected to f_{lp}=30 Hz. Hence, the transfer function of the low pass filter is given by

$$G_{LP}(s) = \frac{\omega_{lp}}{s + \omega_{lp}} \tag{4.57}$$

The closed loop transfer function of the DC-link voltage controller can then be written

$$G_{PIc}(s) = \frac{\frac{K}{C_{dc}T_i}(sT_i + 1)(s + \omega_{lp})}{s^3 + s^2\omega_{lp} + s\frac{K\omega_{lp}}{C_{dc}} + \frac{K\omega_{lp}}{C_{dc}T_i}} \tag{4.58}$$

where the denominator of (4.58) corresponds to the characteristic polynomial of the closed loop system.

Since the characteristic polynomial of the closed loop system is known, and thereby also the characteristic equation, the parameters of the PI-controller can be determined by pole placement. The poles of the closed loop system are selected as a triple pole, in order to avoid oscillations in the DC-link voltage and also prevent from a large voltage overshoot at system start up. The characteristic polynomial of a triple pole system is given by

$$(s + x)^3 = s^3 + 3s^2x + 3sx^2 + x^3 \tag{4.59}$$

where x corresponds to the location of the poles on the negative real axis in the s-plane, i.e. the angular frequency of the closed loop system. By identification of the coefficients of the characteristic polynomial given by the denominator of (4.58) with the desired characteristic polynomial in (4.59), the following equation system with the corresponding solutions are obtained

$$\begin{cases} 3x = \omega_{lp} \\ 3x^2 = \frac{K\omega_{lp}}{C_{dc}} \\ x^3 = \frac{K\omega_{lp}}{C_{dc}T_i} \end{cases} \Rightarrow \begin{cases} x = \frac{\omega_{lp}}{3} \\ K = \frac{C_{dc}\omega_{lp}}{3} \\ T_i = \frac{3^2}{\omega_{lp}} \end{cases} \tag{4.60}$$

From (4.60), it can be concluded that the triple pole placement strategy gives a bandwidth of the closed loop system which is one third of the low pass filter bandwidth.

Simulation

The performance of the DC-link voltage controller is verified by simulations, where the averaged converter models are used. The simulated DC-link voltage response at system start up is shown in Figure 4.12. In the figure, the effect of the feed forward of the battery (load) current during a step change is also shown. The feed forward term almost eliminates the DC-link voltage dip during the battery current transient.

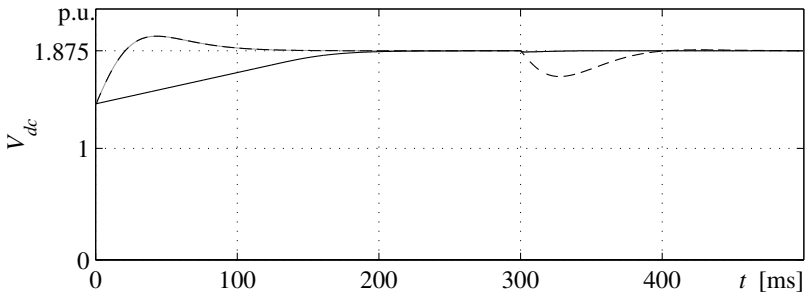

Figure 4.12 Simulation of the DC-link voltage, in per unit, at system start up and a step change in the battery current corresponding to rated power at t=300 ms. PI-controller with feed forward of battery current (grey) and without (black dashed), and PI-controller with feed forward and anti reset windup (black).

The overshoot in the DC-link voltage at system start up is approximately 30 %. The overshoot is due to the zero provided by the integrator in the numerator of the transfer function (4.58), i.e. the zero located at $1/T_i$ on the negative real axis in the s-plane. However, by limiting the output of the DC-link voltage PI-controller, the overshoot at system start up is reduced at the expense of a prolonged start up time. This limitation also reduces the resulting line currents during start up, hence smoother start up of the system is achieved.

Furthermore, in order to avoid windup of the integrator, an anti reset windup algorithm [37] is employed. The anti reset windup algorithm resets the integrator to an appropriate value, if the output of the PI-controller exceeds the limitation. Hence, the value of the integrator is reset so that the output of the PI-controller is within the boundary. In Figure 4.12, the result of the PI-controller output limitation and the anti reset windup strategy is shown. Here, the output of the PI-controller is limited within 20 % of the corresponding nominal line current.

5

Active filter control

In this chapter specific properties concerning shunt active filter control are discussed. The operation principle of a shunt AF for grid conditioning purposes, such as reactive power compensation, harmonic filtering and load balancing, is generally discussed in Chapter 2. It is stated that the basic operation principle of a shunt AF is to inject the undesired components of the load current, in order to cancel their presence in the line current. This is illustrated in Figure 5.1. It is clear that the performance of the shunt AF is determined by the amount of reduction of these undesired components in the line current.

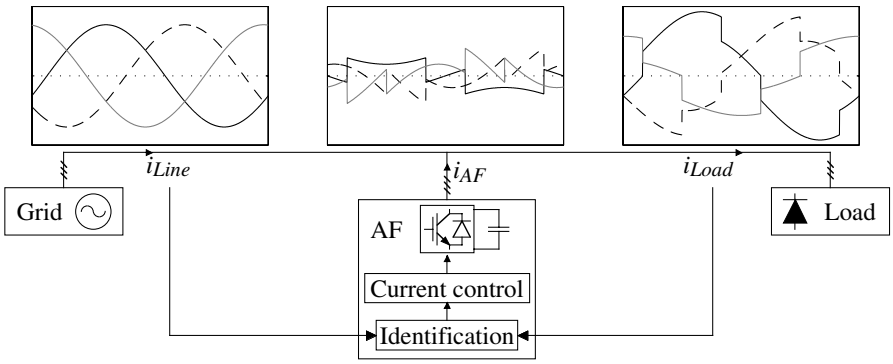

Figure 5.1 Shunt active filter operating principle.

The function of a shunt AF can be divided into two parts. First, the currents that should be compensated for have to be identified or detected. This can be performed either in the frequency domain or in the time domain. Furthermore, the detection can be based either on the load current, the supply (line) current, or the grid voltage [3]. Detection based on the load current, which is used here, is suitable for a shunt AF installed in the vicinity of the load to be conditioned.

The second part consists of the active filter current controller, which should ensure good agreement between the injected currents and the undesired components of the load current. Basically, the filtering

performance of a shunt AF is determined by the current control part, at least in steady state operation. However, during transient operation the filtering performance is also affected by the identification part.

5.1 Identification based on the load current

Various methods for identification of the undesired load current components are proposed in the literature. In this thesis, however, only three methods are considered.

Fast fourier transform

The fast fourier transform (FFT) method calculates the magnitude and phase of the load current frequency components [24]. Then the component corresponding to the fundamental active current is removed. Finally, the active filter current reference is obtained from the inverse FFT of the remaining frequency components. The advantage of the FFT method is that the magnitudes of the frequency components are known. Hence by manipulation of the magnitudes, overloading of the shunt AF can be prevented. Furthermore, selective conditioning is made possible which is useful in some applications, where the focus is to reduce some specific component of the load current. However, the calculations involved are cumbersome and also the lack of information regarding the sequences, i.e. positive- or negative-sequences, of the conditioning components makes the FFT method less practicable.

Instantaneous reactive power theory

The instantaneous reactive power theory (IRPT) proposed in [1][2] is a wide spread concept for load current identification in active filter applications. The idea is to derive the compensating current references based on the decomposition of the instantaneous active and reactive power into their DC and AC components, respectively. The fundamental active and reactive currents are then given by the DC component of the instantaneous power. Consequently, the AC component corresponds to the negative-sequence current component as well as the current harmonics.

According to the IRPT, the corresponding vector representation of the instantaneous power $\vec{p}$ in the stationary reference $\alpha\beta$-frame is defined as

$$\vec{p} = \vec{e}^{\,\alpha\beta *} \cdot \vec{i}^{\,\alpha\beta} = p + jq \tag{5.1}$$

where p and q denotes the instantaneous active and reactive power, respectively. Note, the difference from the normal definition of

instantaneous power given in Appendix A.3, where the conjugation is applied on the current vector and not the voltage vector as in (5.1).

In order to illustrate the IRPT, consider the case of a load current vector $\vec{i}_{Load}^{\,\alpha\beta}$ and an ideal grid voltage vector $\vec{e}^{\,\alpha\beta}$ given by

$$\begin{cases} \vec{e}^{\,\alpha\beta} = E_1 e^{j\omega_1 t} \\ \vec{i}_{Load}^{\,\alpha\beta} = I_1 e^{j(\omega_1 t - \phi_1)} + I_{-1} e^{-j\omega_1 t} + I_{-5} e^{-j5\omega_1 t} + I_7 e^{j7\omega_1 t} \end{cases} \tag{5.2}$$

Then the instantaneous power vector is obtained by inserting (5.2) into (5.1), which gives

$$\vec{p} = E_1 I_1 e^{-j\phi_1} + E_1 \left(I_{-1} e^{-j2\omega_1 t} + I_{-5} e^{-j6\omega_1 t} + I_7 e^{j6\omega_1 t} \right) \tag{5.3}$$

The DC component of the instantaneous power in (5.3) is divided into its corresponding active and reactive component according to

$$\vec{p}_{DC} = p_{DC} + jq_{DC} = E_1 I_1 e^{-j\phi_1} = E_1 I_1 \cdot (\cos\phi_1 - j\sin\phi_1) \tag{5.4}$$

The AC component of the instantaneous power is given by

$$\vec{p}_{AC} = E_1 \left(I_{-1} e^{-j2\omega_1 t} + I_{-5} e^{-j6\omega_1 t} + I_7 e^{j6\omega_1 t} \right) \tag{5.5}$$

Since the compensating current should correspond to the instantaneous power given by all AC components and the reactive DC component, i.e.

$$\vec{p}_{Comp} = jq_{DC} + \vec{p}_{AC} \tag{5.6}$$

the compensating current is determined by the inverse relationship of (5.1), that is

$$\vec{i}_{Comp}^{\,\alpha\beta} = \frac{\vec{p}_{Comp}}{\vec{e}^{\,\alpha\beta *}} \tag{5.7}$$

which in this case corresponds to

$$\vec{i}_{Comp}^{\,\alpha\beta} = I_1 \sin\phi_1 e^{j(\omega_1 t - \frac{\pi}{2})} + I_{-1} e^{-j\omega_1 t} + I_{-5} e^{-j5\omega_1 t} + I_7 e^{j7\omega_1 t} \tag{5.8}$$

The compensating current in (5.8) contains all the undesired components of the load current in this case. Hence, these components are cancelled from the line current, which then only consists of the current component corresponding to the fundamental active power, i.e.

$$\vec{i}_{Line}^{\alpha\beta} = I_1 \cos\phi_1 e^{j\omega_1 t} \tag{5.9}$$

As a conclusion, the IRPT enables full identification and decomposition of the compensation currents that should be injected by the shunt AF. Furthermore, this is achieved without cumbersome calculations, which is the main reason for the wide spread use of the method.

Instantaneous currents in synchronous coordinates

Another approach for identifying the undesired components of the load current considers the instantaneous currents represented in the synchronously rotating reference *dq*-frame oriented to the integral of the grid voltage vector [4][5]. This method resembles the IRPT method and under ideal conditions they are equivalent, which will be shown later. Furthermore, the use of synchronous coordinates is convenient, since the line side current controller of the battery charger, described in Section 4.3, already utilises the synchronous reference *dq*-frame.

As described in Appendix A.2, the load current vector in the synchronous reference *dq*-frame is derived from the stationary reference $\alpha\beta$-frame by subtraction of the corresponding angle difference θ according to

$$\vec{i}_{Load}^{dq} = \vec{i}_{Load}^{\alpha\beta} \cdot e^{-j\theta} \tag{5.10}$$

Consider the case investigated previously for the IRPT, where the grid voltage vector and load current vector are given by (5.2). The angle θ used in the vector transformation is given by the argument of the grid voltage integral, that is

$$\theta = \omega_1 t - \frac{\pi}{2} \tag{5.11}$$

The representation of the load current vector of (5.2) in synchronous coordinates is then given by

$$\vec{i}_{Load}^{dq} = \left(I_1 e^{-j\phi_1} + I_{-1} e^{-j2\omega_1 t} + I_{-5} e^{-j6\omega_1 t} + I_7 e^{j6\omega_1 t} \right) \cdot e^{j\frac{\pi}{2}} \tag{5.12}$$

The DC component of the load current vector in synchronous coordinates is written

$$\vec{i}_{Load,DC}^{dq} = I_1 \cdot \left(\sin\phi_1 + j\cos\phi_1 \right) \tag{5.13}$$

where the real and imaginary parts correspond to the reactive and active current components, respectively. The AC component of the load current vector corresponds to the negative-sequence current component and the current harmonics, that is

$$\vec{i}_{Load,AC}^{\,dq} = j \cdot \left(I_{-1} e^{-j2\omega_1 t} + I_{-5} e^{-j6\omega_1 t} + I_7 e^{j6\omega_1 t} \right) \tag{5.14}$$

As in the case of the IRPT, the instantaneous currents represented in synchronous coordinates provide complete information of the different load current components. The compensation current should correspond to the fundamental reactive current, i.e. the real part of the DC component, and the AC component

$$\vec{i}_{Comp}^{\,dq} = \Re\mathrm{e}\left(\vec{i}_{Load,DC}^{\,dq} \right) + \vec{i}_{Load,AC}^{\,dq} \tag{5.15}$$

which is equivalent to the compensation current obtained from the IRPT.

The result of load current decomposition by the IRPT and by the representation of the instantaneous currents in synchronous coordinates are equivalent under ideal conditions [4]. However, in the presence of grid voltage distorsion, the obtained compensation currents differ. The distorted voltage implies that the corresponding current harmonics will contribute to the actual power flow, and hence to the DC component of the instantaneous power.

According to the IRPT, this contribution implies that part of the load current harmonics can not be separated from the fundamental current component, and hence can not be detected. However, for the instantaneous currents represented in the synchronous reference *dq*-frame, the effect of the voltage harmonics is reduced. This is due to the integration of the grid voltage vector involved in order to obtain the transformation angle. This means that even if the current harmonics contribute to the actual power flow, they are still represented by the AC component of the load current vector.

From the discussion given above, identification by the instantaneous currents represented in the synchronously rotating reference *dq*-frame is selected. The choice is motivated by the equivalency to the IRPT method, together with the convenient relationship with the line current controller. Table 5.1 gives the correspondence between the conditioning components and their representation in the synchronous reference *dq*-frame.

Table 5.1 Representation of the current components in the synchronously rotating reference *dq*-frame.

Component	Sequence	Frequency	Vector
active	positive	*DC*	ji_q
reactive	pos.	*DC*	i_d
asymmetry	negative	$2f_1$	$I_{-1}e^{-j2\omega_1 t}$
5th harmonic	neg.	$6f_1$	$I_{-5}e^{-j6\omega_1 t}$
7th harmonic	pos.	$6f_1$	$I_7 e^{j6\omega_1 t}$
11th harmonic	neg.	$12f_1$	$I_{-11}e^{-j12\omega_1 t}$
13th harmonic	pos.	$12f_1$	$I_{13}e^{j12\omega_1 t}$
…	…	…	…

Filters

In order to extract and remove the current component corresponding to the fundamental active power, a high pass filter on the *q*-axis current component of the load current vector is sufficient. However, in order to obtain selective conditioning by the battery charger, filters extracting the respective conditioning components from the load current are applied instead. This is illustrated in Figure 5.2, where a low pass filter on the *d*-axis current and a band pass filter at twice the fundamental frequency provides for the fundamental reactive current component and the negative-sequence component, respectively. A high pass filter extracts the corresponding load current harmonics, which indicates that there is no selectivity in the harmonic filtering capability, i.e. either all or no current harmonics are filtered. This is not regarded as a severe restriction of the shunt AF performance, but the needed calculation effort is greatly reduced.

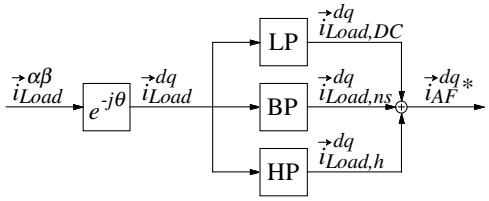

Figure 5.2 Principle block diagram of the load current identifier. Note that the low pass filter only provides the *d*-axis DC current component.

The low pass filter consists of a 4th order Butterworth filter, with cut off frequency f_{lp} equal to 30 Hz. This is a trade off between high attenuation of the current harmonics and the negative-sequence current component

versus the transient characteristics, i.e. response time and overshoot, of the filter. The corresponding transfer function of the low pass filter is given by

$$G_{LP}(s) = \frac{\omega_{lp}^4}{s^4 + 2.613\omega_{lp}s^3 + 3.414\omega_{lp}^2 s^2 + 2.613\omega_{lp}^3 s + \omega_{lp}^4} \quad (5.16)$$

A first approach for designing the band pass filter is to combine a low pass and a high pass filter. However, the band pass filter in fact consists of two identical band pass filters applied to the *d*- and *q*-axis components of the load current, respectively. Hence, the calculation effort would be high. Another approach [33] utilises the vector representation of the load current and applies a vector transformation into a negative-sequence oriented reference frame, referred to as the *ns*-frame. This implies that the fundamental negative-sequence current component is represented as a DC quantity. Consequently, low pass filters are sufficient in order to extract the negative-sequence component from the load current. The output from the low pass filters are then transformed back into the synchronous reference *dq*-frame. The result of the back transformation corresponds to a frequency shift of the low pass filter. The transfer function of the band pass filter is obtained according to [11] in complex notation as

$$G_{BP}^{dq}(s) = G_{LP}^{ns}(s + j2\omega_1) \quad (5.17)$$

where the low pass filter consists of a 4th order Butterworth filter, refer to (5.16), with cut off frequency equal to 20 Hz. The frequency response of the complex valued band pass filter is shown in Figure 5.3.

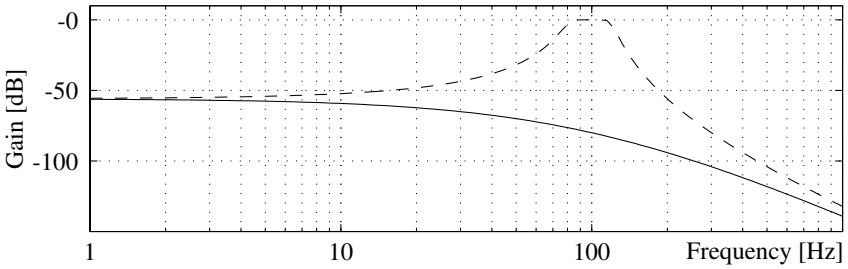

Figure 5.3 Frequency response of the band pass filter in the synchronous reference *dq*-frame, positive- (solid) and negative-sequence (dashed).

As can be concluded from the figure, it is only the negative-sequence current component of twice the fundamental frequency that passes the filter, which is the intention of the band pass filter.

For the high pass filter, a similar approach is used. In this case, first order high pass filters are employed in both the reference frames corresponding to the positive- and negative-sequences of the fundamental frequency. The complex valued transfer function of the high pass filter is

$$G_{HP}^{dq}(s) = G_{HP}^{ns}(s + j2\omega_1) \cdot G_{HP}^{dq}(s) = \frac{s + j2\omega_1}{s + j2\omega_1 + \omega_{hp}} \cdot \frac{s}{s + \omega_{hp}} \qquad (5.18)$$

where the cut off frequency f_{hp} is chosen to 10 Hz. The relatively low cut off frequency of the high pass filters ensures high phase agreement for the filtered current harmonics. The frequency response of the high pass filter is shown in Figure 5.4. The result is, in some aspect, equivalent to notch filters at the fundamental frequency in the stationary reference $\alpha\beta$-frame.

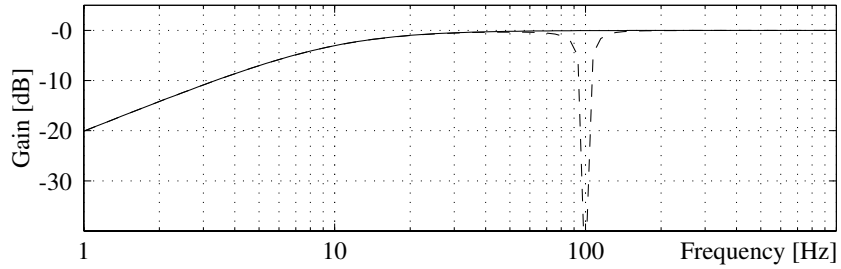

Figure 5.4 Frequency response of the high pass filter in the synchronous reference *dq*-frame, positive- (solid) and negative-sequence (dashed).

In Figure 5.5, the complete block diagram representation of the load current identifier is shown.

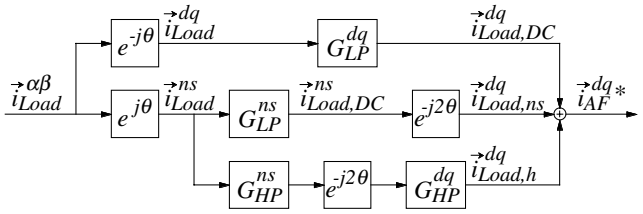

Figure 5.5 Block diagram of the load current identifier.

Transient responses of the filters

From the discussion given above, it can be concluded that the steady state performance of the filters, applied in the load current identifier, is good. This indicates that the steady state performance of the shunt AF is determined by the current controller. However as mentioned previously, the transient performance of the shunt AF is affected by the identification

filters. This is illustrated in Figure 5.6, where the filtered outputs are shown when step changes in each of the conditioning current components are applied.

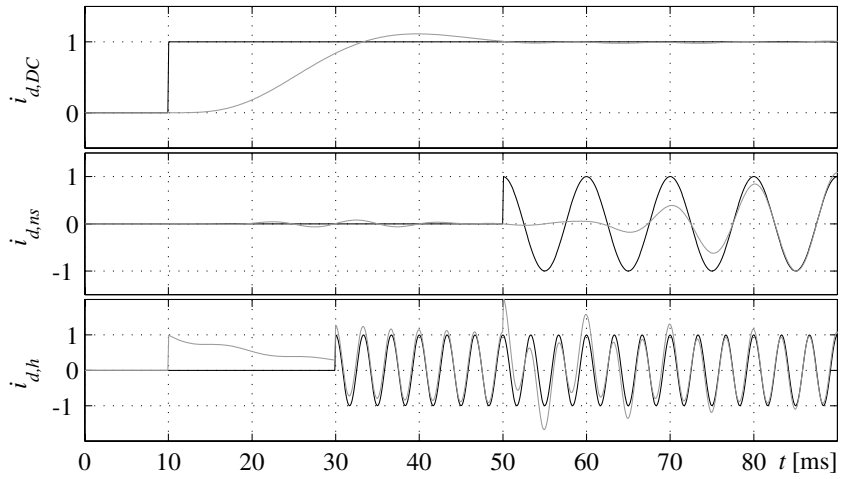

Figure 5.6 Ideal (black) and filtered outputs (grey) during step responses in the individual *d*-axis components of the load current at 10 ms, 30 ms and 50 ms for the reactive, harmonic and negative-sequence current components, respectively. Note the coupling between the filtered outputs, especially for the high pass filter output.

From Figure 5.6, it is concluded that the response times for the low pass and band pass filters roughly correspond to two fundamental time periods, i.e. 40 ms. This is due to the low cut off frequencies selected for the low pass filters used. The low cut off frequencies further provide high reduction of the other frequency components, which implies low interference between the filtered outputs.

The high pass filter output, on the contrary, is strongly affected by step changes in either the fundamental current or the negative-sequence current component. This is due to the low cut off frequency of the high pass filter, selected in order to obtain good phase agreement of the harmonic current reference. Initially, all frequency components passes the high pass filter, which implies that the harmonic current reference can be dangerously large. Furthermore, the transient bias in the high pass filter output can cause unintended active or reactive power flow in the shunt AF.

5.2 Original active filter controller

The original and first approach to the active filter controller is obtained by combining the identification filters with the line side current controller derived in Section 4.3. In Figure 5.7, the block diagram representation of this original active filter controller is shown.

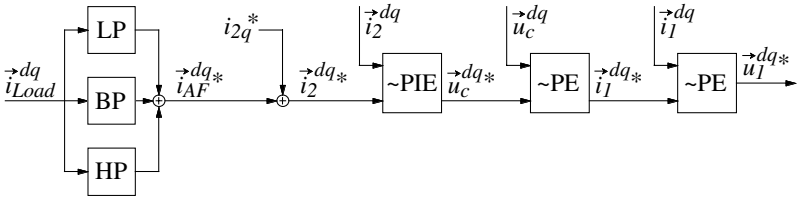

Figure 5.7 Block diagram representation of the original active filter controller.

Note that the fundamental active current reference i_{2q}^{*} obtained from the DC-link voltage controller is added to the active filter current reference. Also note the shorter notation applied to the P-controllers (P), with feed back of the *d*- and *q*-axis cross-coupling (~) and the additional feed forward (E).

In this section, the performance of a shunt AF employing the original active filter controller is investigated for one conditioning capability at the time. The same results are obtained when all conditioning capabilities are analysed simultaneously. However, the analysis is simplified since the results may be hidden under other phenomena, when performing simultaneous investigation of the conditioning capabilities.

Reactive power compensation

Reactive power compensation is in many aspects the easiest active filter task to be performed. Since the synchronously rotating reference *dq*-frame is employed for the original active filter controller, reactive power compensation is equivalent to controlling the *d*-axis DC current component. Furthermore, since the active filter controller contains integrators in the outer current control loop, complete reduction of the reactive current component is obtained.

The simulated result, when performing reactive power compensation with the original active filter controller, is shown in Figure 5.8. In this case the load consists of purely inductive elements, which implies that the load current is completely reactive and lags the grid voltage by 90 degrees.

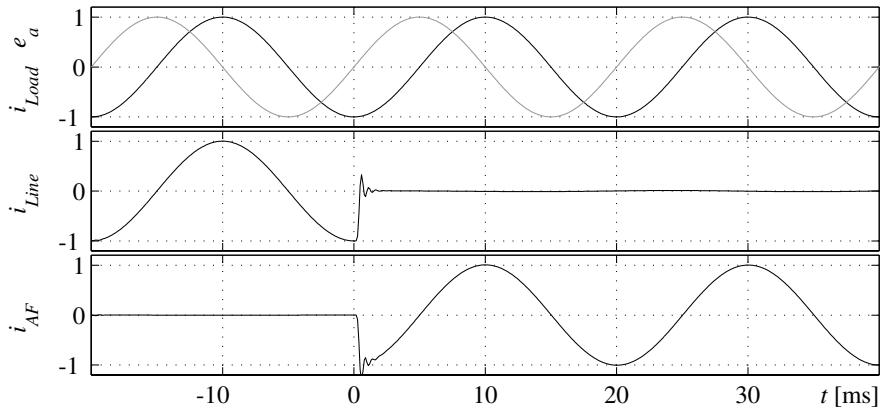

Figure 5.8 Simulated phase currents when performing reactive power compensation of inductive load. Top) load current (black) and grid voltage (grey), middle) resulting line current, and bottom) injected AF current.

The remaining component of the line current corresponds to the fundamental active current consumed by the active filter itself. This small active current component is needed in order to maintain the DC-link voltage at its nominal value, thus compensating for the losses in the shunt AF.

Load balancing

The simulated result when performing load balancing, with the original active filter controller, is shown in Figure 5.9. In this case, the load consists of a resistive load connected between the phases *a* and *c*. Hence, the load current consists of equal amount of the positive- and the negative-sequence current components of fundamental frequency. The two phase load is considered appropriate, since the load balancing capability is restricted to the negative-sequence component due to the lack of a neutral conductor in the shunt AF, i.e. the battery charger.

Under ideal conditions the resulting line current should only contain the fundamental positive-sequence current component, since that component corresponds to the average power consumed by the load. However, as can be seen in Figure 5.9, the line currents are not totally balanced in this case, despite the injection of the negative-sequence current component by the shunt AF. This implies that the injected current is not equal to the corresponding negative-sequence current component of the two phase load.

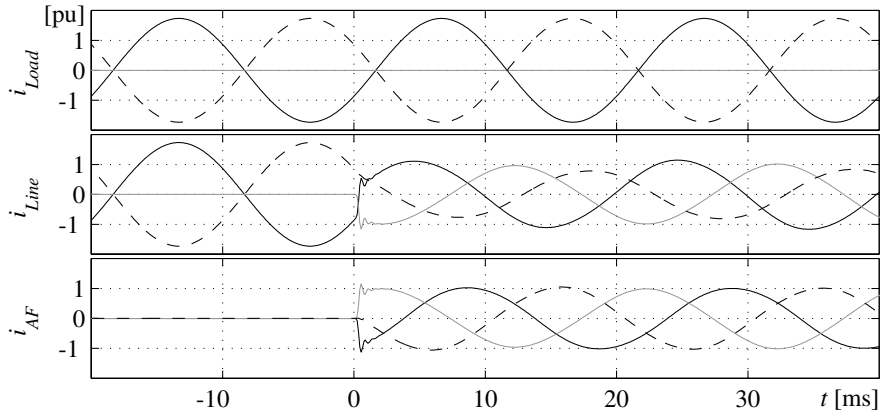

Figure 5.9 Simulated phase currents (phase *a* black, phase *b* grey, and phase *c* dashed black) when performing load balancing of a resistive two phase load. Top) load currents, middle) line currents, and bottom) injected AF currents.

The difference between the load current and the injected current is due to the phase deviation of the line side current controller, see Figure 4.8 on page 55. The phase deviation implies that the injected current differ in phase from the load current. Hence, complete cancellation of the negative-sequence current component is not accomplished. Nevertheless, the performance can be improved by compensating for this inherent phase deviation. This is further discussed in the next section.

Harmonic filtering

Since harmonic filtering involves the injection of several high frequency current components corresponding to the current harmonics produced by the load, it is considered from a control point of view as the hardest task to perform. In order to analyse the harmonic filtering property of the original active filter controller, the complete model of the high pass filter and the current controller has to be derived. From (5.18), the complex valued discrete state space representation of the high pass filter can be derived and is generally written according to

$$\begin{aligned} x_{hp}(k+1) &= \vec{A}_{hp} x_{hp}(k) + \vec{B}_{hp} \vec{i}_{Load}^{\,dq}(k) \\ \vec{i}_{AF}^{\,dq*}(k) &= \vec{C}_{hp} x_{hp}(k) + \vec{D}_{hp} \vec{i}_{Load}^{\,dq}(k) \end{aligned} \tag{5.19}$$

where x_{hp} is the state vector of the high pass filter. The complete model is obtained by the series connection of the state space systems (5.19) and (4.49), which gives

$$\begin{bmatrix} X(k+1) \\ x_{hp}(k+1) \end{bmatrix} = \begin{bmatrix} \vec{\Phi}_X^{dq} & \vec{\Gamma}_{i_2*}^{dq}\vec{C}_{hp} \\ 0 & \vec{A}_{hp} \end{bmatrix} \begin{bmatrix} X(k) \\ x_{hp}(k) \end{bmatrix} + \begin{bmatrix} \vec{\Gamma}_e^{dq} & \vec{\Gamma}_{i_2*}^{dq}\vec{D}_{hp} \\ 0 & \vec{B}_{hp} \end{bmatrix} \begin{bmatrix} \vec{e}^{dq}(k) \\ \vec{i}_{Load}^{dq}(k) \end{bmatrix}$$

$$\vec{i}_2^{dq}(k) = \underbrace{\begin{bmatrix} \vec{C}_X^{dq} & \vec{D}_{i_2*}^{dq}\vec{C}_{hp} \end{bmatrix}}_{\begin{bmatrix} \vec{C}_X^{dq} & 0 \end{bmatrix}} \begin{bmatrix} X(k) \\ x_{hp}(k) \end{bmatrix} + \underbrace{\begin{bmatrix} \vec{D}_e^{dq} & \vec{D}_{i_2*}^{dq}\vec{D}_{hp} \end{bmatrix}}_{[0 \;\; 0]} \begin{bmatrix} \vec{e}^{dq}(k) \\ \vec{i}_{Load}^{dq}(k) \end{bmatrix} \tag{5.20}$$

Neglecting the influence of the grid voltage in the analysis, the closed loop system of the original active filter controller is written

$$\begin{bmatrix} X(k+1) \\ x_{hp}(k+1) \end{bmatrix} = \begin{bmatrix} \vec{\Phi}_X^{dq} & \vec{\Gamma}_{i_2*}^{dq}\vec{C}_{hp} \\ 0 & \vec{A}_{hp} \end{bmatrix} \begin{bmatrix} X(k) \\ x_{hp}(k) \end{bmatrix} + \begin{bmatrix} \vec{\Gamma}_{i_2*}^{dq}\vec{D}_{hp} \\ \vec{B}_{hp} \end{bmatrix} \vec{i}_{Load}^{dq}(k)$$

$$\vec{i}_{Line}^{dq}(k) = \begin{bmatrix} -\vec{C}_X^{dq} & 0 \end{bmatrix} \begin{bmatrix} X(k) \\ x_{hp}(k) \end{bmatrix} + \vec{i}_{Load}^{dq}(k) \tag{5.21}$$

Basically, both the bandwidth and the phase deviation of the current controller affects the harmonic filtering performance. The bandwidth of the current controller, refer to the frequency response plot in Figure 4.8, is sufficiently high. The phase deviation, on the other hand, has a more deteriorating effect on the filtering performance. The phase delay, corresponding to three samples, decreases the harmonic filtering performance. This is concluded from the closed loop frequency response displayed in Figure 5.10 for the shunt AF investigated, i.e. the frequency response from the load current to the resulting line current according to (5.21).

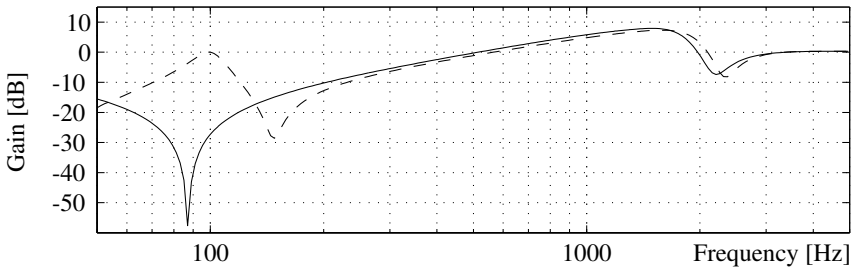

Figure 5.10 Closed loop frequency response for the original harmonic filter controller in the synchronous reference *dq*-frame, positive-sequence (solid) and negative-sequence (dashed).

Note that the low frequency behaviour is due to the high pass filter used in the current harmonic identification and not caused by the current

controller. Anyway, the poor filtering performance of the original active filter controller is clearly seen. In fact, as can be seen in Figure 5.10, the higher order load current harmonics, i.e. above the 12th harmonic in synchronous coordinates, are even amplified instead of reduced by the injected harmonic currents.

The poor harmonic filtering performance can also be concluded from the simulated result shown in Figure 5.11. In this case, the load consists of an ideal three phase diode rectifier with an infinite smoothing choke on the DC side. The DC current is completely flat, and hence also the phase currents when their corresponding diodes are conducting the current. In this case, the amplitudes of the current harmonics decline with the inverse of their corresponding harmonic order.

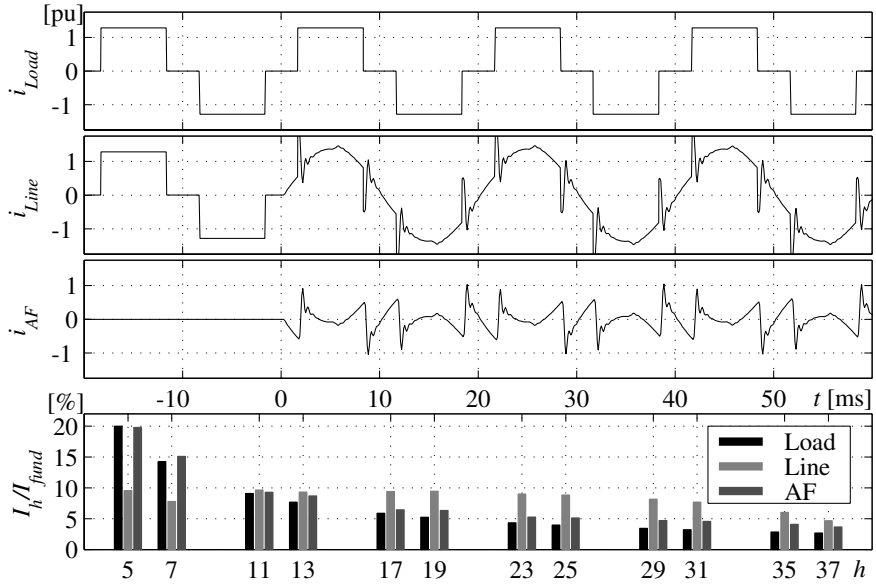

Figure 5.11 Simulated phase currents and the corresponding harmonic spectrum, when performing harmonic filtering with the original active filter controller.

Note the conformity of the resulting line current spectrum and the closed loop frequency response displayed in Figure 5.10. Nevertheless, the unacceptable poor filtering result demands for modification of the active filter controller in order to increase the harmonic filtering performance. The inherent phase deviation of the current controller has to be compensated for, which is the topic of the next section.

5.3 Direct phase compensation of the active filter controller

The main conclusion drawn in the previous section, is the need for compensation of the inherent phase delay in the line current controller. This phase delay is the main reason for the poor harmonic filtering and load balancing results of the original active filter controller. In this section, some basic methods that can be used for the compensation of the phase deviation in the current controller are described.

The phase deviation of the line current controller approximately corresponds to a three sample delay, see Figure 4.8. Hence, the phase compensation should provide a phase advance corresponding to three samples in order to cancel the inherent delay of the current controller.

Load balancing

In the load balancing case, the phase compensation is obtained in a straight forward manner, where the band pass filter output vector is rotated an angle corresponding to the desired phase advance. Hence, the argument of the current reference vector is modified to provide for the desired phase advance in the rotation direction of the negative-sequence vector. This phase compensation is described, in complex valued vector notation, by the following expression

$$\vec{i}_{AF}^{\,dq*} = \vec{i}_{Load,ns}^{\,dq} e^{j(-2\omega_1 \cdot 3T_s)} \tag{5.22}$$

Another approach [5], utilises lead-lag filters in the *d*- and *q*-axis components, respectively, to provide the phase advance of the current reference vector. The obtained result is the same, but the simplicity of the straight forward method is preferred.

The improved performance of the compensated active filter controller is concluded from the simulation result, shown in Figure 5.12, where the phase compensation given by (5.22) is applied. In this case the line current is totally balanced, compare to Figure 5.9 for the uncompensated results. The resulting line current contains only the positive-sequence component of the load current, which corresponds to the ideal case. This result further implies that the injected current equals the negative-sequence component of the load current.

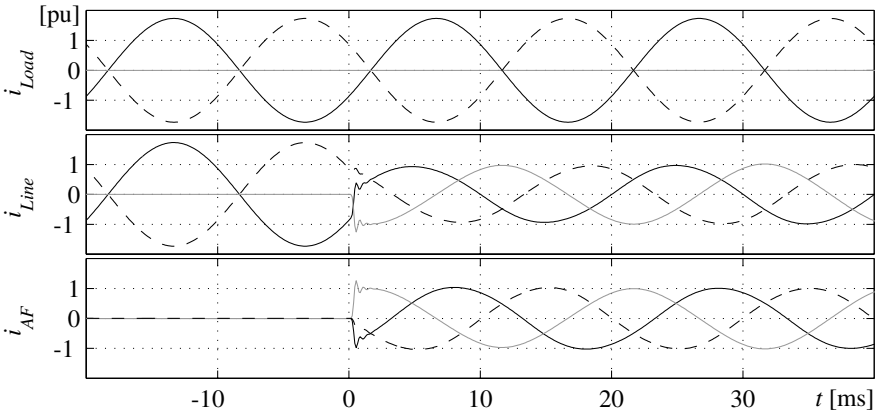

Figure 5.12 Simulated phase currents (phase *a* black, phase *b* grey, and phase *c* dashed black) when performing load balancing of a resistive two phase load with the phase compensated active filter controller.

Harmonic filtering

The straight forward method, applied for the fundamental negative-sequence current component, is not directly applicable in the harmonic filtering case. Since in the harmonic filtering case, several frequencies are concerned. The straight forward method would require similar band pass filters for each of the harmonics, in order to obtain the correct phase advance for every harmonic current component [20]. However, if the FFT method is employed in the load current identification, the corresponding phase of the harmonic current references can be advanced according to the straight forward method [24].

Since the phase deviation of the current controller corresponds to a three sample delay, the desired phase compensation is obtained by the prediction of the current harmonics three samples ahead in time. The periodicity of the current harmonics further implies that previous periods of the harmonic current can be used for the prediction. Hence, the predicted harmonic current is given by the harmonic current, one period minus three samples back. For each current harmonic this can be written

$$\hat{\vec{i}}^{\,dq}_{Load,h}(k+3) = \vec{i}^{\,dq}_{Load,h}(k - T_h + 3T_s) \tag{5.23}$$

where T_h is the time period of the corresponding current harmonic. The prediction (5.23) is generalised to be valid for all harmonics by selecting T_h according to the time period of the lowest current harmonic, i.e. the sixth harmonic in the synchronous reference *dq*-frame.

The realisation of the phase compensation is obtained by a shift register, with a length corresponding to the time period of the lowest order current harmonic. Hence, the harmonic current reference is given by

$$\vec{i}_{AF}^{\,dq*}(k) = \vec{i}_{Load,h}^{\,dq}(k - T_{shift\,register} + 3T_s) \tag{5.24}$$

The discrete state space description of (5.24) can generally be written

$$\begin{aligned} x_{sr}(k+1) &= \vec{A}_{sr}x_{sr}(k) + \vec{B}_{sr}\vec{i}_{Load,h}^{\,dq}(k) \\ \vec{i}_{AF}^{\,dq*}(k) &= \vec{C}_{sr}x_{sr}(k) + \vec{D}_{sr}\vec{i}_{Load,h}^{\,dq}(k) \end{aligned} \tag{5.25}$$

The closed loop state space representation of the phase compensated harmonic filter controller is obtained by inserting (5.25) into (5.21), which gives

$$\begin{aligned} \begin{bmatrix} X(k+1) \\ x_{sr}(k+1) \\ x_{hp}(k+1) \end{bmatrix} &= \begin{bmatrix} \vec{\Phi}_X^{dq} & \vec{\Gamma}_{i_2*}^{dq}\vec{C}_{sr} & \vec{\Gamma}_{i_2*}^{dq}\vec{D}_{sr}\vec{C}_{hp} \\ 0 & \vec{A}_{sr} & \vec{B}_{sr}\vec{C}_{hp} \\ 0 & 0 & \vec{A}_{hp} \end{bmatrix} \begin{bmatrix} X(k) \\ x_{sr}(k) \\ x_{hp}(k) \end{bmatrix} + \begin{bmatrix} \vec{\Gamma}_{i_2*}^{dq}\vec{D}_{sr}\vec{D}_{hp} \\ \vec{B}_{sr}\vec{D}_{hp} \\ \vec{B}_{hp} \end{bmatrix} \vec{i}_{Load}^{\,dq}(k) \\ \vec{i}_{Line}^{\,dq}(k) &= \begin{bmatrix} -\vec{C}_X^{dq} & 0 & 0 \end{bmatrix} \begin{bmatrix} X(k) \\ x_{sr}(k) \\ x_{hp}(k) \end{bmatrix} + \vec{i}_{Load}^{\,dq}(k) \end{aligned} \tag{5.26}$$

The effect of the applied phase compensating method is visualised by the frequency response shown in Figure 5.13. At the frequencies corresponding to the current harmonics in the synchronous reference *dq*-frame, the attenuation is improved in comparison to the original active filter controller. At least 20 dB, or ten times, reduction of the harmonic content of the line current is achieved.

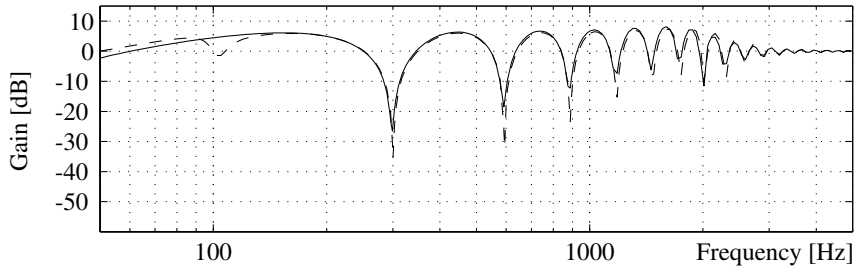

Figure 5.13 Closed loop frequency response for the compensated harmonic filter controller, positive-sequence (solid) and negative-sequence (dashed).

The main advantage of this compensation method is the simple realisation. However, it is seen in Figure 5.13 that the effect of the phase compensation decreases for the higher order current harmonics. This is due to the fact that for the higher order harmonics, the phase deviation of the current controller starts to differ from the assumed three sample phase delay, refer to Figure 4.8.

The simulated result, when performing harmonic filtering with the phase compensated active filter controller, is shown in Figure 5.14. As expected, the harmonic filtering performance is greatly improved in comparison to the result obtained with the original active filter controller, refer to Figure 5.11.

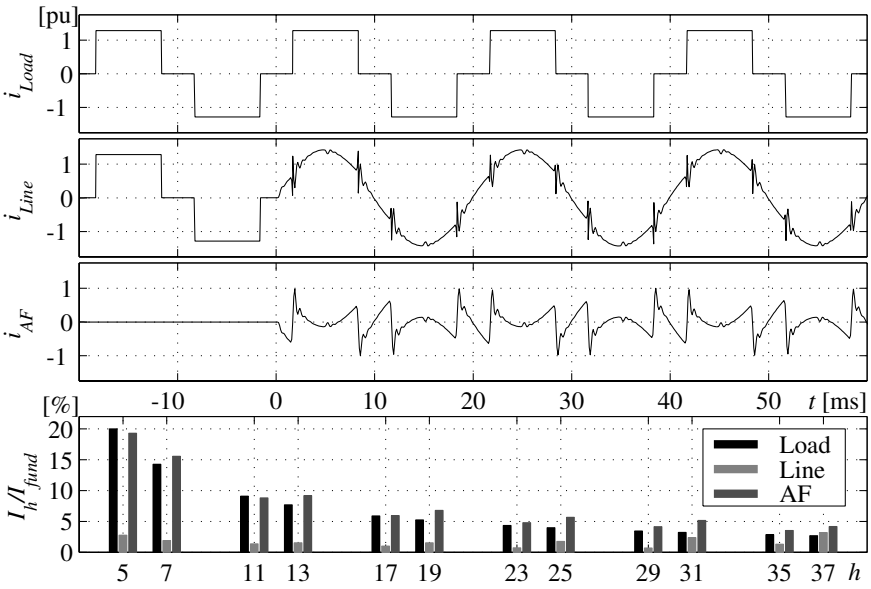

Figure 5.14 Simulated phase currents and the corresponding current spectrum obtained with the phase compensated active filter controller.

Phase compensated active filter controller

Figure 5.15 shows the block diagram representation of the phase compensated active filter controller. According to the discussion given above, the expected performance of this active filter controller is high. However, in a practical realisation of the phase compensated active filter controller, some degrading properties appear that is not modelled or taken into consideration when performing the theoretical analysis. In fact, the experimental results, given in Chapter 6, indicate quite poor filtering performance of the phase compensated active filter controller.

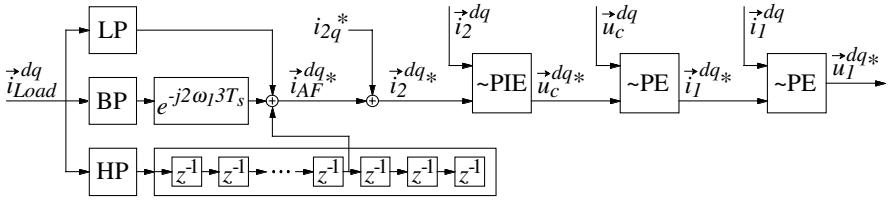

Figure 5.15 Block diagram scheme of the phase compensated active filter controller.

One degrading property is the sensitivity to variations in the system parameters. Since the active filter control is performed in open loop, the performance is determined by the accuracy of the estimated parameters used in the current controller. Uncertainties in these parameters cause the actual behaviour to differ from the expected. Consequently, the theoretically obtained frequency responses do not describe the actual system accurately. Tuning of the active filter controller parameters based on experimental results improves the performance, however this procedure is cumbersome and should be avoided in practice.

Furthermore, the non-linear properties of the VSC also have a degrading effect on the conditioning performance. For instance, the blanking time introduces current harmonics which are not compensated for, since they do not appear in the load current.

5.4 Rotating integrators in active filter control

In order to overcome the deteriorating properties of the phase compensated active filter controller, another improved active filter controller structure is proposed, where integrators in harmonic oriented reference frames are employed [6]. The main focus is to obtain a parameter insensitive active filter controller with high harmonic filtering performance in the steady state [6]. However, as will be shown in this section, additional features such as harmonic filtering selectivity is also achieved. Furthermore, the transient performance of the shunt AF is improved.

The idea of the proposed controller is based on the observation of the effect of the integrators applied in the outer current loop of the line current controller, described in Section 4.3. Due to the infinite gain at zero frequency of the integrator, the steady state error of the corresponding DC component is eliminated. As a consequence, the uncertainties concerning the DC component of the system are totally compensated for. In fact, this is equivalent to compensation of both the

gain and the phase deviation for the fundamental positive-sequence current component in the stationary reference $\alpha\beta$-frame.

Integrators applied in several harmonic oriented reference frames, where the corresponding current harmonics are represented as DC quantities, should have the same effect on the steady state errors of the corresponding current harmonics [32][35]. This implies that the injected harmonic current equals the harmonic content of the load current, and hence complete cancellation of the line current harmonics are obtained. Since this is already true in the reactive power compensation case, refer to Figure 5.8, the original active filter controller for reactive power compensation is kept unchanged. Furthermore, the same technique is used in a negative-sequence oriented reference frame, providing improved performance also of the load balancing property.

Parallel rotating integrator (PRI) controller structure

The block diagram representation of the proposed parallel rotating integrator (PRI) controller structure, where the additional harmonic oriented integrators are simply inserted in parallel to the original synchronous reference *dq*-frame integrator, is shown in Figure 5.16. Note that in the figure, only the integrators corresponding to the lower order current harmonics are shown, i.e. the 5th and 7th current harmonics. In the thesis, however, harmonic oriented integrators for the 5th up to the 25th current harmonics are employed.

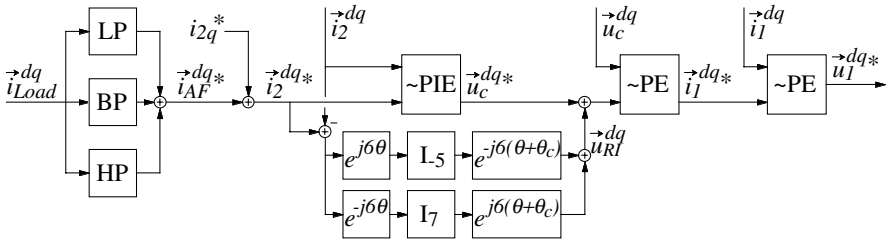

Figure 5.16 Principle block diagram representation for the PRI controller structure for active filters.

Note the additional compensation angle θ_c inserted in the transformation from the harmonic oriented reference frames back to the synchronous reference *dq*-frame. The effect of this additional compensation angle θ_c is discussed later on, at the moment it is sufficient to say that it improves the phase margin, or stability margin, of the PRI controller. This is especially important for the higher order current harmonics. However, as will be shown later, a suitable value for θ_c is

$$\theta_c = \frac{5}{2}\omega_1 T_s \tag{5.27}$$

In order to include the rotating integrator loops in the theoretical analysis, the equivalency of the vector transformation for continuous time and discrete time systems have to be given

$$\vec{s}^{\,\alpha\beta} \xrightarrow{e^{-j\omega_1 t}} \vec{s}^{\,dq} \Rightarrow \begin{cases} s \rightarrow s + j\omega_1 \\ q \rightarrow q \cdot e^{j\omega_1 T_s} \end{cases} \tag{5.28}$$

which describes the result of vector transformation between the stationary and the synchronous reference frames. Nevertheless, the basic principle given in (5.28) is easily extended to arbitrarily vector transformations.

Applying the relationship for the transformation of discrete time systems (5.28) on the rotating integrator loops, the complex valued discrete state space system, including the additional compensation angle, is found

$$\begin{aligned} \begin{bmatrix} I_{-5}(k+1) \\ I_7(k+1) \end{bmatrix} &= \overbrace{\begin{bmatrix} e^{-j6\omega_1 T_s} & 0 \\ 0 & e^{j6\omega_1 T_s} \end{bmatrix}}^{\vec{A}_{RI}} \begin{bmatrix} I_{-5}(k) \\ I_7(k) \end{bmatrix} + \overbrace{\begin{bmatrix} K_h e^{-j6\omega_1 T_s} \\ K_h e^{j6\omega_1 T_s} \end{bmatrix}}^{\vec{B}_{RI}} \left(\vec{i}_2^{\,dq*}(k) - \vec{i}_2^{\,dq}(k) \right) \\ \vec{u}_{RI}^{\,dq}(k) &= \underbrace{\begin{bmatrix} e^{-j6\theta_c} & e^{j6\theta_c} \end{bmatrix}}_{\vec{C}_{RI}} \begin{bmatrix} I_{-5}(k) \\ I_7(k) \end{bmatrix} \end{aligned} \tag{5.29}$$

The integral gain K_h is given by

$$K_h = \frac{1}{k_{uc}} \left(k_{i2} \frac{L_2}{T_s} \right) \frac{T_s}{\tau_h} \tag{5.30}$$

where τ_h corresponds to the selected time constant of the harmonic oriented integrators. Note that in order to correctly interpret the time constant, scaling with respect to the gain constant k_{uc} of the intermediate capacitor voltage P-controller has to be made. Basically, the time constant of the rotating integrators can be chosen equal to the time constant of the integrator used in the synchronous reference *dq*-frame controller. However, in order to improve the transient behaviour of the shunt AF, the time constants of the harmonic oriented integrators are selected according to

$$\tau_h = 10 \text{ ms} \tag{5.31}$$

Anyway, the effect of the time constant τ_h is discussed more in detail later on.

Extending the line current controller given by (4.49), again neglecting the grid voltage in the analysis, with the state space description of the rotating integrators (5.29) gives

$$\begin{aligned}\begin{bmatrix} X(k+1) \\ x_{RI}(k+1) \end{bmatrix} &= \begin{bmatrix} \vec{\Phi}_X^{dq} & \vec{\Gamma}_{RI}^{dq}\vec{C}_{RI} \\ -\vec{B}_{RI}\vec{C}_X^{dq} & \vec{A}_{RI} \end{bmatrix}\begin{bmatrix} X(k) \\ x_{RI}(k) \end{bmatrix} + \begin{bmatrix} \vec{\Gamma}_{i_2^*}^{dq} \\ \vec{B}_{RI} \end{bmatrix}\vec{i}_2^{dq*}(k) \\ \vec{i}_2^{dq}(k) &= \begin{bmatrix} \vec{C}_X^{dq} & 0 \end{bmatrix}\begin{bmatrix} X(k) \\ x_{RI}(k) \end{bmatrix}\end{aligned} \tag{5.32}$$

where

$$\vec{\Gamma}_{RI}^{dq} = \begin{bmatrix} 0 & \vec{L}_{\Sigma i_2} & 0 & 0 \end{bmatrix}^T \tag{5.33}$$

links the output of the rotating integrators to the converter voltage reference, refer to Section 4.3.

The closed loop discrete state space system of the PRI harmonic filter controller is then obtained by inserting the state space representation of the high pass filter (5.19) into (5.32)

$$\begin{aligned}\begin{bmatrix} X(k+1) \\ x_{RI}(k+1) \\ x_{hp}(k+1) \end{bmatrix} &= \begin{bmatrix} \vec{\Phi}_X^{dq} & \vec{\Gamma}_{RI}^{dq}\vec{C}_{RI} & \vec{\Gamma}_{i_2^*}^{dq}\vec{C}_{hp} \\ -\vec{B}_{RI}\vec{C}_X^{dq} & \vec{A}_{RI} & \vec{B}_{RI}\vec{C}_{hp} \\ 0 & 0 & \vec{A}_{hp} \end{bmatrix}\begin{bmatrix} X(k) \\ x_{RI}(k) \\ x_{hp}(k) \end{bmatrix} + \begin{bmatrix} \vec{\Gamma}_{i_2^*}^{dq}\vec{D}_{hp} \\ \vec{B}_{RI}\vec{D}_{hp} \\ \vec{B}_{hp} \end{bmatrix}\vec{i}_{Load}^{dq}(k) \\ \vec{i}_{Line}^{dq}(k) &= \begin{bmatrix} -\vec{C}_X^{dq} & 0 & 0 \end{bmatrix}\begin{bmatrix} X(k) \\ x_{RI}(k) \\ x_{hp}(k) \end{bmatrix} + \vec{i}_{Load}^{dq}(k)\end{aligned} \tag{5.34}$$

In Figure 5.17, the frequency response for the PRI harmonic filter controller, with integrators oriented to the 5th up to the 25th current harmonics, is displayed. The narrow notches, at the frequencies corresponding to the harmonics in the synchronous reference *dq*-frame, indicate the elimination of the corresponding current harmonics. Hence, the harmonic oriented integrators provide complete compensation of the degrading phase deviation in the original active filter controller. Furthermore, this is obtained independent of the system parameters.

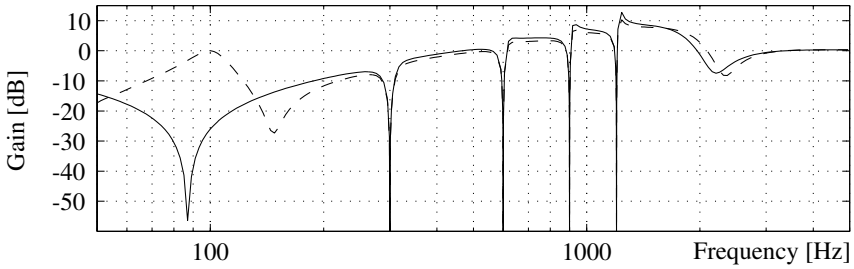

Figure 5.17 Closed loop frequency response for the PRI harmonic filter controller in the synchronous reference *dq*-frame, positive-sequence (solid) and negative-sequence (dashed).

Note the similarity between the frequency responses obtained with the PRI controller and the original harmonic filter controller shown in Figure 5.10. Except for the narrow notches in the PRI controller case, they appear to be identical. This implies that the higher order current harmonics, i.e. without corresponding integrators, still are affected by the phase deviation of the line current controller. Hence, these current harmonics are even amplified instead of reduced, which can be concluded from Figure 5.17.

The conclusions drawn from the frequency response, of the PRI harmonic filter controller, are confirmed by the simulated results shown in Figure 5.18. The current harmonics with corresponding integrators are practically eliminated. This implies that the remaining oscillation in the line current is completely due to the higher order current harmonics, partly present in the load current and partly due to the injected filtering current. This is concluded from the plotted harmonic spectrum of the currents. Furthermore, it can be concluded that the settling time of the integrators correspond to the selected time constant τ_h.

The still remaining degrading property of the PRI harmonic filter controller, i.e. the amplification of the higher order current harmonics, is due to the direct path provided by the P-controllers through the cascaded controller structure. The consequence of this is that the controller puts as much control effort on these higher order current harmonics, despite the fact that the produced control actions only decreases the performance of the active filter. However, this is circumvented by the removal of the direct path through the active filter controller. In fact, this is accomplished for the active filter controller described next, which still has the advantages but lacks the drawbacks of the PRI controller.

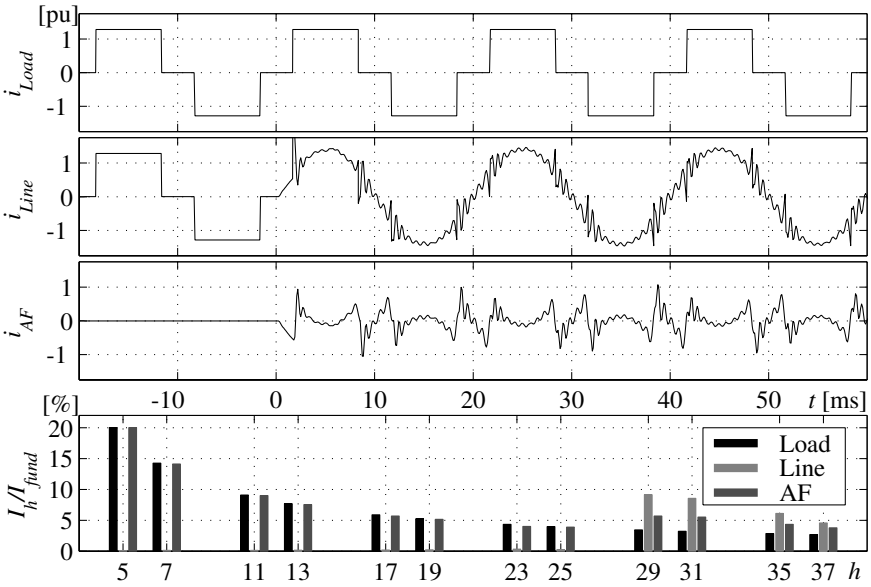

Figure 5.18 Simulated phase currents and their harmonic content, when performing harmonic filtering with the PRI controller.

Multiple rotating integrator (MRI) controller structure

In order to overcome the remaining drawback of the PRI harmonic filter controller, i.e. the amplification of higher order current harmonics, a further improved rotating integrator controller is proposed. Basically, the idea is to remove the direct path through the cascaded controller structure for the current harmonics. This is obtained by removing the path from the high pass and the band pass filter outputs to the line current controller. These filter outputs are instead only input to the multiple rotating integrator (MRI) loops, see Figure 5.19. As a consequence, harmonic selectivity is obtained since only current harmonics with corresponding integrators are filtered. Hence, in this thesis the 5^{th} up to the 25^{th} current harmonics are filtered, while the higher order current harmonics are left unfiltered.

Note the additional anti windup block (AW) inserted in the figure, which is described later on. Also note the principle difference regarding the band pass and high pass filter inputs. This implies that the current of the battery charger also is filtered. However, the filters are not essential for the function of the harmonic oriented integrators, and hence can be left out in the MRI active filter controller. Nevertheless, their presence reduce the ripple in the harmonic oriented integrators caused by the fundamental

current component, whose magnitude is several times higher than any of the current harmonic magnitudes.

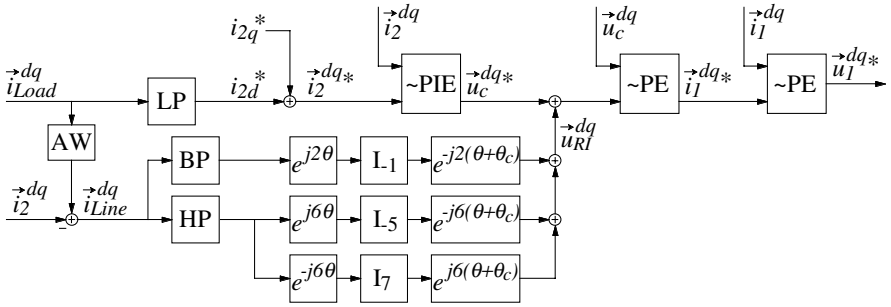

Figure 5.19 Principle block diagram representation for the MRI controller structure for active filters.

The parameters for the MRI loops, i.e. the compensation angle θ_c and the time constant for the harmonic oriented integrators τ_h, are chosen equal to the PRI harmonic filter controller. However, the time constant of the negative-sequence oriented integrator is selected to

$$\tau_{ns}=100 \text{ ms} \tag{5.35}$$

which is due to the longer response time of the band pass filter, refer to Figure 5.6.

For the MRI harmonic filter controller, the complex valued discrete state space representation is given by

$$\begin{bmatrix} X(k+1) \\ x_{RI}(k+1) \\ x_{hp}(k+1) \end{bmatrix} = \begin{bmatrix} \vec{\Phi}_X^{dq} & \vec{\Gamma}_{RI}^{dq}\vec{C}_{RI} & 0 \\ -\vec{B}_{RI}\vec{D}_{hp}\vec{C}_X^{dq} & \vec{A}_{RI} & \vec{B}_{RI}\vec{C}_{hp} \\ -\vec{B}_{hp}\vec{C}_X^{dq} & 0 & \vec{A}_{hp} \end{bmatrix} \begin{bmatrix} X(k) \\ x_{RI}(k) \\ x_{hp}(k) \end{bmatrix} + \begin{bmatrix} 0 \\ \vec{B}_{RI}\vec{D}_{hp} \\ \vec{B}_{hp} \end{bmatrix} \vec{i}_{Load}^{dq}(k)$$

$$\vec{i}_{Line}^{dq}(k) = \begin{bmatrix} -\vec{C}_X^{dq} & 0 & 0 \end{bmatrix} \begin{bmatrix} X(k) \\ x_{RI}(k) \\ x_{hp}(k) \end{bmatrix} + \vec{i}_{Load}^{dq}(k) \tag{5.36}$$

which is similar to the PRI harmonic filter controller case (5.34).

The absence of the direct path, in the MRI harmonic filter controller, results in the fact that the higher order harmonics are left unfiltered. This is concluded from the closed loop frequency response of the MRI harmonic filter controller (5.36) displayed in Figure 5.20. The gain is

approximately unity for all frequencies except at the frequencies of the corresponding integrators.

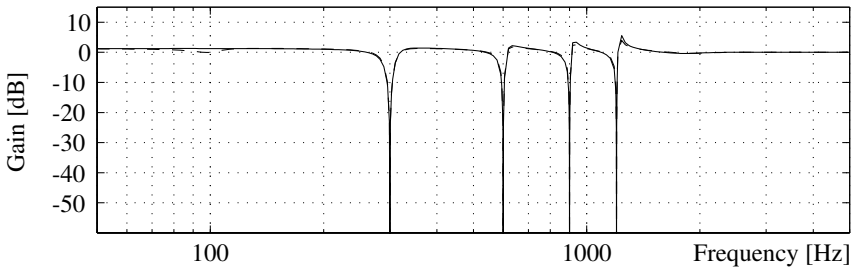

Figure 5.20 Closed loop frequency response for the MRI controller with corresponding integrators for the 5th up to the 25th current harmonics, positive-sequence (solid) and negative-sequence (dashed).

The pole and zero map of the MRI harmonic filter controller (5.36) is shown in Figure 5.21. The narrow notches in the frequency response are due to the pole and zero pairs located in the vicinity of the unit circle. In fact, the zeroes are actually on the unit circle, which causes the cancellation of the corresponding frequency component, i.e. the depth of the notches in the frequency response. In [36], an active filter controller based on notch filters in the controller was proposed resulting in a similar pole and zero map.

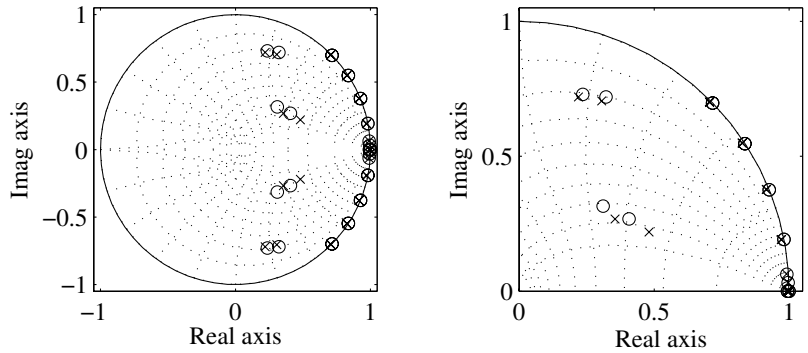

Figure 5.21 Pole and zero map for the closed loop MRI harmonic filter controller. The right plot shows a close up of the first quadrant.

Note that the location of the poles corresponding to the original line current controller, without the MRI loops, are proportionately unchanged, refer to the pole map shown in Figure 4.7.

The simulated result, when performing harmonic filtering with the MRI controller, is shown in Figure 5.22. The superiority of the proposed MRI

controller, compared to the previous cases, is clearly seen. The current harmonics up to 25th are eliminated, whereas the even higher order current harmonics are left unfiltered.

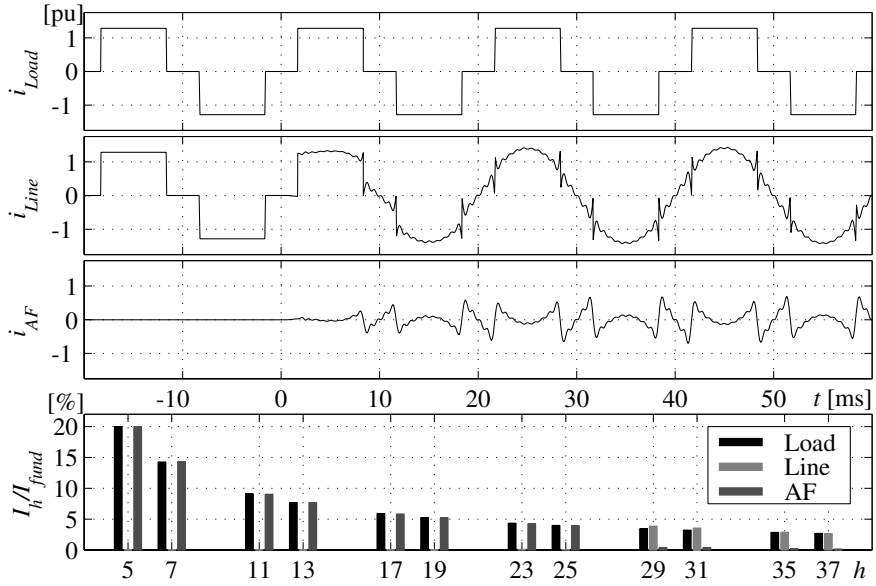

Figure 5.22 Simulated phase currents and their harmonic content obtained with the MRI harmonic filter controller.

Note that the response time of the MRI controller corresponds to the selected time constant τ_h of the harmonic oriented integrators. This is further verified in Figure 5.23, where the harmonic oriented integrator outputs for the lowest and highest orders of current harmonics are shown.

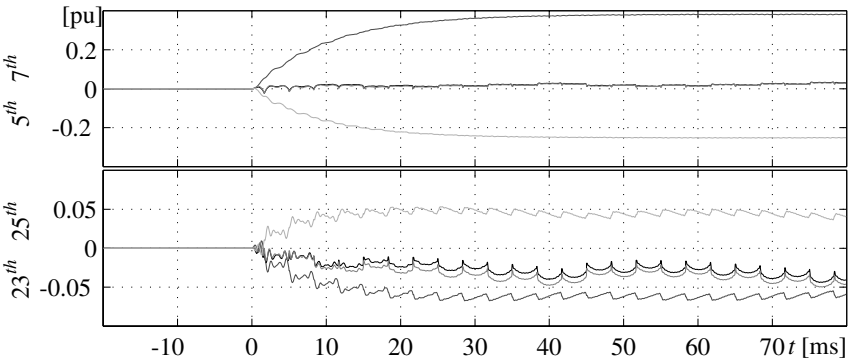

Figure 5.23 The integrator outputs for the simulation of the MRI harmonic filter controller, top) 5th dark and 7th light, and bottom) 23rd dark and 25th light.

Note that the ripple in the integrators of the lower figure is due to the remaining higher order current harmonics still present in the line current.

An additional feature of the MRI controller concerns the transient behaviour of the shunt AF. In the MRI controller case, the low pass filtering property of the integrators neutralises the transient coupling in the high pass filter output shown in Figure 5.6. Hence, the time constant τ_h of the harmonic oriented integrators determines the transient response time of the MRI controller.

Anti windup schemes for the MRI controller

The MRI controller provides for simple counter-measures in order to prevent from windup of the harmonic oriented integrators. It is recognised that integrator windup or integrator runaway only occurs when the VSC, i.e. the actuator, output is limited by the DC-link voltage, refer to the discussion in Section 3.2. Hence, if overmodulation of the VSC is prevented, then integrator windup can not occur.

Overmodulation of the VSC appears, in steady state, when the voltage drop across the LCL-filter becomes larger than the margin between the DC-link voltage and the grid voltage. This voltage drop is dependent both on the magnitude of the injected current harmonics and on the equivalent impedance of the filter seen from the VSC. However, the influence of the latter is reduced by the use of a LCL-filter in comparison to an ordinary L-filter, refer to the discussion in Section 3.4.

Anti windup is achieved in steady state either by reducing the magnitudes of the injected current harmonics or by omitting some of the harmonic oriented integrators. Hence, anti windup is ensured at the expense of a reduced filtering performance. In the first case, this can be accomplished by reducing the amount of the load current prior to the band pass and high pass filters. This principle is shown in Figure 5.19, where the AW block simply consists of a scaling factor. The value for the scaling factor AW is then determined by the following simple algorithm

```
if overmodulation
   AW:=MIN(0,AW-0.01)
else
   AW:=MAX(1,AW+0.0001)
```

Note that the decrement should be considerably larger than the increment in order to accomplish anti windup in steady state.

In the second case, anti windup is provided by continuous reset of the corresponding integrators of the current harmonics to be omitted, preferably applied to the higher order harmonic oriented integrators.

Influence of the MRI parameters

The influence of the rotating integrator parameters, i.e. θ_c and τ_h, have previously not been discussed. The value of the compensation angle θ_c is, however, crucial in order to obtain stability of the MRI controller. This is especially important for the higher order harmonic oriented integrators. The time constants τ_h and τ_{ns}, on the other hand, determines the transient characteristics of the MRI controller.

In Figure 5.24, the loci of the poles and zeroes of the MRI controller is shown when the rotating integrator parameters are altered. Note that only the poles and zeroes corresponding to the highest order harmonic oriented integrators, i.e. for the 23rd and 25th current harmonics, are shown. It is concluded that the proposed set of θ_c and τ_h gives a stable system, since the poles are inside the unit disc.

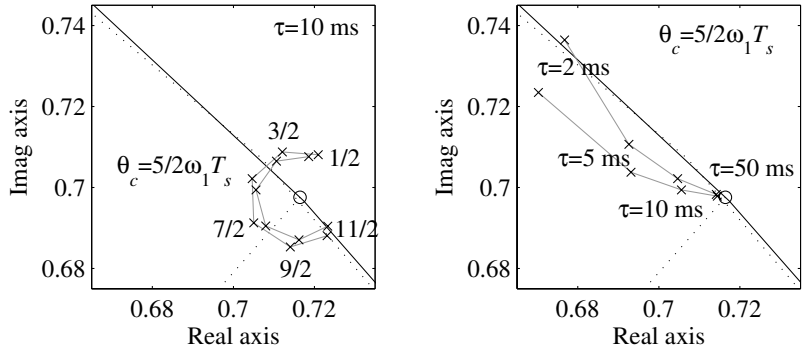

Figure 5.24 Part of loci of pole and zero map for the MRI harmonic filter controller, varying θ_c (left) and varying τ_h (right).

Note that the dotted line corresponds to the frequency of the investigated harmonic in the synchronous reference *dq*-frame.

Figure 5.25 shows the effect on the frequency response, caused by the parameter variations of the MRI controller. Note the principle difference in the location of the peaks when the compensation angle θ_c is altered. This is due to the fact that the corresponding frequency, i.e. location, of the poles differ more or less from the frequency of the zeroes involved. The closer to the corresponding frequency line, the less distorted frequency response.

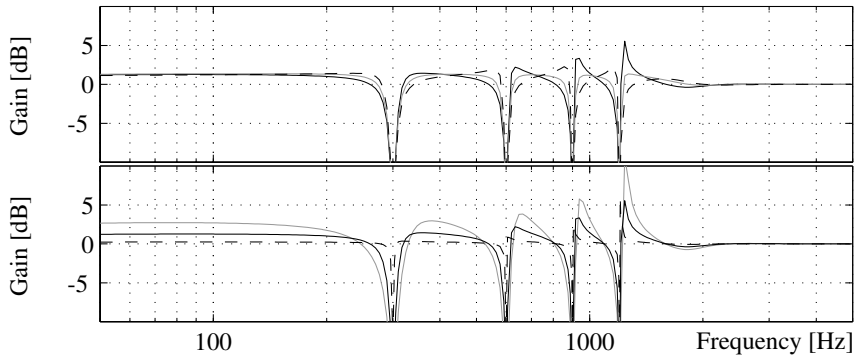

Figure 5.25 Influence of the MRI parameters on the frequency response for the MRI harmonic filter controller. Top) $\theta_c = 5/2\omega_1 T_s$ (black), $7/2\omega_1 T_s$ (grey), and $9/2\omega_1 T_s$ (dashed black). Bottom) $\tau_h = 5$ ms (grey), 10 ms (black), and 50 ms (dashed black).

Furthermore, the width of the notches are narrowed with increasing time constant, and at the same time the bias in between the notches is lowered. This is due to the more closely aligned poles and zeroes for larger time constants. Hence, a trade of between the response time and the intermediate bias has to be made. This is especially important for the highest order harmonic oriented integrators, since a high bias results in the amplification of the even higher order current harmonics, refer to Figure 5.25.

Note that the analysis given reveals that the selected set of MRI parameters are not the optimal choice. In fact, the compensation angle θ_c should preferably have been selected to $7/2\omega_1 T_s$, since in this case the frequency correspondence of the poles and zeroes are improved. Nevertheless, the main objective in terms of high steady state conditioning performance is fulfilled with the proposed set of MRI parameters.

6

Experiments

In this chapter, the experimental results of the proposed battery charger are presented. The basic current controllers described in Chapter 4 are verified. However, the emphasis is put on the grid conditioning results and especially the properties of the proposed MRI active filter controller.

6.1 Experimental set-up

The experimental set-up is shown in Figure 6.1. Note that the power grid should be connected in the lower leftmost part of the figure. The three phase diode rectifier is applied in order to generate the load current to be conditioned by the shunt AF part of the battery charger. The diode rectifier load is purely resistive, i.e. a lamp ballast. Note that the load current is not explicitly measured, instead it is estimated from the measured supply (line) current and the battery charger current.

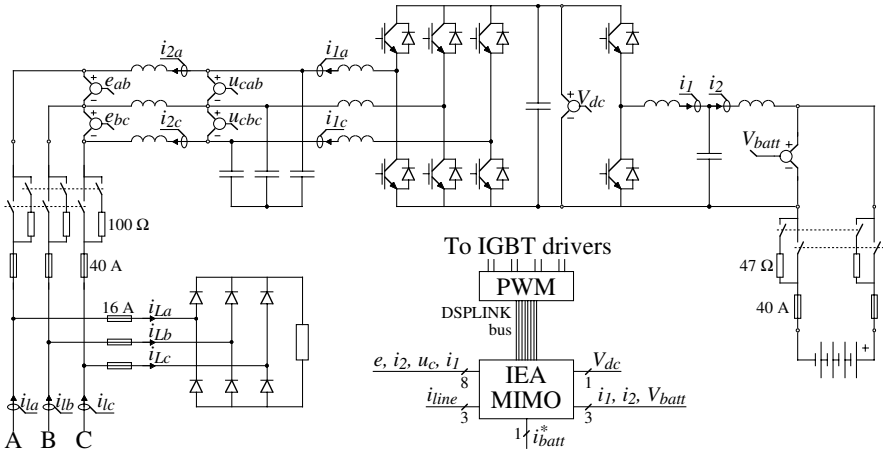

Figure 6.1 Schematic layout of the experimental set-up.

The battery package, shown in the lower right of the figure, actually consists of a rotating converter, where the armature circuit of a DC machine is used as a battery equivalent. The nominal DC voltage of the

battery equivalent is 240 V, which implies that the maximum charging power is lower than the rated power of the battery charger.

The surge currents are limited by the additional resistors in series with the source to be connected. Initially at system start up, the contactors in series with the current limiting resistors are closed. After the initial surge transient, the main contactors are closed and thus short circuits the current limiting resistors. The contactors in series with the current limiting resistors are at the same time released. This is automatically controlled by timer relays, which are not shown in Figure 6.1.

The VSCs actually consist of six SKM50GB123D half bridge modules, where the additional two modules are due to the implementation of the quasi resonant DC link converter described in [18]. The modules are rated 1200 V and 40 A at 80 °C case temperature. The driver SKHI23/12, also manufactured by Semikron, is used. Furthermore, the blanking time of the IGBTs is selected to 4 μs.

The DC link capacitor value is given in Chapter 3. The DC link capacitor consists of four electrolytic capacitors, two series connected capacitor pairs in parallel in order to sustain the DC link voltage and the DC link current. Furthermore, additional capacitors, i.e. resonant link capacitors [18], distributed among the half bridges serve as overvoltage snubbers.

The output filter parameters are according to the design expressions given in Chapter 3. The inductors are wound on iron powder cores manufactured by Micrometals, refer to [18]. The filter capacitors consists of polypropylene capacitors manufactured by Icar.

The control algorithms are implemented in the IEA MIMO controller [7], which is based on the TMSC320C30 floating point DSP. The main characteristics of the IEA MIMO controller are, simultaneous sampling of 16 analogue inputs with 12 bits resolution, 8 analogue outputs, and a DSPLINK bus for expansion boards, i.e. the PWM board. The PWM board consists of a triangular carrier wave generator and comparators in order to generate the instantaneous switching states of the VSCs. The sampling instants of the IEA MIMO are synchronised to the triangular carrier end-points via the DSPLINK bus. Note that all 16 analogoue inputs are used for control purposes, where the final input is used for the battery current reference. The 8 analogue outputs are used for debug and controller analysis.

The currents are measured with LEM LA50P current transducers, which provides galvanic isolation and high bandwidth. The AC voltages, i.e. grid

voltage and line filter capacitor voltage, are measured with transformers, whereas the DC voltages, i.e. DC link voltage and the battery voltage, are measured with LEM LV25P voltage transducers. Hence, galvanic isolation is obtained also on the voltage measurements. The transducer outputs are converted to suitable electronic voltage levels by operational amplifiers.

The measurements shown in this chapter are obtained with a Tektronix TDS 640A four channel digitising oscilloscope, where each channel is stored by 2000 sample points in memory. The stored data have then been transferred to a computer, where MATLAB™ is used in order to perform further analysis and plotting of data. However, in order to reduce the effect of measurement noise in the results, the 2000 samples are split into 500 cells each containing four adjacent samples. The time domain results given in this chapter are then provided as the mean values of each four sample cell. This considerably decreases the noise in the measurement results shown in this chapter.

6.2 Current control verification – Step response

In order to confirm the transient behaviour of the current controllers used in the battery charger, they have been exposed to step changes in the reference currents. In Figure 6.2, the step response of the line current controller is shown. Note that repeated changes in both the *d*- and *q*-axis current components are made simultaneously. This implies that the line current controller does not enter steady state. Furthermore, the pulses in the *q*-current component are centred around zero in order to prevent from any active power flow, in average, during the measurement. The reason for this is that the battery side of the unit is turned off during this measurement, in order not to interfere with the line current controller analysis. However, the instantaneous active power flow affects the DC-link voltage, which results in DC-link voltage controller action that is added to the step changes in the *q*-component of the reference current. This explains the slight deviation during the pulses in the *q*-axis reference current component shown in Figure 6.2.

The deviation from the simulated step response, shown in Figure 4.9, is apparent. There exist no simple explanation for this deviation in the measurement. However, uncertainties in model parameters, imperfect decoupling of the *d*- and *q*–axis components, the non-linear properties of the VSC and measurement noise surely contribute to the deviation. Nevertheless, the step responses shown satisfy the requirements of the application. In any case, the integrators provided in the outer current control loop reduce the current error in steady state.

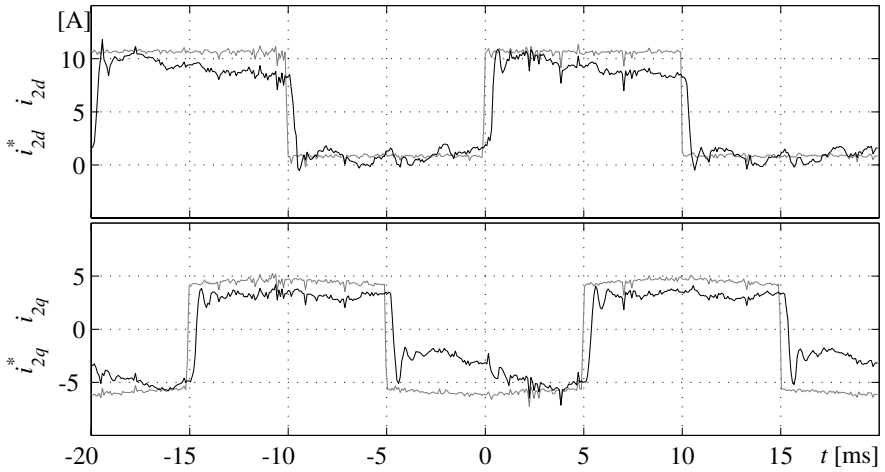

Figure 6.2 Step response in the *d*-and *q*-axis current components of the line current controller, reference currents (grey) and resulting currents (black).

In Figure 6.3, the step response of the battery current controller is shown. In this case, the conformity to the simulated step response shown in Figure 4.5 is good, except for the DC offset in the battery current during the current pulses. The DC offset is due to the fact that the integrator, in the outer current control loop, does not enter steady state. The selected time constant of the integrator is longer than the width of the current pulses.

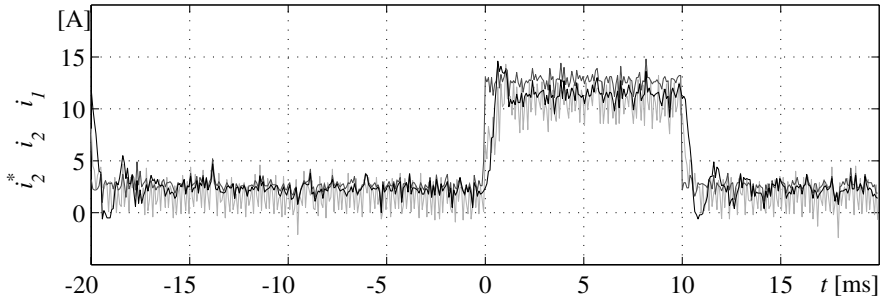

Figure 6.3 Step response of the battery current controller, reference current i_2^* (dark grey), outer current i_2 (black), and inner current i_1 (light grey).

6.3 Charging of battery equivalent

The measured currents when charging the battery equivalent are shown in Figure 6.4. From the figure, it is clear that the condition for sinusoidal line current when charging is met. Furthermore, the reactive power requirements of the filter capacitors are accommodated by the VSC

resulting in unity power factor for the unit, which can be concluded from the slight phase difference in between the outer and inner phase currents.

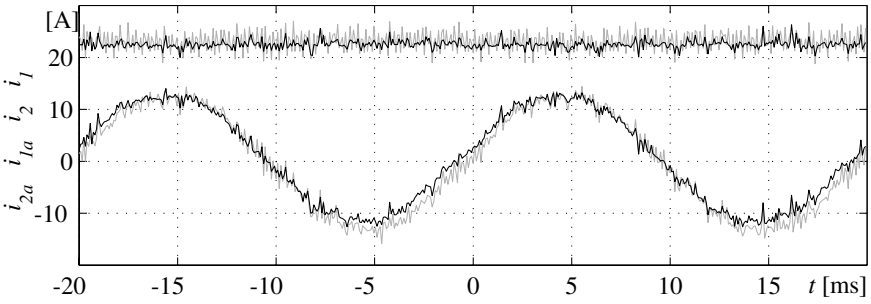

Figure 6.4 Charging currents. Top) battery currents, outer current i_2 (black) and inner current i_1 (grey). Bottom) line currents, outer phase current i_{2a} (black) and inner phase current i_{1a} (grey).

In Figure 6.5, the same currents are shown in a shorter time scale. Note the high frequency oscillations of ≈35 kHz contained in the currents. Their presence are unexplainable and attributed to measurement and/or system noise. Nevertheless, the switching frequency current ripple of 5 kHz is clearly seen in the inner inductor currents, i.e. i_1 and i_{1a}, shown in grey in the figure. The effective damping provided by the LCL-filters practically eliminates this content in the outer inductor currents shown in black.

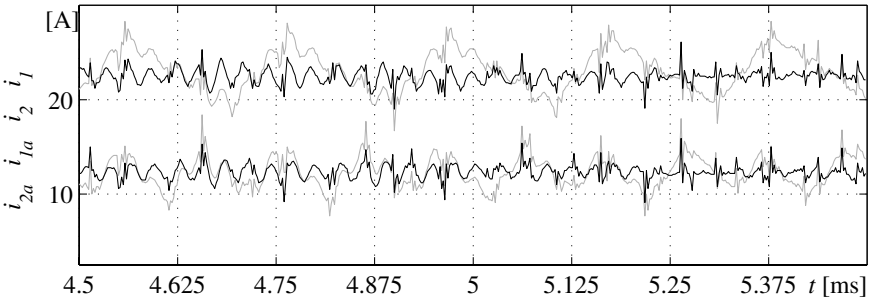

Figure 6.5 Charging currents in the short time scale. Top) battery currents, outer current i_2 (black) and inner current i_1 (grey). Bottom) line currents, outer phase current i_{2a} (black) and inner phase current i_{1a} (grey).

When the battery charger is idle running, the current into the battery charger should be zero in the ideal case. However, losses in the passive filter and in the VSC cause an active current component in order to preserve the DC-link voltage at its nominal value. The introduced 4 μs dead time, or blanking time, in the IGBT driver circuits causes low order current harmonics in the phase currents. Furthermore, grid voltage

distortion also causes low order current harmonics. In Figure 6.6, the phase current when the unit is idle running is shown. Note the high 5th harmonic current component, which is mainly due to the blanking time of the VSC.

The effect of the blanking time, i.e. the low order current harmonics, is greatly reduced by the MRI controller as shown in the middle of Figure 6.6. In this case, the line current is practically sinusoidal with fundamental frequency. This implies that the MRI controller is capable of reducing the internally generated current harmonics of the battery charger. As a consequence, the MRI controller can be applied to an electrical drive for reduction of the torque ripple caused by the blanking time or/and the semiconductor forward voltage drops.

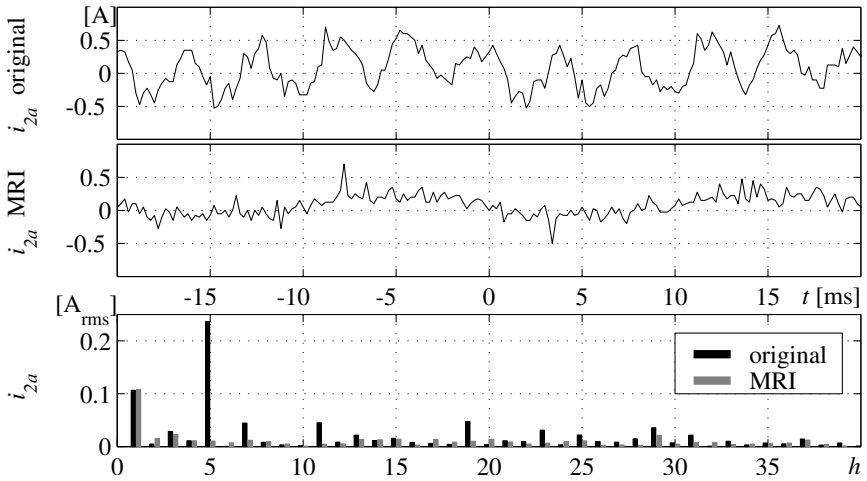

Figure 6.6 Phase current when unit is idle running. Top) original controller, middle) with MRI controller, and bottom) harmonic content of the currents above.

The spectrum of the phase currents is shown in the lower part of the figure. The harmonic content of the phase current in the MRI controller case is, in fact, reduced down to the noise floor of the experimental set-up.

Note that the RMS-values of the fundamental current components are equal in the two cases. Furthermore, the idle reactive current in the filter capacitors corresponding to 0.73 A_{rms}, i.e. 5 % of the nominal line current according to the design given in Section 3.4, is accommodated by the VSC.

6.4 Load balancing of a two-phase load

In order to confirm the load balancing characteristics of the investigated battery charger, an asymmetrical load is used. The asymmetrical load consists of a purely resistive load, i.e. a lamp ballast, connected in between phases *a* and *c*. In fact, the three phase diode rectifier is used also in this case, where the *b* phase is disconnected by means of the fuse. Hence, the resulting load current contains equal amount of positive- and negative-sequence current components of fundamental frequency. The ideal result of load balancing should therefore correspond to a resulting line current which only contains the positive-sequence current component of fundamental frequency.

In Figure 6.7, the result of load balancing with the direct phase compensated active filter controller is shown. Since the phase order of the injected AF current is *acb*, it is clear that the injected AF current consists of a negative-sequence current component. However, the resulting line current still contains an asymmetry, which implies that the load is not totally compensated for. This differ from the simulated result shown in Figure 5.12, where complete compensation of a similar load is obtained with the phase compensated active filter controller.

From the experimental result, it is clear that the amplitude of the injected negative-sequence current component is not sufficient in order to cancel the asymmetry in the line currents. This is due to the sensitivity to the line current controller parameters, which implies that the gain is not unity for the negative-sequence current component.

The sensitivity to the parameters of the line current controller is reduced by the MRI controller, which is due to the integrators introduced. In Figure 6.8, the result when performing load balancing with the MRI controller is shown. It is clear that the load is fully compensated for in this case. The resulting line current contains only the positive-sequence current component of the two phase load, while the injected current by the shunt AF provides the negative-sequence current component of the load current. Hence, the advantageous characteristics of the introduced negative-sequence oriented integrator for the negative-sequence current component are confirmed.

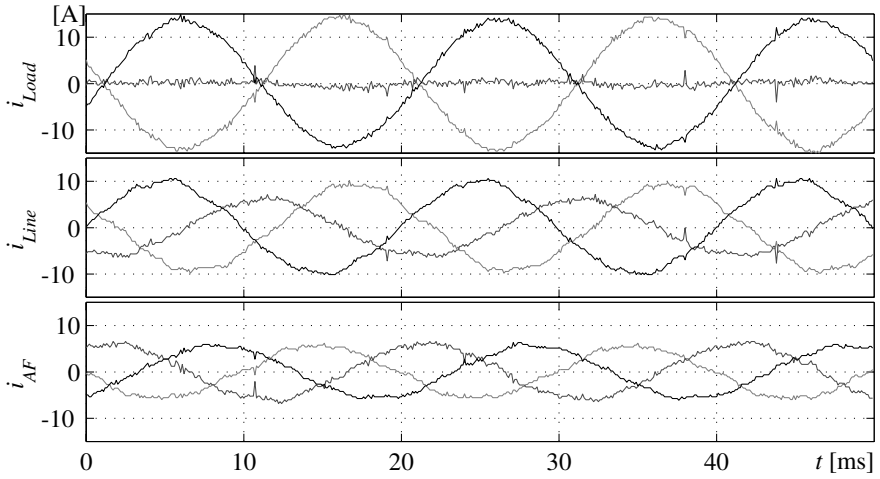

Figure 6.7 Phase currents, *a* (black), *b* (dark grey), and *c* (light grey), when performing load balancing with the direct phase compensated controller. Top) estimated load currents, middle) resulting line currents, and bottom) AF currents.

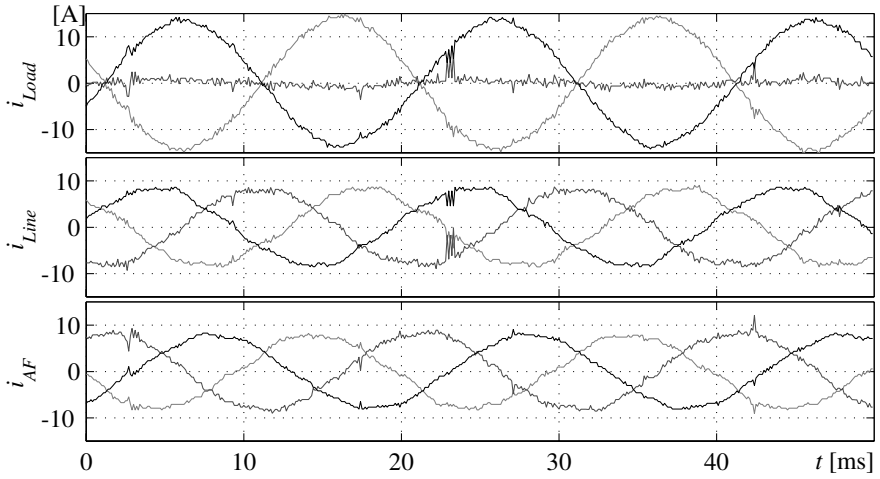

Figure 6.8 Phase currents, *a* (black), *b* (dark grey), and *c* (light grey), when performing load balancing with the MRI controller for the negative-sequence current component. Top) estimated load currents, middle) resulting line currents, and bottom) AF currents.

Note that the MRI controller in this case only contains the negative-sequence oriented integrator. This implies that the presence of current harmonics are due to the effect caused by the blanking time and the grid voltage distortion, which is previously described.

6.5 Harmonic filtering of a diode rectifier

The harmonic filtering property of the investigated battery charger is confirmed by the filtering of the current harmonics produced by the three phase diode rectifier. The three phase diode rectifier is loaded by an equivalent resistor, which is previously described.

For the direct phase compensated active filter controller, the result of harmonic filtering is shown in Figure 6.9. As can be seen, the measured harmonic filtering result is quite poor. The harmonic reduction is only 50-70 % in the measured case, which should be compared to the anticipated reduction of at least 90 % from the theoretical analysis, refer to Section 5.3. The difference is again due to the sensitivity to the parameters in the line current controller. The major cause for the remaining line current harmonics is given by the difference in the amplitudes of the injected current harmonics in comparison to the load current harmonics. This is concluded from the spectrum of the harmonic content of the currents displayed in Figure 6.9, which indicates that the gain of the experimental set-up is lower than unity for the current harmonics concerned.

However, the phase compensation, i.e. the phase advance corresponding to three samples, still improves the harmonic filtering performance. This is concluded from the fact that the remaining harmonic content of the line current is directly given by the subtraction of the injected current harmonics from the load current. This implies that the phase of the injected current harmonics corresponds to the load current harmonics. However, this is only true for the lower order current harmonics, i.e. up to the 13^{th} current harmonic. For the higher order current harmonics the phase correspondence is deteriorated, which in fact was anticipated from the theoretical analysis.

In Figure 6.10, the measured result obtained with the proposed MRI harmonic filter controller is shown. The MRI controller contains harmonic oriented integrators for the 5^{th} up to the 25^{th} harmonic orders. The harmonic filtering result is excellent and, furthermore, completely in accordance with the theoretical analysis. The effect of the inserted rotating integrators are twofold. First, the gain deviation of the line current controller is completely compensated for, which implies that the gain is unity for the corresponding harmonic frequencies. Second, the phase correspondence in between the injected current harmonics and the load current harmonics are complete.

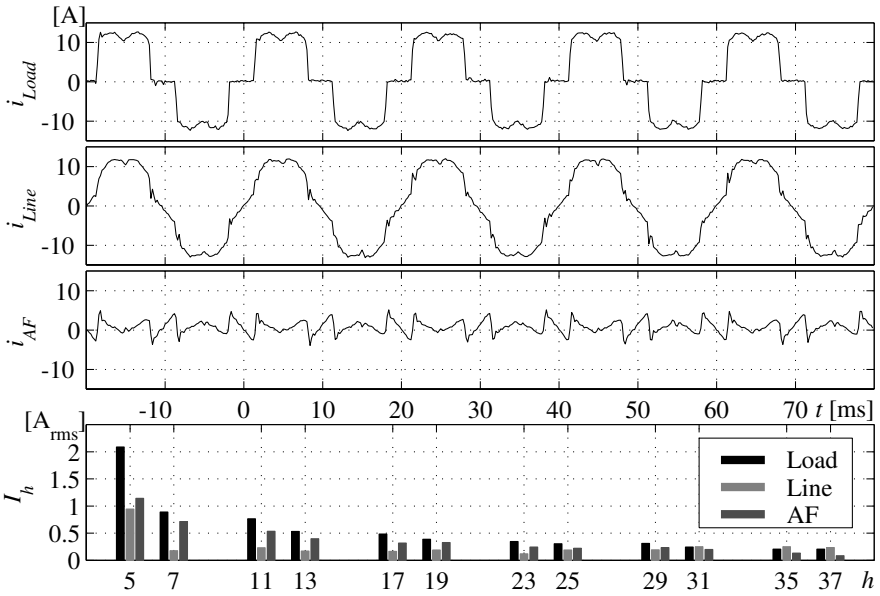

Figure 6.9 Result of harmonic current filtering with the direct phase compensated active filter controller. From top to bottom: estimated load current, line current, injected AF current, and the harmonic content of the currents.

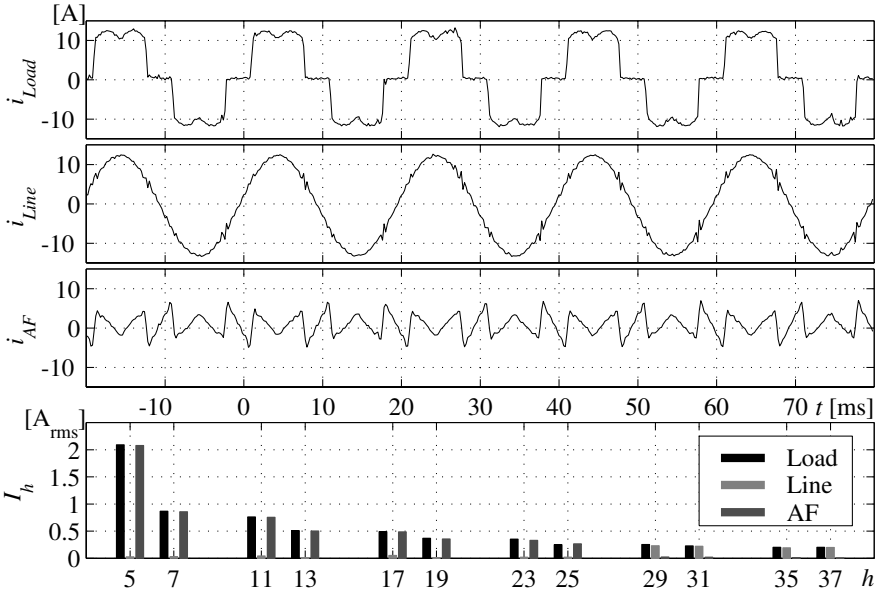

Figure 6.10 Result of harmonic current filtering with the MRI controller. From top to bottom: estimated load current, line current, injected AF current, and the harmonic content of the currents.

The additional advantageous characteristic of the MRI controller, regarding the harmonic selectivity, is also confirmed by the measured results. In this case, this corresponds to the fact that the higher order current harmonics are left unfiltered.

6.6 Dynamics of the MRI controller

From the theoretical analysis on the dynamics of the MRI harmonic filter controller, it is found that the response times of the harmonic oriented integrators are given by the selected time constants. This is further confirmed by the simulated results. Since the same value for the time constants of the harmonic oriented integrators are selected for the experimental implementation, the anticipated response time of the MRI controller should thus be 10 ms. In Figure 6.11, the harmonic filtering currents at turn on of the MRI controller are shown.

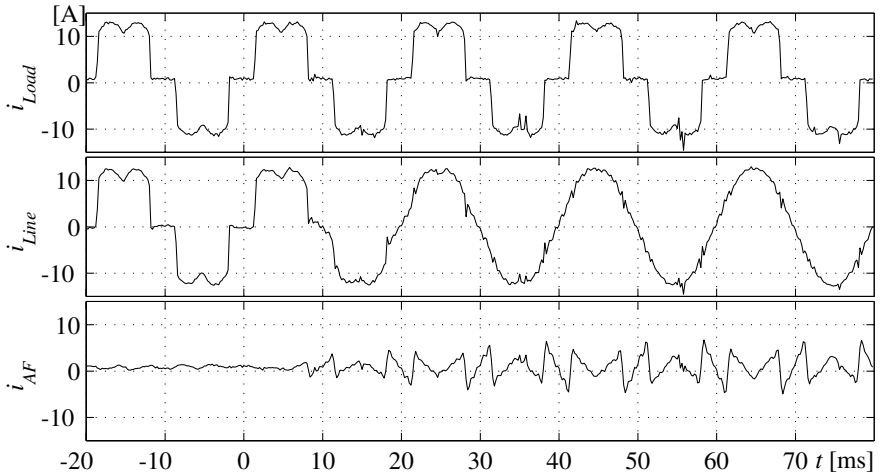

Figure 6.11 Turn on of the MRI harmonic filter controller, top) estimated load current, middle) resulting line current, and bottom) injected AF current.

The harmonic oriented integrator outputs for the lowest and highest orders of the corresponding current harmonics are displayed in Figure 6.12. In this case the response time of the integrators are extended compared to the simulated case. In fact, the response time is approximately doubled. Also the integrators oriented to the higher order harmonics have further a prolonged settling time.

The extended response time of the harmonic oriented integrators is certainly due to a number of reasons. Here, two reasons are given. First, the interpretation of the integrator time constant is obtained from the line

current controller parameters according to (5.30). Consequently, variations in the system parameters decreases the validity of this interpretation, which causes another time constant than the anticipated. Second, the blanking time introduced in the VSC increases the settling time of the integrators, since the effect of the blanking time is dependent on the operating point of the converter.

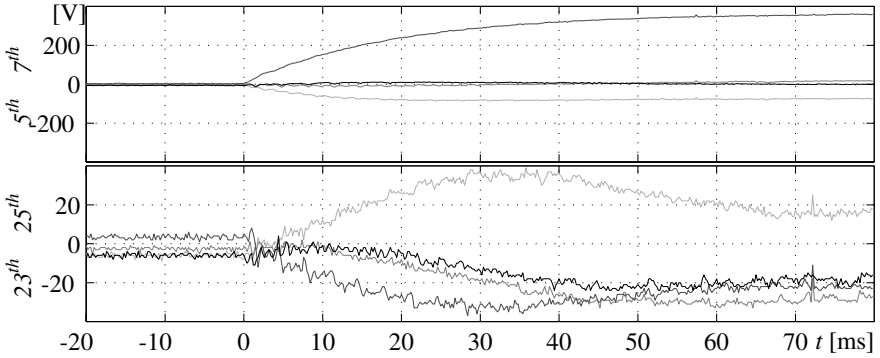

Figure 6.12 Turn on of the MRI harmonic filter controller. Integrator outputs oriented to the current harmonics of orders 5th and 7th (top), and 23rd and 25th (bottom).

Note that the shown dynamic response of the MRI controller only describe the turn on of the harmonic oriented integrators. Hence, the transient behaviour concerning load changes is not displayed.

However, the transient behaviour of the MRI controller is nevertheless improved. The smooth start of the integrators neutralises the transient coupling in the high pass filter output shown in Figure 5.6. In fact, the transient response is very well described by the dynamic response shown in this section.

7

Conclusions

In this thesis, a high performance battery charger for EVs is presented. The drawbacks of line-commutated battery chargers in terms of the current harmonic generation and the reactive power requirement, are overcome by the use of self commutated charger topologies. By including power line conditioning capabilities in the battery charger, a viable concept for a fast charging infrastructure is obtained. The use of the investment in the fast charging infrastructure increases, since both EV users and power distributors can utilise the battery chargers for their own purposes. The EV user extends the driving range of the EV whereas the power distributor increases the power quality. Furthermore, the investigated concept is not restricted to battery chargers, but can also be applied to other applications involving the power grid, such as photo voltaic systems and uninterruptible power supplies (UPS).

The investigated battery charger consists of a three phase VSC and a half bridge DC-DC converter connected back to back across a DC-link capacitor. Carrier wave based PWM is employed. Furthermore, the switching frequency harmonics are attenuated by third order LCL-filters. The advantageous low frequency characteristics of the LCL-filter facilitates better utilisation of the DC-link voltage when performing grid conditioning. Modelling aspects and design considerations for the battery charger are given in the thesis.

The control system of the battery charger consists of model based discrete controllers, where the synchronous reference *dq*-frame are applied for the line current controller. Basically, the derived control system consists of cascaded P- and PI-controllers. Additional feed forward are employed in order to improve the transient behaviour of the control system. Furthermore, the cascaded current controllers are interpreted as linear state feedback controllers in order to perform theoretical analysis and confirm stability of the control system.

The use of the synchronous reference *dq*-frame in the line current controller enables direct separation between the fundamental, the

negative-sequence and the harmonic current components. This is utilised in the load current identification part of the active filter control structure.

The model based line current controller suffers from the inherent phase deviation caused by the PWM technique employed. This is circumvented by use of the direct phase compensation method. The experimental results, however, reveal other weaknesses of this active filter controller, such as the sensitivity to system parameters and the inability to compensate for the current harmonics caused by the shunt AF itself due to the non-linear properties of the VSC, such as the blanking time.

Instead a control structure for shunt AFs based on several integrators in multiple rotating reference frames is proposed. The main objectives with the proposed MRI controller are to reduce the sensitivity to system parameters and further improve the steady state performance of the shunt AF. An additional feature obtained by the proposed MRI controller is harmonic selectivity. The superior performance of the MRI controller is verified both theoretically and experimentally. It is found that the introduced rotating integrators practically eliminates the corresponding current harmonics. Furthermore, the dynamic performance is determined by the integral time constant selected. Also, the MRI controller neutralises the coupling during transient operation which is due to the low pass filtering property of the harmonic oriented integrators.

References

[1] H. Akagi, Y. Kanazawa and A. Nabae, ”Instantaneous Reactive Power Compensators Comprising Switching Devices without Energy Storage Components”, *IEEE Transactions on Industry Applications*, Vol. 20, No. 3, May/June 1984, pp. 625-630.

[2] H. Akagi, A. Nabae and S. Atoh, ”Control Strategy of Active Power Filters Using Multiple Voltage-Source PWM Converters”, *IEEE Transactions on Industry Applications*, Vol. 22, No. 3, May/June 1986, pp. 460-465.

[3] H. Akagi, ”New Trends in Active Filters for Power Conditioning”, *IEEE Transactions on Industry Applications*, Vol. 32, No. 6, November/December 1996, pp. 1312-1322.

[4] S. Bhattacharya, D.M. Divan and B. Banerjee, ”Synchronous Frame Harmonic Isolator Using Active Series Filter”, *EPE 91 Conference Proceedings*, Firenze, Italy, Vol. 3, September 1991, pp. 3030-3035.

[5] M. Bojrup, P. Karlsson, M. Alaküla and B. Simonsson, ”A Dual Purpose Battery Charger for Electric Vehicles”, *PESC’98 Conference Proceedings*, Fukuoka, Japan, Vol. 1, May 1998, pp. 565-570.

[6] M. Bojrup, P. Karlsson, M. Alaküla and Lars Gertmar, ”A Multiple Rotating Integrator Controller for Active Filters”, *EPE 99 Conference Proceedings*, Lausanne, Switzerland, September 1999.

[7] A. Carlsson, ”The back-to-back converter; control and design”, *Licentiate’s Thesis, Department of Industrial Electrical Engineering and Automation, Lund Institute of Technology*, Lund, Sweden, May 1998.

[8] A. Edris, A.S. Mehraban, M. Rahman, L. Gyugyi, S. Arabi and T. Reitman, ”Controlling the flow of Real and Reactive Power”, *IEEE Computer Applications in Power*, No. 1, 1998, pp. 20-25.

[9] T. Glad and L. Ljung, ”Reglerteknik. Grundläggande teori”, (in Swedish), *Studentlitteratur*, Lund, Sweden, 1989.

[10] J.D. Glover and M. Sarma, ”Power System Analysis & Design”, *PWS Publishing Company*, 2nd edition, 1994.

[11] L. Harnefors, ”On Analysis, Control and Estimation of Variable-Speed Drives”, *Ph. D. Thesis, Electrical Machines and Drives, Department of Electric Power Engineering, Royal Institute of Technology*, Stockholm, Sweden, 1997.

[12] H.J. Haubrich and A.R. Heider, ”Charging Strategies for Electric Vehicles and their Consequences for Power Supply”, *EPE 97 Conference Proceedings*, Trondheim, Norway, Vol. 1, September 1997, pp. 1560-1565.

[13] M. Hemmingsson, ”A Powerflow Control Strategy to Minimize Energy Losses in Hybrid Electric Vehicles”, *Licentiate’s Thesis, Department of Industrial Electrical Engineering and Automation, Lund Institute of Technology*, Lund, Sweden, January 1999.

[14] J. Hokfelt and F. Tufvesson, ”Övertonernas nätpåverkan i låg- och mellanspännings stadsnät”, (in Swedish), *Master’s Thesis, Department of Industrial Electrical Engineering and Automation, Lund Institute of Technology*, Lund, Sweden, September 1993.

[15] J. Holtz, ”Pulsewidth Modulation for Electronic Power Conversion”, *Proc. of the IEEE*, Vol. 82, No. 8, August 1994, pp. 1194-1214.

[16] H. Kahlen and G. Maggeto, ”Electric and Hybrid Vehicles”, *EPE 97 Conference Proceedings*, Vol. 1, September 1997, pp. 1.030-1.054.

[17] P. Karlsson, M. Bojrup, M. Alaküla and L. Gertmar, ”Efficiency of Off-Board, High Power, Electric Vehicle Battery Chargers with Active Power Line Conditioning Capabilities”, *EPE 97 Conference Proceedings*, Trondheim, Norway, Vol. 4, September 1997, pp. 4688-4692.

[18] P. Karlsson, ”Quasi Resonant DC Link Converters – Analysis and Design for a Battery Charger Application”, *Licentiate’s Thesis, Department of Industrial Electrical Engineering and Automation, Lund Institute of Technology*, Lund, Sweden, November 1999.

[19] K.W. Klontz, D.M. Divan and D.W. Novotny, ”An Actively Cooled 120 kW Coaxial Winding Transformer for Fast Charging Electric Vehicles”, *IEEE-IAS Conf. Rec.*, Denver, USA, October 1994, pp. 1049-1054.

[20] K. Kubo and K. Sakai, ”Feedforward Voltage Compensation for Digital Active Filter Using Frequency Domain Decomposition”, *EPE 97 Conference Proceedings*, Trondheim, Norway, Vol. 4, September 1997, pp. 4.786-4.791.

[21] N.H. Kutkut, D.M. Divan, D.W. Novotny and R.H. Marion, ”Design Considerations and Topology Selection for a 120-kW IGBT Converter for EV Fast Charging”, *IEEE Transactions on Power Electronics*, Vol. 13, No. 1, January 1998, pp. 169-178.

[22] J.W. Lee, ”An Intelligent Current Controller Using Delay Compensation for PWM Converters”, *EPE 97 Conference Proceedings*, Vol. 1, September 1997, pp. 1.342-1.347.

[23] M. Lindgren, ”Filtering and Control of a Grid-connected Voltage Source Converter”, *Licentiate’s Thesis, Department of Electric Power Engineering division of Electrical Machines and Power Electronics, Chalmers University of Technology*, Gothenburg, Sweden, September 1995.

[24] M. Lindgren, ”Modelling and Control of Voltage Source Converters Connected to the Grid”, *Ph. D. Thesis, Department of Electric Power Engineering division of Electrical Machines and Power Electronics, Chalmers University of Technology*, Gothenburg, Sweden, November 1998.

[25] P. Lundberg, ”Grid-connected NPC Converter in Load Balancing Applications”, *Licentiate’s Thesis, Department of Electric Power Engineering division of Electrical Machines and Power Electronics, Chalmers University of Technology*, Gothenburg, Sweden, November 1994.

[26] J.M. Maciejowski, ”Multivariable Feedback Design”, *Addison-Wesley*, 1989.

[27] N. Mohan, T.M. Undeland and W.P. Robbins, ”Power Electronics; Converters, Applications, and Design”, *Wiley*, New York, USA, 2nd edition, 1995.

[28] S. Ogino and Y. Kimura, ”Fuel Cell Powered Electric Vehicle”, *EVS 13 Conference Proceedings*, Osaka, Japan, Vol. 1, October 1996, pp. 671-674.

[29] D. Ouverkerk, ”Who says you can’t pass high power through a paddle?”, *EVS 12 Conference Proceedings*, Anaheim, USA, Vol. 1, December 1994, pp. 612-618.

[30] D. Owen, J. Simpson and J. McGuire, ”UK Electric Vehicle Charging Infrastructure Case Study”, *EVS 12 Conference Proceedings*, Anaheim, USA, Vol. 1, December 1994, pp. 136-144.

[31] S. Rahman and G.B. Shrestha, ”An investigation into the impact of electric vehicle load on the electric utility distribution system”, *IEEE Transactions on Power Delivery*, Vol. 8, No. 2, April 1993, pp. 591-597.

[32] O. Simon, H. Spaeth, K.-P. Juengst and P. Komarek, ”Experimental Setup of a Shunt Active Filter Using a Superconducting Magnetic Energy Storage Device”, *EPE 97 Conference Proceedings*, Trondheim, Norway, Vol. 1, September 1997, pp. 1447-1452.

[33] R. Strzelecki, L. Frackowiak and G. Benysek, ”Hybrid Filtration in Conditions of Asymmetric Nonlinear Load Current Pulsation”, *EPE 97 Conference Proceedings*, Trondheim, Norway, Vol. 1, September 1997, pp. 1.453-1.458.

[34] T. Svensson, ”On Modulation and Control of Electronic Power Convertors”, *Ph. D. Thesis, Department of Electrical Machines and Power Electronics, Chalmers University of Technology*, Gothenburg, Sweden, November 1988.

[35] M. Yano, S. Kuramochi and N. Nanaumi, ”New Control Method of Harmonic Current Compensation Using Individual Rotaing P-Q Frame of Corresponding Frequency”, *EPE 97 Conference Proceedings*, Trondheim, Norway, Vol. 4, September 1997, pp. 4842-4847.

[36] W. Zhang, ”On Feedback Control of Active DC Filters in HVDC Cable Links with Coastal Lines”, *Licentiate’s Thesis, Division of High Power Electronics, Department of Electric Power Engineering, Royal Institute of Technology*, Stockholm, Sweden, December 1995.

[37] K.J. Åström and B. Wittenmark, ”Computer Controlled Systems; Theory and Design”, *Prentice-Hall International*, Englewoods Cliffs, USA, 2nd edition, 1990.

A

Vector notation

A.1 Three phase to two phase transformation

Three phase quantities (s_a, s_b and s_c) are transformed to two phase vector representation by

$$\vec{s}^{\alpha\beta} = s_\alpha + j s_\beta = \sqrt{\frac{2}{3}}\left(s_a\, e^{j0} + s_b\, e^{j\frac{2\pi}{3}} + s_c\, e^{j\frac{4\pi}{3}} \right) \tag{A.1}$$

or in real notation

$$\begin{cases} s_\alpha = \sqrt{\frac{2}{3}}\left(s_a - \frac{1}{2}(s_b + s_c)\right) \\ s_\beta = \sqrt{\frac{1}{2}}\left(s_b - s_c\right) \end{cases} \tag{A.2}$$

The inverse, two phase to three phase transformation for a balanced system, i.e.

$$s_a + s_b + s_c = 0 \tag{A.3}$$

is given by

$$\begin{cases} s_a = \sqrt{\frac{2}{3}}\, s_\alpha \\ s_b = -\sqrt{\frac{1}{6}}\, s_\alpha + \sqrt{\frac{1}{2}}\, s_\beta \\ s_c = -\sqrt{\frac{1}{6}}\, s_\alpha - \sqrt{\frac{1}{2}}\, s_\beta \end{cases} \tag{A.4}$$

If the three phase quantities are sinusoidally varying with rms-value S, angular frequency ω_1 and phase shifted 120° in time

$$\begin{cases} s_a = \sqrt{2} S \cos(\omega_1 t) \\ s_b = \sqrt{2} S \cos(\omega_1 t - \frac{2\pi}{3}) \\ s_c = \sqrt{2} S \cos(\omega_1 t - \frac{4\pi}{3}) \end{cases} \tag{A.5}$$

then the corresponding vector is

$$\vec{s}^{\,\alpha\beta} = \sqrt{3}S e^{j\omega_1 t} \tag{A.6}$$

Thus, the vector rotates with constant magnitude $\sqrt{3}S$ and angular frequency ω_1 in the stationary reference $\alpha\beta$-frame.

A.2 Vector transformation

A vector in the stationary reference $\alpha\beta$-frame is transformed into the synchronously rotating reference dq-frame oriented to the integral of grid voltage vector, see Figure A.1, by subtracting the angle difference θ

$$\vec{s}^{\,dq} = \vec{s}^{\,\alpha\beta} e^{-j\theta} \tag{A.7}$$

where the angle difference, transformation angle θ, is given by

$$\vec{e}^{\,\alpha\beta} = E_n e^{j\omega_1 t} \Rightarrow \vec{\psi}^{\,\alpha\beta} = \int \vec{e}^{\,\alpha\beta} dt = \Psi_n e^{j\left(\omega_1 t - \frac{\pi}{2}\right)} \Rightarrow \theta = \omega_1 t - \frac{\pi}{2} \tag{A.8}$$

The transformation can also be expressed in real notation as

$$\begin{bmatrix} s_d \\ s_q \end{bmatrix} = \begin{bmatrix} \cos\theta & \sin\theta \\ -\sin\theta & \cos\theta \end{bmatrix} \begin{bmatrix} s_\alpha \\ s_\beta \end{bmatrix} \tag{A.9}$$

Hence, a rotating vector in the stationary reference $\alpha\beta$-frame

$$\vec{s}^{\,\alpha\beta} = \sqrt{3}Se^{j(\omega_1 t - \varphi)} \tag{A.10}$$

is transformed into a vector in the synchronous reference dq-frame

$$\vec{s}^{\,dq} = \vec{s}^{\,\alpha\beta} e^{-j\left(\omega_1 t - \frac{\pi}{2}\right)} = \sqrt{3}Se^{j\left(\frac{\pi}{2} - \varphi\right)} = s_d + js_q \tag{A.11}$$

where the real and imaginary parts are constants, i.e. DC quantities.

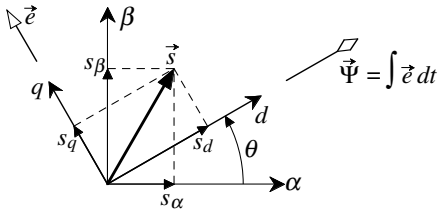

Figure A.1 Relationship between the stationary reference $\alpha\beta$-frame and the synchronously rotating reference dq-frame.

The inverse transformation, from the synchronously rotating reference dq-frame to the stationary reference $\alpha\beta$-frame is equivalently given by

$$\vec{s}^{\,\alpha\beta} = \vec{s}^{\,dq} e^{j\theta} \tag{A.12}$$

In real notation the inverse transformation is given by

$$\begin{bmatrix} s_\alpha \\ s_\beta \end{bmatrix} = \begin{bmatrix} \cos\theta & -\sin\theta \\ \sin\theta & \cos\theta \end{bmatrix} \begin{bmatrix} s_d \\ s_q \end{bmatrix} \tag{A.13}$$

A.3 Instantaneous power

The three phase to two phase transformation given in (A.1) is power invariant, i.e. the instantaneous power can be expressed as

$$p = u_a \cdot i_a + u_b \cdot i_b + u_c \cdot i_c \tag{A.14}$$

or

$$p = \Re\mathrm{e}\left(\vec{u}^{\,\alpha\beta} \cdot \vec{i}^{\,\alpha\beta *}\right) = u_\alpha \cdot i_\alpha + u_\beta \cdot i_\beta \tag{A.15}$$

or

$$p = \Re\mathrm{e}\left(\vec{u}^{\,dq} \cdot \vec{i}^{\,dq *}\right) = u_d \cdot i_d + u_q \cdot i_q \tag{A.16}$$

B

Normalisation

B.1 Per unit definition

The base values for power, voltage and frequency are defined according to

$$\begin{aligned} S_{base} &= S_n \\ U_{base} &= E_n \\ \omega_{base} &= \omega_1 \end{aligned} \tag{B.1}$$

where S_n is the rated power, E_n is the line to line rms-value of the grid voltage and ω_1 is the fundamental grid frequency. The base values for current and impedance are then obtained according to

$$I_{base} = \frac{S_{base}}{U_{base}} = \sqrt{3} I_n \tag{B.2}$$

$$Z_{base} = \frac{U_{base}^2}{S_{base}} = \frac{U_{base}}{I_{base}} \tag{B.3}$$

where I_n is the rated line (phase) current. Z_{base} can further be divided into bases for inductance and capacitance according to

$$L_{base} = \frac{Z_{base}}{\omega_{base}} \tag{B.4}$$

$$C_{base} = \frac{1}{\omega_{base} Z_{base}} \tag{B.5}$$

The normalised (per unit) values of the electrical parameters are then given by

$$R_{p.u.} = \frac{R_{[\Omega]}}{Z_{base}} \tag{B.6}$$

$$L_{p.u.} = \frac{L_{[\mathrm{H}]}}{L_{base}} = \left\{ \frac{\omega_{base} L_{[\mathrm{H}]}}{Z_{base}} \right\} = \frac{X_{L,[\Omega]}}{Z_{base}} \tag{B.7}$$

$$C_{p.u.} = \frac{C_{[\mathrm{F}]}}{C_{base}} = \left\{ \omega_{base} Z_{base} C_{[\mathrm{F}]} = \frac{Z_{base}}{\frac{1}{\omega_{base} C_{[\mathrm{F}]}}} \right\} = \frac{Z_{base}}{X_{C,[\Omega]}} \tag{B.8}$$